Design and implementation of an apparatus for sliced velocity map imaging of H atoms

Mikhail Ryazanov

Reisler group

August 2012

Table of contents

Design and implementation of an apparatus for sliced velocity map imaging of H atoms

1 Introduction

Velocity map imaging (VMI) is the most powerful method of momentum spectroscopy — experimental investigation of mechanical momentum distributions of free particles, products of disintegration (dissociation, ionization, detachment) and scattering of atomic and molecular systems. While VMI is inherently applicable to electrically charged particles only, with the help of an appropriately selected ionization method (such that the ion retains the initial momentum of the neutral particle and does not decompose) it becomes suitable for neutral products as well. Moreover, highly selective ionization methods, such as resonance-enhanced multiphoton ionization (REMPI), allow state-resolved detection of the products. This makes VMI the ultimate tool in scattering experiments — assuming that the initial momenta are known and measuring the final momentum of one particle[1], the differential scattering cross-section can be directly obtained in the experiment. Employment of coincidence detection schemes allows to study more complicated processes, where more than two fragments are formed.

The fundamental idea of VMI is that if the charged particles are formed in a specially shaped electric field (or the field is switched on at the right moment of time), they are accelerated towards the detector in such a way that their arrival positions and times depend on the initial velocities. In a coordinate system defined with the x and y axes parallel to the detector plane, and z perpendicular to it and coinciding

[1]The other momentum is known from conservation of the total momentum.

with the symmetry axis of the VMI apparatus (see figure 1), this VMI mapping can

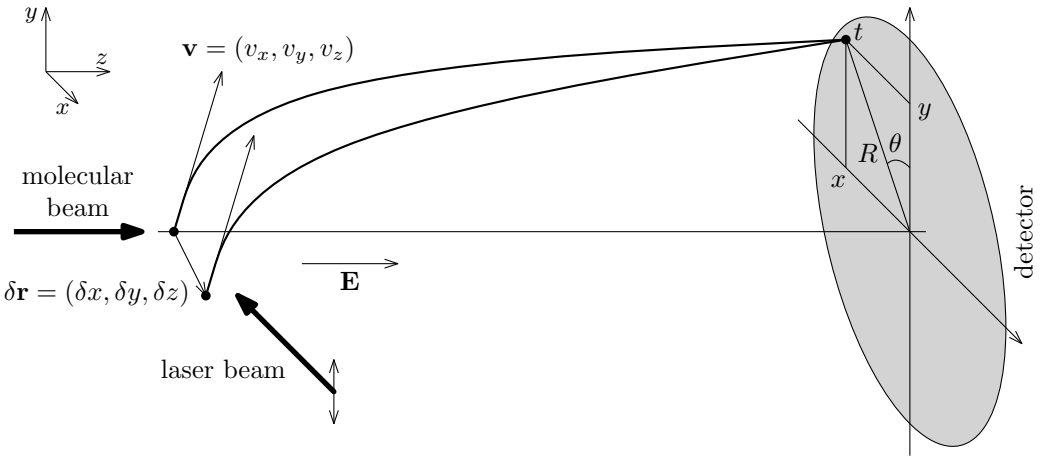

Figure 1 General scheme of velocity map imaging setup.

be written as

$$\mathbf{v} = (v_x, v_y, v_z) \mapsto (x, y, t). \tag{1}$$

(The mapping is approximately linear and is different for particles of different masses, which will be discussed later.) Thus collecting the data from a position/time-resolving detector allows determination of the initial velocity vector of the particle. While such mapping can be achieved simply by a homogeneous electric field, a special shape of an inhomogeneous field is required to make the mapping insensitive to the initial positions $\delta\mathbf{r}$ of the particles. This "focusing" is important, since in the experiment the interaction/ionization region always has a finite size, sometimes not significantly smaller than the detector radius, and mapping of the initial positions to the arrival positions and times would lead to overlap between the images of different velocities, inevitably reducing the velocity resolution of the system.

Historically, detectors resolving both position and time became available only recently, and they are still more expensive and complicated and have lower resolution and/or saturation level[1] than detectors resolving only position (2-dimensional) or time (1-dimensional).[2]

Ion current multipliers were known for a long time and, being connected to a fast oscilloscope, presented a tool for measurements of arrival time distributions. Among the instruments based on this kind of detection were time of flight (TOF) mass spec-

[1] Maximum number of detectable particles per acquisition frame.
[2] See for example [1] and section 3.2 in review [2].

trometers. Although intended to measure mass spectra instead of velocity spectra, they can be considered as precursors of modern VMI spectrometers. In 1955 Wiley and McLaren gave a detailed analysis [3] of TOF mass spectrometers, where they described the electric field configuration required to minimize the effect of the initial spatial spread of the particles on their arrival time (space focusing conditions) and discussed the effect of the initial kinetic energy. In connection with VMI, the TOF space focusing conditions are a subset of the overall VMI focusing conditions, and the kinetic energy effect on TOF is directly related to the $v_z \mapsto t$ part of (1), allowing determination of the 1-dimensional projection of the initial velocity distribution from the measured profile of the TOF signal. This is especially useful in combination with the so-called "core sampling" technique [4] where a mask placed in front of the detector selects a narrow range of the other two velocity components according to the $(v_x, v_y) \mapsto (x, y)$ part of (1). Therefore, the determination of the full 3-dimensional distribution is, in principle, possible by scanning the mask position. However, since only a small fraction of all particles is detected, the method either has poor resolution (in v_x and v_y) or is very time-consuming.

The advent of reliable microchannel plate (MCP) multipliers in 1970s [5] was an essential step in the development of position-sensitive detectors with high spatial resolution. The idea was to install a phosphor screen immediately after the MCP to convert the amplified space-resolved current to an optical image (as in MCP-based image intensifiers) and then record the resulting image with the already widely available high-resolution optical imaging instruments. For example, modern systems use a digital videocamera with ~1 Mpx resolution directly connected to a computer for real-time data analysis. However, this kind of detector does not have sufficient time resolution to obtain the v_z component for each particle. In principle, the total MCP current can be measured simultaneously with the image acquisition and yield an equivalent of the TOF signal. Thus 2-dimensional distribution of (v_x, v_y) and 1-dimensional distribution of v_z can be determined, but the correlation between these distributions is lost, and determination of the initial 3-dimensional distribution of (v_x, v_y, v_z) is not possible in the general case. There are however a few special cases when the 3-dimensional distribution can be determined with acceptable accuracy from these incomplete data.

First, in the limit when the average number of particles reaching the detector is very small, most of acquisition frames have at most one detection event. In that

case the (v_x, v_y) components of the sole particle can be directly determined from the single spot location in the image frame, and the v_z component can be directly determined from the single peak time in the MCP current, providing the full velocity vector (v_x, v_y, v_z) of the single detected particle. The obvious disadvantage of this case is that the amount of information gained from each frame is very small, and thus an accurate determination of the distribution requires a very large number of frames. Since the frame rate is limited by the laser repetition rate (10 Hz in the present work) and/or the videocamera acquisition capabilities (usually $\lesssim$100 Hz), the overall required experiment time becomes extremely long.

The situation can be somewhat improved by using a split anode (that is, instead of the total TOF signal, several TOF signals with coarse spatial resolution are recorded, and the spatial resolution is subsequently improved using the imaging data; the number of events is then limited by one per *each* anode segment and thus can reach several events per acquisition frame) or a resistive or delay-line anode (which can give precise arrival time information and some position information, but only when no more than one particle arrives within the detection time interval; this "dead time" limits the total number of detectable events). A detailed description of such 3-dimensional techniques is available in a comprehensive review [2]. Unfortunately, they offer only a moderate increase in the allowed signal intensity and require much more specialized and expensive equipment, so they will not be considered here.

Another very important case is when the 3-dimensional distribution is known to have some symmetry that reduces the amount of unknown information to 2 or 1 dimensions. For example, in photodissociation or photoionization by a single linearly polarized laser the distribution of the photofragments has cylindrical symmetry with the axis parallel to the laser polarization vector.[1] That is, assuming the symmetry axis is the y axis, the 3-dimensional distribution $I(v_x, v_y, v_z)$ can be described as 2-dimensional $I(v_\rho, v_y)$, where $v_\rho = \sqrt{v_x^2 + v_z^2}$. This reduction does not facilitate the measurements by itself, but suggests that there might exist a bijective (one-to-one)

[1]The case of spherical symmetry is even simpler (and its angle-independent radial distribution can be measured directly by core-sampling TOF), but for the present discussion we can consider it as a subcase of cylindrical symmetry.

mapping between $I(v_\rho, v_y) = I\left(\sqrt{v_x^2 + v_z^2}, v_y\right) = I(v_x, v_y, v_z)$ and its measured projection

$$P(v_x, v_y) = \int_{-\infty}^{+\infty} I(v_x, v_y, v_z)\, dv_z = \int_{|v_x|}^{+\infty} I(v_\rho, v_y) \frac{v_\rho\, dv_\rho}{\sqrt{v_\rho^2 - v_x^2}}. \tag{2}$$

The forward mapping $I(v_\rho, v_y) \mapsto P(v_x, v_y)$ explicitly given by (2) is called "Abel transform".[1] Its properties were studied in the 19th century, and the inverse transform was found in an explicit form:

$$I(v_\rho, v_y) = -\frac{1}{\pi} \int_{v_\rho}^{+\infty} \frac{dP(v_x, v_y)}{dv_x} \frac{dv_x}{\sqrt{v_x^2 - v_\rho^2}}. \tag{3}$$

Therefore, in case of cylindrical symmetry, the initial 3-dimensional distribution indeed can be reconstructed from the measured 2-dimensional projection.

This approach was first applied to photochemical reactions by Chandler and Houston in 1987 [6]. Their setup did not use proper electric field configuration to perform VMI focusing (see p. 5), so the obtained velocity resolution was very limited, but nevertheless the results were encouraging. The situation greatly improved in 1997 when Eppink and Parker demonstrated [7] that the focusing can be easily achieved by using a simple electrostatic lens. Their arrangement is still widely used today in the original form or with minor modifications, and velocity resolution $\Delta v/v \approx 0.2\,\%$ has been reached[2] (see, for example, [8]).

Despite all its success, the "projection–reconstruction" approach has a few serious drawbacks. The most obvious one — inapplicability to distributions lacking cylindrical symmetry — is a major concern for general scattering experiments, but has no importance for the present work. However, two other important issues are related to the reconstruction part described by (3). First, the integral is taken from v_ρ to infinity, meaning that in order to get $I(v_\rho)$ at particular v_ρ, knowledge of the projection $P(v_x)$ for all $v_x \geqslant v_\rho$ is required. In other words, even if all the information interesting for a particular experiment is contained only in the low-velocity part of

[1] Strictly speaking, Abel transform connects 1-dimensional functions $I_{v_y}(v_\rho) \equiv I(v_\rho, v_y)$ and $P_{v_y}(v_x) \equiv P(v_x, v_y)$ for each particular v_y. That is, mapping (2) is a direct product of Abel transform in the v_ρ subspace and identity mapping in the v_y subspace.

[2] For monochromatic particles. This qualification is important since all ion-optical systems have chromatic aberrations, and thus the more relevant parameter $\max \Delta v/v_{\max}$ calculated over the whole velocity range might be larger. A more detailed discussion is given on p. 36.

the distribution, its extraction without recording the complete projection of the whole distribution is impossible. As a consequence, the relative velocity resolution for the interesting part of the distribution is decreased. The second, partially related, issue is associated with the form of the integrand. The experimentally measured projection always has some noise,[1] and its differentiation leads to an extreme amplification of the noise. Although the resulting very noisy derivative is then integrated, the integration weight $1/\sqrt{v_x^2 - v_\rho^2}$ drops quite quickly near the lower integration limit, so that no efficient averaging takes place. At the same time, the weight drops slowly for large v_x values, and the noise from the outer parts of the image makes a significant contribution to the inner parts of the reconstructed distribution. That is, the intensity resolution (signal-to-noise ratio) of the low-velocity part of the distribution is also noticeably reduced.

The third special case or, more precisely, approach to determination of the 3-dimensional distribution from 2-dimensional measurements was developed under the name "sliced VMI" (SVMI) in 2001 by Gebhardt, Rakitzis, Samartzis, Ladopoulos and Kitsopoulos [9], and in 2003 in a better form by Lin, Zhou, Shiu and Liu [10] and Townsend, Minitti and Suits [11]. It is based on the fact that preselection of one v_z value for all particles can be done much easier that resolution of v_z for each of them. That is, 2-dimensional slices $I_{v_z}(v_x, v_y)$ can be recorded for any chosen v_z value. The whole 3-dimensional distribution then can be obtained by v_z scanning — very similar to the core sampling approach, but much more efficient, since the 2-dimension spatial scanning with a mechanical mask is replaced with the 1-dimension temporal scanning with an electrical detector-gating pulse.

Moreover, the application of SVMI to cylindrically symmetric distributions is very advantageous, because in that case the central slice ($v_z = 0$) contains *all* the required information. Namely, if the slicing function $S(v_z)$[2] is centered at $v_z = 0$ (that is, $\int v_z S(v_z)\, dv_z = 0$), then the measured sliced projection is

$$P(v_x, v_y) = \int_{-\infty}^{+\infty} I(v_x, v_y, v_z) S(v_z)\, dv_z \approx \tag{4}$$

[1] The lower limit of the noise level is determined by the shot noise due to the discrete nature of the measured signal. In practice, the projection intensity (the number of events per resolved interval $\Delta v_x\, \Delta v_y$) is of the order of 100, leading to the relative noise of the order of $\sqrt{100}/100 = 10\,\%$.

[2] Defined as the dependence of the relative detection efficiency on the v_z velocity component. It is assumed to be normalized by amplitude: $\max S(v_z) = 1$.

$$\approx I(v_x, v_y, 0) \cdot \Delta v_z, \tag{5}$$

where $\Delta v_z = \int S(v_z)\, dv_z$ is the effective slice thickness. Therefore, if the slice is thin enough, the initial distribution can be obtained immediately as

$$I(v_\rho, v_y) \approx P(v_x = v_\rho, v_y)/\Delta v_z \quad \text{for } v_\rho \gg \Delta v_z. \tag{6}$$

A quantitative estimation of how thin the slice should be is readily obtained from the diagram shown in figure 2. The monochromatic particles with velocity v_ρ produce

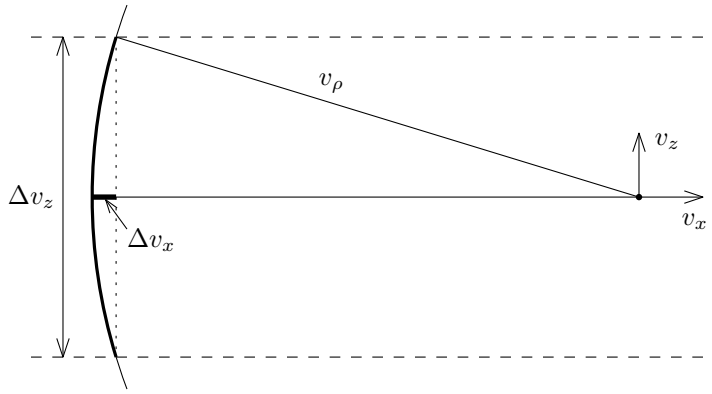

Figure 2 Illustration of blurring due to a finite slice thickness. The thick arc shows the part of monochromatic particles that is detected by slicing. The recorded projection of the arc is shown by the thick straight segment marked Δv_x.

the finite effective range Δv_x in the sliced projection with the effective thickness Δv_z. The relative blurring is then

$$\frac{\Delta v_x}{v_\rho} = 1 - \sqrt{1 - \left(\frac{\Delta v_z}{2v_\rho}\right)^2} \approx \frac{1}{2}\left(\frac{\Delta v_z}{2v_\rho}\right)^2. \tag{7}$$

That is, even if the effective slice thickness Δv_z is ~1/10 of the total velocity range $2v_\rho$ (from $-v_\rho$ to $+v_\rho$), the effective blurring is only ~0.5 %. Of course, with a fixed slice thickness the relative resolution decreases for the low-velocity part of the distribution (when $v_\rho \ll \Delta v_z$, the "sliced" projection (4) degenerates to the regular projection (2)). However, in contrast to the full projection approach, the expression (6) for "reconstruction" is *local*, meaning that the low-velocity part can be measured separately with higher resolution.[1] Moreover, the transformation (4) is also invertible, and the

[1]The ratio $\Delta v_z/v_\rho$ for a fixed slicing pulse duration depends on the ion cloud TOF stretching. As

inverse transformation has better properties than the inverse Abel transform (3). This means that SVMI always outperforms conventional 2-dimensional VMI.

Several other special cases allowing determination of the 3-dimensional distribution from its 2-dimensional projections can be found in the VMI review [12]. Some special techniques for selective detection are also mentioned there. However, these techniques are less general than the described slicing approach[1] and hence are not considered in this work.

The overview of the available VMI methods given above reveals that SVMI is the most effective choice for studies of product distributions in photodissociation reactions. Therefore, the following sections are focused on the desired performance of the SVMI setup, the general properties of ion-optical systems suitable for SVMI implementation, and the selection of the optimal design and its parameters to meet the performance requirements.

2 Design goals

The designed SVMI system was intended to replace the previously used TOF detection system in the free-radical molecular beam apparatus designed and built by Conroy and described in his Ph. D. dissertation [13]. Since the apparatus itself has shown good operability and satisfied the experimental needs, it was desirable to implement the retrofitting with minimal changes to the other parts of the machine. This imposed some geometric constraints on the ion optics parts, as discussed later. Another important geometrical parameter in the design was the detector diameter. Since the MCP detector assembly is the most expensive part of the SVMI system and the only part that has a finite lifetime and thus has to be replaced occasionally, it was decided, for unification purposes, to employ the same detector type as in the other VMI setup [14] used in the laboratory.

The primary design goal of the new system was the ability to perform SVMI of atomic hydrogen products from photodissociation of small organic radicals. The ki-

discussed in subsections 4.3 and 5.5, the experimental conditions required to achieve large TOF stretching are more favorable for slower particles. Thus the achievable SVMI resolution is generally better for the low-velocity part of the distribution if it is measured separately.

[1] For example, the “optical slicing” method requires a pump–probe arrangement in which the “pump” laser(s) should not cause ionization of the studied particles, and the “probe” laser should only ionize them and should not create such particles by itself

netic energy release (KER) in such processes ranges from a fraction of an electronvolt to a few electronvolts, and due to the large mass difference between the H fragment and the molecular cofragment, almost all the kinetic energy is carried by the H atom. Conversion of the produced H atoms to detectable H^+ ions is performed by the convenient and practically proven [13] near-threshold REMPI through the $2p$ state. The process is quite efficient and, since the recoil in near-threshold ionization is negligible, the produced H^+ ions retain the initial momentum of the H fragments. The achievable resolution is therefore determined by the uncertainties in the initial experimental conditions and the accuracy of the SVMI setup itself.

The experimental uncertainties involve position, velocity and time uncertainties. The initial position uncertainty comes from the finite size of the ionization region, determined by the intersection of the molecular beam with the ionizing laser beam, and the finite precision of the location of this intersection relative to the ion-optical system. The diameter of the skimmed molecular beam at the ionization region is 2–3 mm, and the laser beam waist length is usually comparable to it. This defines the Δx uncertainty (see figure 1). The Δy and Δz uncertainties are mostly defined by the laser beam alignment relative to the ion optics, since the beam waist radius is usually negligibly small (of the order of several micrometers for the focused beam), and can be estimated as ~1 mm each.

The initial velocity uncertainty comes from the velocity distribution of the parent radical and is determined by the velocity spread in the molecular beam. The average speed in a "supersonic" helium beam does not exceed ~1400 m/s. Given the nozzle diameter of 0.5 mm and the skimmed beam diameter of 2–3 mm at ~100 mm from the nozzle, the beam divergence multiplied by the average speed yields a limit for the transversal velocity components Δv_x and Δv_y of about 50 m/s which is less than 0.5 % of the characteristic speed of H fragments (~14 000 m/s for 1 eV kinetic energy). The longitudinal velocity spread Δv_z might be somewhat larger, but is still small compared to the H fragment velocities. Moreover, since v_z is not measured, and Δv_z affects only the effective slice thickness, its effect on the resolution should be negligible.

The initial time uncertainty is due to the finite duration of the ionizing laser pulse and the timing jitter. The optical pulse is generated by frequency doubling of the radiation produced by a dye laser pumped with a Q-switched Nd:YAG laser and thus has a duration of a few nanoseconds. Its jitter directly replicates the jitter of the

pump laser and generally does not exceed 1 ns. Thus the overall time resolution of the experiment is inherently limited at the few nanoseconds level, and this fact must be taken into account when the desired characteristics of the SVMI setup are considered. In particular, slicing with detector gating pulses shorter than a few nanoseconds will not lead to any improvement in the resolution but rather will decrease the recorded signal strength, according to (5). The effective relative slice thickness ~1/10 required for good resolution (see p. 10) therefore demands TOF stretching for the imaged velocity range of the order of a few tens of nanoseconds. This criterion constitutes the main difficulty in the SVMI design for H ions, as discussed below.

Another major requirement for the new system was not directly related to its SVMI capabilities but concerned its ability to operate in the TOF mass spectrometer (TOF-MS) mode with sufficient mass resolution. As mentioned above, VMI spectrometers grew out of TOF mass spectrometers and in principle can be used for the same purpose. However, the optimal design decisions and operation parameters for these two uses are quite different and even contradictory in some respects. Fortunately, the mass resolution required mostly for diagnostic purposes — observation of the radicals, their precursors and decomposition products — is very modest by the TOF-MS standards. The ions of interest contain a few C, O and H/D atoms and, possibly, one halogen (Cl) atom. Therefore, a mass resolution of 1 Da (one H atom difference) for masses up to ~100 Da should be sufficient.

3 General considerations

As was briefly mentioned in section 1, there are two approaches to SVMI implementation. The first [9] is based on the so-called “delayed extraction”, where the ionization occurs in the absence of electric fields, the ion cloud is allowed to expand for a predetermined amount of time and is then accelerated towards the detector using a pulsed electric field. The TOF dispersion ($v_z \mapsto t$ part) is achieved basically by mapping the *positions* at the moment of the field switching

$$z(t_{\text{delay}}) = \delta z + v_z \cdot t_{\text{delay}} \tag{8}$$

to the arrival times. This obviously requires that the setup does not meet Wiley–McLaren space-focusing conditions. However, (8) still contains the initial position

$\delta z = z(0)$. Therefore, either the technique cannot be applied to VMI studies with extended ionization regions, or a complicated analysis of the possibility to suppress the δz term while retaining the $v_z \cdot t_{\text{delay}}$ term in the $z(t_{\text{delay}}) \mapsto t$ mapping is required.[1] Moreover, the transversal expansion of the ion cloud before the extraction makes the transversal focusing (for the $(v_x, v_y) \mapsto (x, y)$ part) more demanding. Yet another potential complication is that for reliable operation of the system the time-dependent electric field must have well-defined and stable characteristics. This requires an electronic circuit that can switch a finely controllable kilovolt-range voltage in a few nanoseconds without producing noticeable ringing. The latter, in turn, requires very good impedance matching between the electric pulser and the ion-optical assembly to which the voltage is applied. Since the dimensions of the system are not negligible compared to the "wavelength"[2], the whole problem might require solution of time-dependent Maxwell equations in nontrivial geometry and with real nonperfect conductors and dielectrics. As a result of these difficulties, the rational design, optimization and implementation of the system become an intricate task.

Fortunately, the second approach [10, 11] to SVMI implementation involves only electrostatic fields for velocity mapping and focusing purposes and therefore avoids the complications described above. Therefore, all the following analysis deals only with electrostatic systems.

3.1 Exact relationships

As a starting point, consider the behavior of a charged particle in an electric field with fixed geometry in a general case. The equation of motion with initial conditions is

$$\begin{cases} m\dfrac{d^2\mathbf{r}(t)}{dt^2} = q\mathbf{E}\big(\mathbf{r}(t)\big), \\ \dfrac{d\mathbf{r}(0)}{dt} = \mathbf{v}_0, \\ \mathbf{r}(0) = \mathbf{r}_0, \end{cases} \tag{9}$$

where m is the mass of the particle, q is its electric charge, and $\mathbf{E}(\mathbf{r})$ is the electric field that depends on coordinates (but not on time explicitly). The general properties of the motion can be studied by finding the invariants of (9). For that purpose it is

[1] No attempts of such analysis were known to me at the time of the present work.

[2] The electric field propagation speed in vacuum is $c \approx 30$ cm/ns and is even smaller in waveguides, including the one formed by the ion optics, its surroundings and connections.

convenient to rewrite the electric field in the whole space as

$$\mathbf{E}(\mathbf{r}) \equiv E \cdot \mathbf{f}(\mathbf{r}), \tag{10}$$

where E is a scalar constant describing the overall field strength (can be chosen as $E = |\mathbf{E}(0)|$), and $\mathbf{f}(\mathbf{r})$ is a vector function describing the coordinate dependence of the field. In addition, a scaling substitution

$$\begin{cases} t' = \alpha t, & \text{(11a)} \\ m' = \beta m, & \text{(11b)} \\ q'E' = \gamma q E & \text{(11c)} \end{cases}$$

with arbitrary constants α, β and γ can be made into (9) to obtain

$$\begin{cases} \dfrac{\beta}{\alpha^2}\, m \dfrac{d^2\mathbf{r}(\alpha t)}{dt^2} = \gamma\, q \mathbf{E}\big(\mathbf{r}(\alpha t)\big), \\ \dfrac{1}{\alpha}\, \dfrac{d\mathbf{r}(0)}{dt} = \mathbf{v}_0{}', \\ \mathbf{r}(0) = \mathbf{r}_0{}'. \end{cases} \tag{12}$$

It is obvious from comparison of (9) and (12) that the form of the solution does not change if

$$\begin{cases} \dfrac{\beta}{\alpha^2} = \gamma, & \text{(13a)} \\ \mathbf{v}_0{}' = \dfrac{1}{\alpha}\mathbf{v}_0, & \text{(13b)} \\ \mathbf{r}_0{}' = \mathbf{r}_0. & \text{(13c)} \end{cases}$$

The last equation, (13c), simply tells that in order to have the same trajectory the initial position of the particle should not change. The preceding equation (13b) defines the scaling of the initial velocity. It would also be useful to consider how the initial kinetic energy K_0 should scale:

$$K_0' = \frac{m'(v_0')^2}{2} = \frac{\beta}{\alpha^2}\frac{m v_0^2}{2} = \frac{\beta}{\alpha^2} K_0. \tag{14}$$

Comparison of (14) with (13a) and (11c) immediately yields that

$$\frac{K_0'}{q'E'} = \frac{K_0}{qE} = \text{const} \tag{15}$$

is an invariant of (9). An important property of (15) is that it does not depend on the particle mass. That is, all singly charged ions with identical initial kinetic energies (and identical initial velocity directions) have identical trajectories in a given electrostatic field. If the field direction is reversed ($E' = -E$), electrons with the same K_0 will also have the same trajectories. This fact reveals that in the electrostatic implementation of VMI the initial kinetic energy is a more fundamental (and often more convenient) quantity than the initial velocity or the initial momentum.[1] Another important observation is that the imaged kinetic energy range is directly proportional to the electric field strength. That is, the image magnification (the $(v_x, v_y) \mapsto (x, y)$ part) can be easily controlled by proportional scaling of all voltages applied to the ion optics.

Other useful invariants can be obtained if some parameters are fixed. The first invariant is related to the behavior of different particles in the same electric field ($E' = E$).[2] According to (11), it corresponds to $\gamma = 1$ and thus, from (13a), to $\beta/\alpha^2 = 1$, or $K_0' = K_0$. That is, the only free parameter is the particle mass. Substitution of (11) into $\beta/\alpha^2 = 1$ yields

$$\frac{t'}{\sqrt{m'}} = \frac{t}{\sqrt{m}}, \quad \text{or} \quad \frac{t'}{t} = \sqrt{\frac{m'}{m}}. \tag{16}$$

[1]The role of kinetic energy can be understood from Maupertuis' principle (see §44 in [15]), which determines the trajectory of a mechanical system in a time-independent potential. The abbreviated action extremum conditions for a single particle in an external potential $U(\mathbf{r})$ can be written explicitly: $\delta \int_{\mathbf{r}_0}^{\mathbf{r}} \sqrt{2m\big([K_0 + U(\mathbf{r}_0)] - U(\mathbf{r})\big)}\,|d\mathbf{r}| = 0$. Obviously, the coordinate-independent mass m can be taken outside the integral and the variation without changing the variational equation and thus its solution — the trajectory. The same reasoning applies to a common scaling factor for K_0 and U. In other words, the trajectory is determined by the K_0/U ratio, but not by K_0 or U separately, which is reflected in (15) where the denominator is related to U as $dU = -q\mathbf{E}\,d\mathbf{r}$.

These arguments do not hold for time-dependent electric fields (the interaction depends not only on the particle position, but also explicitly on time) and for magnetic fields (the interaction depends on velocity and cannot be described by a potential, although static magnetic fields do not affect the kinetic energy of electrically charged particles), thus the trajectories in such fields generally *do* depend on the particle mass.

[2]Henceforth only singly charged ions or electrons are considered. It is also implicitly assumed that the particles are positively charged (cations); for negatively charged particles (anions, electrons) the electric field should be reversed.

In other words, the TOF is directly proportional to the square root of the particle mass, if all other parameters are fixed. This forms the foundation of the TOF-MS operation. It also allows mass-selectivity in (S)VMI and will be important in the further analysis of the temporal characteristic of the SVMI system.

The second invariant is related to the behavior of the same particle ($m' = m$) in different electric fields. This corresponds to $\beta = 1$ in (11). Although the kinetic energy scaling was already given by (15) for the general case, we will be mostly interested in the "central" TOF, t_0, of the ion cloud, that is in the behavior of the particles with $\mathbf{v}_0 = 0$, or $K_0 = 0$ (this case satisfies (13b) automatically). Substitution of (11) into $1/\alpha^2 = \gamma$ (from (13a)) yields

$$t_0' \sqrt{E'} = t_0 \sqrt{E}, \quad \text{or} \quad \frac{t_0'}{t_0} = \sqrt{\frac{E}{E'}}. \tag{17}$$

In other words, the central TOFs for particles of each mass are inversely proportional to the square root of the electric field strength (or, equivalently, the square root of the applied voltages), if the field geometry is fixed. Combination of (16) and (17) gives the general TOF dependence

$$t_0 \sim \sqrt{\frac{m}{E}}. \tag{18}$$

3.2 Approximate relationships

Now the properties related to the velocity mapping (1) shall be studied. Unfortunately, this cannot be done in a general form, as in the previous subsection, and thus some restrictions and approximations appropriate for the considered SVMI systems must be made. One of such restrictions is that only electric fields with cylindrical symmetry around the z axis will be considered. This restriction does not reduce the design freedom and is even desirable for an SVMI system. Namely, it means that all directions in the (x, y) plane are equivalent, and the system does not introduce any artificial anisotropy in the $(v_x, v_y) \mapsto (x, y)$ part of the mapping. It also entails that the mapping conserves the angle θ (see figure 1). With that in mind, the "radial" velocity

$$v_r \equiv \sqrt{v_x^2 + v_y^2} \tag{19}$$

is introduced,[1] which is mapped to the radius $R = \sqrt{x^2 + y^2}$ at the detector.

The first task is a more detailed determination of the expression for TOF. Since (18) gives the TOF for particles with $\mathbf{v}_0 = 0$, the general dependence can be written as

$$t = t_0 + \tau(\mathbf{v}_0), \tag{20}$$

where $\tau(\mathbf{v}_0)$ defines the TOF–velocity dispersion function ($\tau(0) = 0$), and all terms implicitly depend on m and the electric field. Within the paraxial approximation[2] the exact equations of motion (9) can be approximately separated into the axial and radial parts. The axial part is then

$$\begin{cases} m\dfrac{d^2z(t)}{dt^2} = qE_z\big(z(t)\big), & \text{(21a)} \\ \dfrac{dz(0)}{dt} = v_z, \\ z(0) = z_0, \end{cases} \quad \text{(21b)}$$

and still contains the field $E_z(z)$ in an arbitrary form.

In order to obtain an explicit (although approximate) dispersion function $\tau(v_z)$, the field in the vicinity of the ionization region can be approximated with a homogeneous field $E_z(z)|_{z\approx z_0} \approx E_0$ as shown in figure 3. (The justification of this approxima-

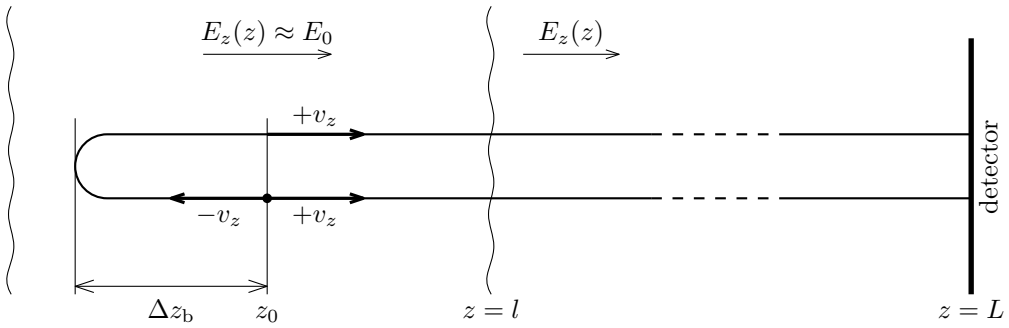

Figure 3 Diagram illustrating the electric field approximation used in the derivation of the TOF velocity dispersion.

tion will be given after the formal derivations of its consequences.) In that case (21)

[1]The index "r" cannot be confused with the radius-vector $\mathbf{r} = (x, y, z)$, since the latter always appears as a vector.

[2]Meaning that the particles do not depart from the z axis significantly, and the axial component E_z of the electric field has very weak dependence on the radial distance r from the axis, at least in the reachable regions.

can be analytically integrated up to $z = l$ ($l \gg z_0$):

$$z(t) = \frac{qE_0}{2m}t^2 + v_z t + z_0, \quad z \leqslant l, \tag{22}$$

and the TOF up to $z = l$ can be found directly:

$$t_l \equiv t|_{z(t)=l} = \frac{-v_z + \sqrt{v_z^2 + 2\dfrac{qE_0}{m}(l - z_0)}}{\dfrac{qE_0}{m}}, \tag{23}$$

where the positive root of the quadratic equation (22) was chosen. This expression can be rearranged as

$$t_l = \underbrace{-\frac{mv_z}{qE_0}}_{t_\mathrm{b}} + \frac{\sqrt{2m}}{qE_0}\sqrt{\underbrace{\frac{mv_z^2}{2}}_{K_z} + \underbrace{qE_0(l - z_0)}_{\Delta U}}, \tag{24}$$

revealing the physical meaning of the participating terms. Namely, $t_\mathrm{b} \equiv -mv_z/qE_0$ is the time required to stop a particle initially flying with velocity $-v_z$ from the detector (see figure 3), K_z is the initial kinetic energy (K_0) component associated with motion along the z axis, and ΔU is the energy gained by the particle from the electric field. Taking into account that $\Delta U \gg K_z$ (see below), the first term under the root can be treated as a small parameter, which yields

$$t_l = -\frac{mv_z}{qE_0} + \sqrt{\frac{2m(l - z_0)}{qE_0}} + O\left(\left(\frac{v_z}{v_{\Delta U}}\right)^2\right), \tag{25}$$

where

$$v_{\Delta U} \equiv \sqrt{\frac{2\Delta U}{m}} \gg v_z \tag{26}$$

is the characteristic speed gained due to the acceleration,[1] and $O(...)$ contains quadratic and higher-order terms in the small parameter $v_z/v_{\Delta U}$. Notice that the velocity-independent term in (25) is proportional to $\sqrt{m/E_0}$ in full agreement with the general result (18).

The subsequent behavior of the particle can be described by formal integration of

[1] In particular, $v_{\Delta U}$ is the "central" (see p. 17) speed at $z = l$.

(21a) starting from $z = l$,

$$\begin{cases} m\dfrac{d^2z(t)}{dt^2} = qE_z\big(z(t)\big), \quad t \geqslant t_l, \\ \dfrac{dz(t_l)}{dt} = v_l, \\ z(t_l) = l, \end{cases} \tag{27}$$

where the velocity $v_l \equiv v(t_l) = v|_{z=l}$ can be obtained by plugging (25) into $v(t) = \frac{qE_0}{m}t + v_z$ or simply from energy conservation:

$$v_l = \sqrt{\frac{2(K_z + \Delta U)}{m}} = v_{\Delta U} + O\left((v_z/v_{\Delta U})^2\right). \tag{28}$$

For the TOF from $z = l$ to the detector ($z = L$) the integration yields[1]

$$t_{l\to L} = \int_l^L \frac{dz}{\sqrt{\frac{2q}{m}\int_l^z E_z(z')dz' + v_l^2}}, \tag{29}$$

which depends on the initial velocity v_z only through v_l given by (28) and thus has the same weak dependence:

$$t_{l\to L}(v_z) = t_{l\to L}(0) + O\left((v_z/v_{\Delta U})^2\right), \tag{30}$$

where

$$t_{l\to L}(0) = \sqrt{\frac{m}{2q}}\int_l^L \frac{dz}{\sqrt{E_0(l - z_0) + \int_l^z E_z(z')dz'}} \tag{31}$$

(notice again the $\sqrt{m/E}$ factor). This, together with (25), allows to write the two terms in (20) for the total TOF as

$$t_0 = \sqrt{\frac{2m(l - z_0)}{qE_0}} + t_{l\to L}(0) \tag{32}$$

[1]Since the transition from (27) to (29) is not so obvious, here is a hint: the first step involves multiplication of the first equation by dz and the rearrangement $\frac{d^2z}{dt^2}dz = \frac{d\left(\frac{dz}{dt}\right)}{dt}dz = \left(\frac{dz}{dt}\right)d\left(\frac{dz}{dt}\right)$, after which the subsequent steps are trivial. See also §11 in [15] for derivations of an equivalent expression from energy conservation.

and

$$\tau(\mathbf{v}_0) \approx -\frac{m v_z}{q E_0}. \tag{33}$$

That is, the $v_z \mapsto t$ part of the mapping (1) is approximately linear:

$$v_z \mapsto t \approx t_0 - \frac{m}{q E_0} \cdot v_z. \tag{34}$$

The total TOF spread (ion cloud stretching) for particles with initial kinetic energy K_0 is therefore

$$\Delta\tau_{K_0} \equiv \max_{\frac{m v_0^2}{2} = K_0} \tau(\mathbf{v}_0) - \min_{\frac{m v_0^2}{2} = K_0} \tau(\mathbf{v}_0) = \frac{2\sqrt{2mK_0}}{q E_0}. \tag{35}$$

It should be noted that (35) is in fact a stronger result than the relation (33). Namely, a properly operating SVMI setup should not significantly distort the shape of the ion cloud, so that even if there are deviations from (33), the shortest TOF should still correspond to the particles initially flying directly towards the detector, and the longest — to those flying in the opposite direction, as illustrated in figure 3. The latter particles after the "turnaround time" $t_{\mathrm{TA}} = 2t_b$ (see (24)) return to their initial position but with the exactly reversed initial velocity,[1] and thus after that point their behavior is *exactly* identical to that of the former particles. It means that the TOF difference is exactly equal to t_{TA} and is determined by the electric field *only* in the small interval Δz_{b}.

Another important fact that should be mentioned here is that the TOF velocity dispersion (33) (and the TOF stretching (35)) is inversely proportional to the electric field strength, in contrast to the central TOF (18), which is inversely proportional to its square root. This has important implications for both SVMI and TOF-MS, as will be shown in a moment.

The justification of the assumptions involved in the derivation of the above results should now be given. As discussed on p. 13, the required TOF stretching is few tens nanoseconds. Solving (35) to obtain, for example, $\Delta\tau_{K_0} = 50$ ns for hydrogen ions with $K_0 = 1$ eV gives the required field $E_0 \approx 58$ V/cm. The maximum value of $\Delta z_{\mathrm{b}} = K_0/(qE_0)$ is then only about 0.17 mm — even smaller than the initial position uncertainty (see p. 12), which indicates that formula (35) can be actually considered exact for all practical purposes. The characteristic size of the VMI ion op-

[1] The trajectory schematically shown in the figure is vertically unfolded for clarity.

tics elements is of the order of a few centimeters, defining the length scale for the spatial electric field variation. Therefore, the choice of $l \sim 1$ cm gives a reasonable estimation for the region where the field can be treated as approximately homogeneous (see figure 3). Thus $\Delta U \sim 58$ eV in (24) is indeed much larger than K_0, and $(v_z/v_{\Delta U})^2 \leqslant K_0/\Delta U \sim 1/58$ in (25) is also a small parameter. The numerical simulations described in section 5 in fact show that the main factors determining the inaccuracy in (33) are deviations from paraxial approximation, and they become noticeable only when the ion-optical system operates in unfavorable conditions.

For investigation of the TOF-MS resolution and the $v_r \mapsto R$ part of the mapping a more explicit expression for the central TOF (32) is required. It can be obtained for the practically important field configuration shown in figure 4 where the particles are

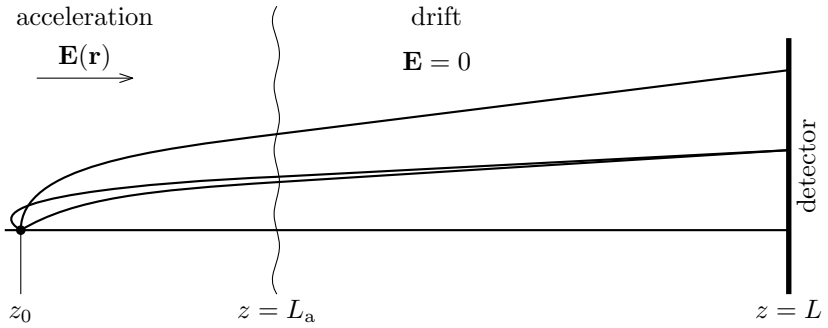

Figure 4 Ion optics configuration with a field-free drift region.

accelerated by the electric field only in a limited "acceleration" region from z_0 to L_a and then fly to the detector through a field-free "drift" region. The subradical integral in (31) then changes only in the $z_0 \leqslant z \leqslant L_\mathrm{a}$ region, and thus the main integral can be split into two parts, $\int_l^L = \int_l^{L_\mathrm{a}} + \int_{L_\mathrm{a}}^L$, with the second part having no z-dependence. The total expression for the central TOF (from z_0) then becomes

$$t_0 = \sqrt{\frac{m}{2q}} \int_{z_0}^{L_\mathrm{a}} \frac{dz}{\sqrt{\int_{z_0}^{z} E_z(z')\,dz'}} + \sqrt{\frac{m}{2qV_0}}(L - L_\mathrm{a}), \tag{36}$$

where

$$V_0 \equiv \int_{z_0}^{L_\mathrm{a}} E_z(z)\,dz \tag{37}$$

is the total acceleration voltage (electric potential difference between the initial po-

sition z_0 and the drift region). The expression (36) shows that the total TOF grows linearly with the total length of the VMI setup, and if L_a is relatively short,

$$t_0 \approx \sqrt{\frac{m}{2qV_0}} L \sim L \cdot \sqrt{\frac{m}{E}}. \tag{38}$$

The mass resolution is determined by the maximum mass for which the TOF distribution does not overlap with that of the next mass. Therefore, assuming ideal TOF spatial focusing and a characteristic kinetic energy K_0 for particles of mass m and $m + 1$ Da, the masses are resolved if

$$\frac{1}{2}\Delta\tau_{K_0}(m) + \frac{1}{2}\Delta\tau_{K_0}(m + 1\ \mathrm{Da}) \leqslant t_0(m + 1\ \mathrm{Da}) - t_0(m). \tag{39}$$

Substitution of (38) and (35), with an assumption $m \gg 1$ Da, yields

$$\frac{1}{2}\Delta\tau_{K_0}(m) + \frac{1}{2}\Delta\tau_{K_0}(m + 1\ \mathrm{Da}) \sim \frac{\sqrt{mK_0}}{E}, \tag{40}$$

$$t_0(m + 1\ \mathrm{Da}) - t_0(m) \sim L\sqrt{\frac{m + 1\ \mathrm{Da}}{E}} - L\sqrt{\frac{m}{E}} \sim \frac{L}{\sqrt{mE}}, \tag{41}$$

and hence the maximal resolved mass

$$m_\mathrm{max} \sim L\sqrt{\frac{E}{K_0}}. \tag{42}$$

For each particular setup it can also be expressed more quantitatively through the parameters for hydrogen ion ($m = 1$ Da):

$$m_\mathrm{max} \approx \frac{t_0(\mathrm{H}^+)}{2\Delta\tau_{K_0}(\mathrm{H}^+)}. \tag{43}$$

This dependence immediately shows one of the mentioned contradictory requirements for SVMI and TOF-MS. Namely, the mass resolution is higher for stronger electric fields, where $\Delta\tau_{K_0}$ is smaller, but the slicing conditions require a specific finite $\Delta\tau_{K_0}$ value and thus generally relatively weak fields (see p. 21). In principle, if the TOF-MS and SVMI modes are used independently, then a strong field can be set in one mode and a weaker field in the other. However, designs optimized for TOF-MS operation benefit from using a long drift region (according to (42)) and a very

short acceleration region (figure 4) in order to maximize E_0 in (35) without inflating V_0 in (36). At the same time, such geometrical parameters are usually unfavorable for SVMI because they lead to an expansion of the image size at the detector plane beyond the desirable limits.

Namely, the radial velocity component $v_r(t)$ inside the acceleration region depends linearly (in paraxial approximation) on its initial value v_r:

$$v_r(t) \approx v_r \cdot g(t), \tag{44}$$

where $g(t)$ is a system-dependent function, and is (exactly) conserved in the field-free drift region:

$$v_r(t > t_\mathrm{a}) = v_r(t_\mathrm{a}), \quad \text{or} \quad g(t > t_\mathrm{a}) = g(t_\mathrm{a}), \tag{45}$$

where t_a is the time spent in the acceleration region ($z(t_\mathrm{a}) = L_\mathrm{a}$). Therefore, the image radius at the detector

$$R = r_0 + \int_0^{t(\mathbf{v}_0)} v_r(t)\,dt = r_0 + v_r \left[\int_0^{t_\mathrm{a}} g(t)\,dt + g(t_\mathrm{a}) \cdot (t_0 - t_\mathrm{a}) + O\left(\tau(\mathbf{v}_0)/t_0\right) \right] \tag{46}$$

is directly proportional to the radial component of the initial velocity as well. That is, the radial part of the velocity mapping

$$v_r \mapsto R \approx \mathrm{const}\, t_0 \cdot v_r \tag{47}$$

is also approximately linear (compare to (34)) with a system-dependent proportionality constant. For $t_\mathrm{a} \ll t_0$ (that is, $L_\mathrm{a} \ll L$) the image size scales as

$$R \sim L\sqrt{\frac{K_r}{V_0}} \sim L\sqrt{\frac{K_0}{E}}, \tag{48}$$

where the "radial kinetic energy" $K_r \equiv m v_r^2/2$ and (38) were substituted.[1] Hence the use of a long drift region and very short acceleration region optimal for TOF-MS would lead to a very large image size due to the L proportionality in (48) and very small V_0 caused by the required weak field E_0 and short L_a in (37).

[1] Notice again that R depends on the K_0/E ratio and does no depend on the particle mass, in agreement with the general result (see p. 16).

A few remarks should be made about the radial part (47) of the velocity mapping (1). First, the original expression (46) contains a weak dependence on the initial axial velocity component through the $t(\mathbf{v}_0)$ dependence on it. If a more accurate TOF from (34) is substituted into (47) instead of t_0, the overall velocity mapping becomes

$$(v_r, v_z) \mapsto \left(\text{const}\left[t_0 - \tfrac{m}{qE_0}\cdot v_z\right]\cdot v_r,\; t_0 - \tfrac{m}{qE_0}\cdot v_z\right). \tag{49}$$

That is, a small cross-term $v_z v_r$ appears in the radial part. This term is not related to any approximations and disappears only in the limit $\Delta\tau_{K_0}/t_0 \to 0$ (meaning $t_0 \to \infty$, since $\Delta\tau_{K_0}$ must have a finite value). In practice it means that in the projection–reconstruction approach (see p. 8) the inverse Abel transform can be applied only when $\Delta\tau_{K_0} \ll t_0$, which is in fact usually satisfied in modern VMI setups.[1] The cross-term has no effect in SVMI of cylindrically symmetric distributions, since only the slice with $v_z = 0$ is recorded. In SVMI of general distributions the correction according to the selected v_z value can be easily done regardless of the $\tau(\mathbf{v}_0)/t_0$ ratio.

The second remark, related to the issue emphasized on p. 21, is crucial for SVMI and concerns the different dependences of the axial and radial parts of the mapping on the electric field strength. Namely, for a fixed field geometry the TOF spread (35) is proportional to $\sqrt{K_0}/E$, whereas the image size (48) is proportional to $\sqrt{K_0/E}$, which means that, in general, fulfillment of slicing conditions and selection of appropriate image size at the detector cannot be achieved simultaneously. In other words, an SVMI setup intended for measurements in variable kinetic energy ranges must necessarily permit creation of electric fields with variable geometries.

4 Ion optics

This section is devoted to an overview of ion optics concepts and historical examples of their application to the VMI problem. This information serves as an illustration of the general principles and is important for understanding the limitations of these simple systems and the means to overcome these limitations.

[1] See [16] for a detailed discussion and a reconstruction method for the $\Delta\tau_{K_0} \not\ll t_0$ case. Please note that the electrostatic optical system described there has no field-free drift region and thus has a poor $\tau(\mathbf{v}_0)/t_0$ ratio, so that the values of their ρ parameter (equal to qV_0/K_0 in the present notation) required for nearly parallel projection would be somewhat overestimated for modern systems.

4.1 Wiley–McLaren arrangement for TOF spatial focusing

As mentioned in the introduction, the conditions required for making the TOF independent on the initial positions of the ions were studied by Wiley and McLaren in 1955 [3] in the context of TOF mass spectrometer. Since they were not interested in the initial radial position and velocity distributions of the particles, a 1-dimensional electric field configuration was chosen for simplicity. In other words, the axial part (21) of the equations of motion provided an exact description of the problem.

Another simplification of the problem was to limit the field configuration to a few regions of homogeneous electric field. From a practical perspective, such field configuration is easily created by applying different voltages to a few mutually parallel grids installed perpendicular to the TOF axis as illustrated in figure 5. The grids

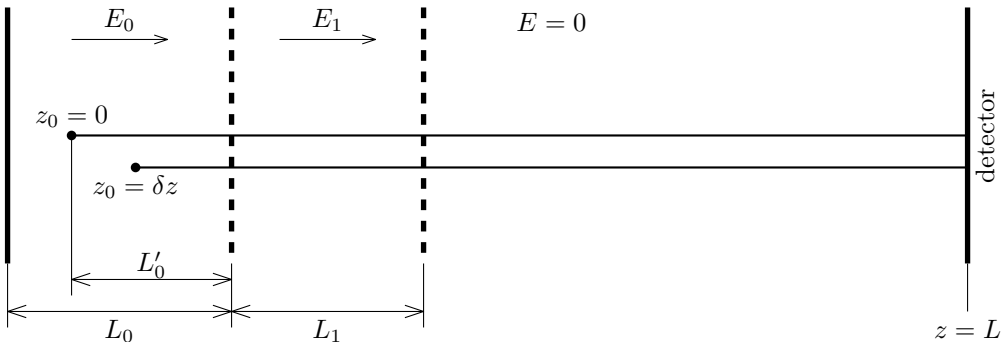

Figure 5 Geometry of Wiley–McLaren TOF mass spectrometer as an example of a system with TOF spatial focusing.

(meshes) must have sufficiently high open area ratio in order to transmit the particles and, at the same time, sufficiently small cell size in order to keep the electric field on both sides nearly homogeneous.[1] Such simple $E_z(z)$ dependence allows facile analytical evaluation of the integrals in (36) and (37) and therefore results in a relatively simple analytical expression for the total TOF.

Without going into details, which can be found in [3], the idea of the focusing can be understood from very simple considerations. Namely, ions originated farther from the detector spend more time in the accelerator region than ions originated closer to the detector (the first term in (36) increases when z_0 decreases), but acquire higher energy from the electric field and thus fly through the drift region faster (the second

[1]The depth (distance from the grid plane) of field inhomogeneities is comparable to the mesh opening diameter, so, for example, the field between two grids with densities of the order of ~10 mm^{-1} separated by a few centimeters can be considered as homogeneous with very high accuracy.

term in (36) decreases with z_0 because V_0 in (37) grows). Therefore, at some point in time these ions should meet in the drift region. Existence of more than one region of homogeneous electric field allows to vary V_0 (which determines the final energy $K = qV_0$) independently of E_0 (which determines the energy difference $\delta K = -qE_0\delta z$) for matching the "focal length" of the system to the detector position. In fact, two regions (as depicted in figure 5) are already sufficient for that purpose.

Quantitative analysis gives a relatively simple analytical expression (see [3]) for the dependence of the focal length F_t on the two accelerator lengths L'_0 and L_1 and the field strengths ratio E_1/E_0. The dependence is illustrated in figure 6, which

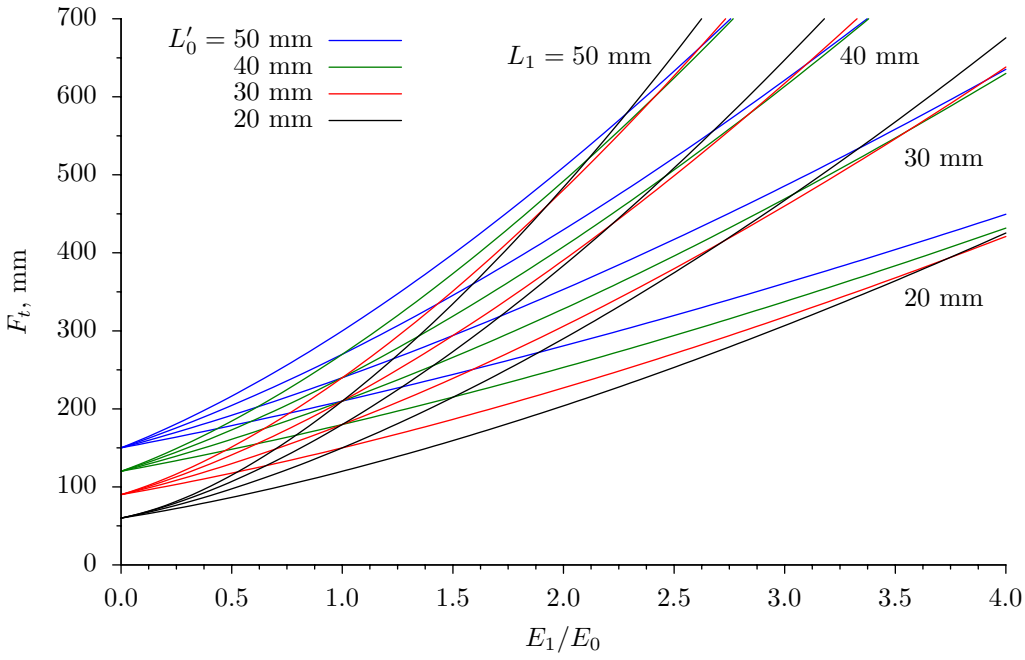

Figure 6 Focal length for TOF spatial focusing in the Wiley–McLaren system (see fig. 5).

makes clear that F_t can be varied in a very broad range by adjusting any of the parameters, especially the E_1/E_0 ratio. This last fact is quite useful from a practical perspective, since the applied voltages that determine E_0 and E_1 for given L'_0 and L_1 are the most easily controllable parameters. The prominent increase of F_t with L_1 is mostly due to the increase in the final kinetic energy — the particles have higher velocity in the drift region and thus meet at a longer distance.

One interesting feature of the general dependence also visible in the plots is that in the case of a single acceleration field (that is, $E_1 = 0$) the focusing is still present,

and $F_t = 3L'_0$.[1] However, in light of the remark made on p. 25, such configuration is not very suitable for the SVMI needs because the field geometry depends on only one parameter $L'_0 = L/3$, whereas the two-field configuration has 3 degrees of freedom $\{L'_0/L, L_1/L, E_1/E_0\}$.

In more complex geometries, including 2-dimensional field configurations[2], the dependence of F_t on the field geometry becomes more complicated, and its determination usually requires numerical integration. However, the general qualitative relation to E_0 and V_0 is preserved.

4.2 Eppink–Parker arrangement for radial focusing

The first ion-optical system able to perform spatial focusing in the radial direction, that is to make the arrival positions of the particles independent on their initial positions, was studied by Eppink and Parker in 1997 [7] and is surprisingly similar to the Wiley–McLaren arrangement. The only difference is that the two grids are replaced by apertures — flat electrodes with circular opening of finite radius, as shown in figure 7. The finite size of the opening breaks the homogeneity of the electric fields

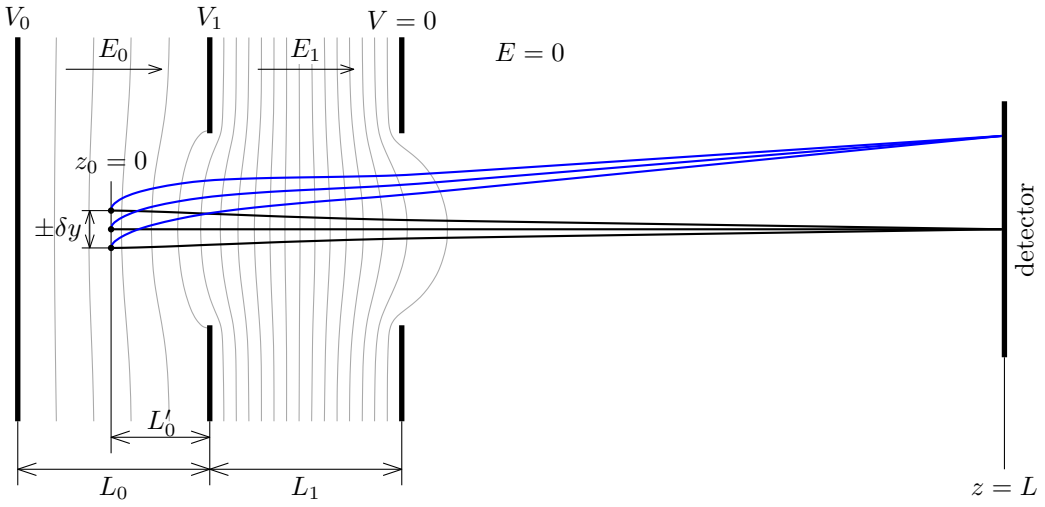

Figure 7 Cross-section of Eppink–Parker VMI setup for radial focusing. Electric field configuration is illustrated by gray equipotential contours. Sample ion trajectories are shown in black for $\mathbf{v}_0$ parallel to the z axis and in blue for $\mathbf{v}_0$ perpendicular to it.

at finite scales comparable to the aperture radii. Since the electric potential $\varphi(r,z)$ in

[1] In addition, when $E_1/E_0 = 1$, the configuration is also effectively a single field region of length L'_0+L_1. In that case $F_t = 3(L'_0+L_1)$, which is also evident from the figure.

[2] Meaning cylindrically symmetric geometry, see p. 17.

free space satisfies the Laplace's equation

$$\frac{1}{r}\frac{\partial}{\partial r}\left(r\frac{\partial \varphi}{\partial r}\right)+\frac{\partial^2 \varphi}{\partial z^2}=0, \tag{50}$$

any inhomogeneities must lead to appearance of a non-zero radial component of the electric field

$$E_r(\mathbf{r})=-\frac{\partial \varphi(\mathbf{r})}{\partial r}\neq 0. \tag{51}$$

Moreover, the fact that $\frac{\partial^2 \varphi}{\partial z^2}$ is finite, in conjunction with (50), leads to the paraxial dependence

$$E_r(r)\sim r, \tag{52}$$

which has the form exactly suitable for focusing of charged-particle beams.

The focusing properties of these so-called "aperture electrostatic lenses" were actually known since at least 1932 when Davisson and Calbick studied them theoretically and experimentally [17][1], and were widely used in many charged-particle beam applications including *imaging* devices such as cathode ray tubes and electron microscopes (since the same early 1930s [19]). The exceptionally long delay in the adoption of these ideas in the VMI was probably caused by two factors. The first is that the charged-particle optics and reaction dynamics of free molecules were quite separated fields. In principle, even though TOF spectrometers that were used in the latter can have "optical" elements in electron guns and ion beam collimators and reflectors, they were not intended to produce a meaningful spatial distribution that could be analyzed. The second factor is that VMI systems are *not imaging systems from the optical point of view*. Namely, an optical system is classified as "imaging" if it produces a real image of a real object. In other words, it should map points from the object space to points in the image space. On the contrary, VMI systems produce a real image of a velocity distribution, that is they map "points" from the velocity space (beam directions and speeds) to points in the image space.[2] In the context of optics such systems can be classified as telescopic objectives. At the same time, their input

[1]Their first communication appeared in 1931 as APS meeting abstract (p. 585 in [18]), but it was related to slit apertures which behave somewhat differently from circular apertures.

[2]Therefore, the terminology must be used carefully to distinguish the "*velocity map* imaging" from the truly *imaging* techniques such as "ion imaging" in "imaging mass spectrometry" (see, for example, [20]), as well as from various "velocity mapping" techniques, which provide spatial distribution of flow velocity in media (for example, of blood flow [21]).

lens is of the immersion type. This is a quite extraordinary combination, meaning that even familiarity with the usual devices based on charged-particle optics would not immediately give an idea of the VMI possibility.

The behavior of charged particles in electric field configurations formed by apertures can be studied using analytical approximations (see [22] for an example). In particular, they show that the focal length f of the aperture lens, in the first approximation, does not depend on its diameter and is determined by the ratio of the particle kinetic energy at the lens plane to the difference between the electric field strengths in the regions separated by the aperture:

$$f = \frac{4K(z_{\text{lens}})}{q(E_{z>z_{\text{lens}}} - E_{z<z_{\text{lens}}})}. \tag{53}$$

This dependence has two important properties. First, the focal length is directly proportional to the kinetic energy of the particle. This fact reveals that electrostatic lenses have very high "chromatic aberrations" (dependence of the refraction on the energy).[1] In addition, since electric fields exist before and after the lens, the kinetic energy of the particles constantly changes as they fly through the system, so the properties of a lens substantially depend on its location. Second, the lens is asymmetric. Namely, it is converging ($f > 0$) if the field increases along the path, and diverging ($f < 0$) if the field decreases.[2] In application to the system shown in figure 7 it means that the first aperture works as a positive lens, and the second one — as a negative, but since the kinetic energy at the second lens is higher than at the first, the overall result is positive (if the second field is sufficiently strong). All the mentioned effects can be noticed in the figure.

Although the focusing does not depend on the lens diameter in the first approximation, some dependence emerges if the ions are created within a close distance (comparable to the aperture radius) from the lens plane, as shown in figure 7. In that case the electric field in the ionization region has a nonzero curvature, resulting in initial acceleration towards the axis, which leads to some additional focusing.[3] The

[1] For example, electrostatic lenses have two times different focal lengths for particles with energies K and $2K$, whereas "regular" lenses for visible light have only ~4 % focal length variation for the whole visible spectrum (the same twofold difference in the photon energy $h\nu$).

[2] More precisely, the field projection on the traveling direction is important. If particles are decelerated flying against the field, then "less negative" fields mean a field increase, so (53) and its description do not contradict the time reversal symmetry.

[3] The curvature is nevertheless sufficiently small and can be safely ignored in the analysis given on

position of the leftmost electrode in figure 7 might also affect the focusing, if it is placed close to the lens, since the field is flattened near the electrode surface. However, if the distance from the lens plane exceeds the aperture diameter, the effect is minor.

In any case, numerical simulations become the preferred method for quantitative analysis because they can be performed relatively quickly with modern computers, work equally well in any geometry and have good accuracy. The lack of specific restrictions additionally allows more detailed studies of various aberrations. All characteristics of ion-optical systems reported from this point onwards (as well as the electric potential contours and particle trajectories in figure 7) were obtained by numerical simulations in the ion optics simulation software package SIMION 8 [23, 24] complemented with customized user-programming scripts for analysis of the trajectories and (semi)automatic optimization of the electric field parameters.

An illustration of the radial focusing focal length F_R dependence on L'_0, L_1 and E_1/E_0 for the two-aperture system is given in figure 8. As with the TOF focusing dependence $F_t(L'_0,L_1,E_1/E_0)$ (see p. 27), the radial focal length $F_R(L'_0,L_1,E_1/E_0)$ also can be varied in a very broad range by adjusting any of the parameters, among which the electric field strengths ratio again has the most prominent effect. However, in contrast to F_t, F_R is negative for $E_1/E_0 \lesssim 2$, meaning that the beams actually diverge. This fact is easily understood for $E_1/E_0 < 1$, since in that case both lenses are diverging, as can be seen from (53). When $E_1/E_0 > 1$, the first lens becomes converging, but its optical power $(1/f)$ is proportional to $E_1 - E_0 = ([E_1/E_0] - 1)E_0$, which has smaller magnitude than the proportionality factor $0 - E_1 = -[E_1/E_0]E_0$ for the second, diverging, lens. Nevertheless, the kinetic energy factor in (53) decreases the power of the second lens relative to the first one. The ratio of the kinetic energies strongly depends on both length parameters (L'_0 and L_1), what explains why the threshold ratio $\min\limits_{F_R>0}[E_1/E_0]$ at which the overall optical power becomes positive increases with L_0 and decreases with increasing L_1.[1]

For the sake of completeness, it should be pointed out that if the second aperture is replaced with a flat grid (as in the original Wiley–McLaren system), then only

p. 18.

[1] The distance between the lenses, equal to L_1, also affects the overall optical power through changing the relative position of the focal points of the two lenses, so the dependence on L_1 is not purely due to the kinetic energy dispersion effect.

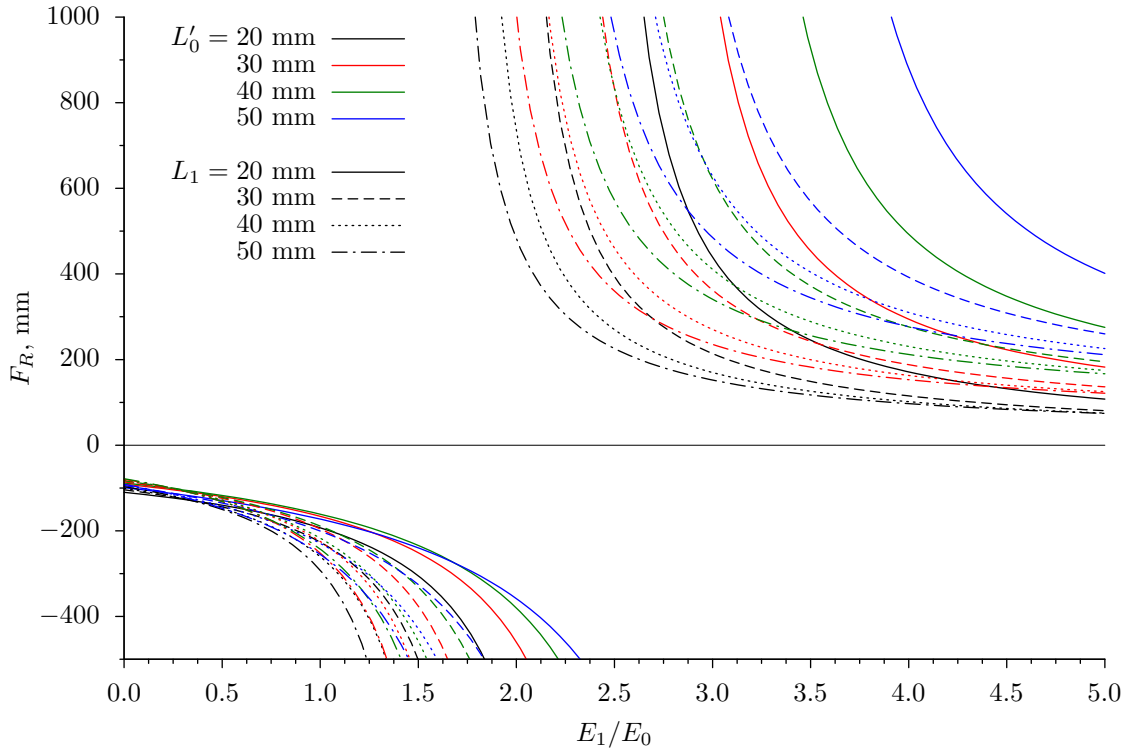

Figure 8 Focal length for radial focusing in Eppink–Parker VMI system (see fig. 7; both apertures have ⌀40 mm, and $L_0 = L'_0 + 15$ mm).

the first, positive, lens remains, making the focusing possible with lower E_1/E_0 ratios. This arrangement, however, does not offer any practical advantages and is even detrimental, since maintaining the grid at sufficiently flat geometry is practically challenging, and the presence of the grid in the beam path decreases the transmission of the system.[1] An additional problem with the grid is that its transmission has spatial dependence, which might introduce artificial patterns in the VMI result.

Another possibility is to extend the second electric field region up to the detector, thus having only one positive lens and no grids. Or to use specially shaped electrodes instead of the flat leftmost plate in figure 7 and the aperture plate in order to create a suitable field curvature in the ionization region for overall focusing effect even with the single aperture working as a negative lens (see [25] for an attempt to use this approach). Such configurations, however, have the same drawback as the single-field TOF focusing (see p. 27), namely, very small freedom of electric field geometry

[1]The Eppink–Parker configuration actually has *ideal* transmission.

variations.[1]

4.3 Minimalistic SVMI system

The fact that the Wiley–McLaren arrangement for TOF focusing and the Eppink–Parker arrangement for radial focusing are very similar suggests that both types of focusing can be achieved simultaneously in a system with two aperture lenses. Indeed, comparison of the F_t dependence shown in figure 6[2] and the F_R dependence shown in figure 8 reveals that for any given $\{L'_0, L_1\}$ the former monotonically grows with E_1/E_0, and the latter monotonically descends. Therefore, for any lengths combination $\{L'_0, L_1\}$ there always exists exactly one electric fields ratio E_1/E_0 at which the F_t and F_R curves cross, so placing the detector at $L = F_t = F_R$ produces the sought VMI system that performs the mapping (1) independently of the initial ion positions.

Hence the parameters required for SVMI operation should satisfy the following conditions:

$$\begin{cases} \Delta t_{\max K_0}(E_0) = \Delta\tau_{\mathrm{S}}, \\ F_t(L'_0, L_1, E_1/E_0) = L, \\ F_R(L'_0, L_1, E_1/E_0) = L, \end{cases} \tag{54}$$

where $\Delta\tau_{\mathrm{S}}$ is the TOF stretching required for slicing (~10 times the effective slicing width, see p. 13). This system of 3 equations has 5 independent variables: $\{L, L'_0, L_1, E_0, E_1/E_0\}$. E_0 is determined by the first equation, and the remaining 2 equations with 4 variables leave 2 degrees of freedom in the solution. From a mathematical point of view, the total length L is a very good choice of a free parameter because, according to (48), it is directly related to the radial magnification constant in (47) and thus allows to change the overall image size independently of the TOF stretching (35). Unfortunately, this approach is rather inconvenient from a practical point of view because for good adjustability of the image size the total length of the apparatus must be variable by several times, which is difficult to perform for a high-vacuum system.[3] Therefore, a more practical approach is to fix the total length at some reasonable value, mostly determined by the desired mass resolution, since L is also the

[1] The variation of electrode shapes in the "single-field" case is too impractical.

[2] As mentioned above, this dependence should be slightly different for the system with apertures instead of grids, but the difference is actually small and not qualitative.

[3] An example of a VMI system with variable total length is described in [26]. Notice, however, that the length change requires a partial disassembly of the vacuum chamber and hence is at least time-consuming.

most important factor in (42). This leaves only one free parameter in (54) that can be used for image size adjustments or minimization of aberrations. The choice of the parameter is not very important, as long as it uniquely determines the solution of (54). In the results reported below the initial acceleration length L_0' was chosen as the independent variable based on its role in affecting the electric field curvature in the ionization region and the kinetic energy at the first lens plane, and through that the aberrations of the whole ion-optical system.

As discussed in sections 3.1 and 3.2, all performance characteristics have simple scaling rules with respect to the overall electric field strength and particle mass. Therefore, numerical simulations for one particular type of ions and one electric field scale are sufficient to completely characterize the system. The natural choice of ions are H^+, since they have "unit" mass ($m = 1$ Da) and are particularly important for the intended application of the designed setup. The natural measure of the overall electric field strength is E_0 (see (54) and the discussion following it), which determines the TOF stretching. The choice $E_0 = 20$ V/cm, of the order of the lowest practical limit, yields $\Delta\tau_{K_0} = 144$ ns for H^+ ions with $K_0 = 1$ eV. This should be sufficient for SVMI of distributions with maximum kinetic energy down to a fraction of an electronvolt, thus satisfying the low-KER limit of the design goals (see p. 11).

The remaining parameters required for numerical solution of (54) are the total length L, the aperture radii and the distance $L_0 - L_0'$ between the terminating electrode and the ionization region. As mentioned above, the total length has a strong effect on the mass resolution and thus must be sufficiently large. The maximum length that could be achieved with the existing apparatus (see the beginning of section 2) by attaching a standard-size extension nipple without additional vacuum pumping is about $L = 600$ mm, which was chosen for these preliminary simulations. Although the aperture radii have small effect on the focal length (see p. 30), they must be several times larger than the expected beam size in order to keep the aberrations at a reasonably low level. A detailed account will be given later, and for now it will be assumed that an aperture diameter comparable to the detector diameter is a sensible choice.[1] Thus, for the sake of simplicity, both aperture diameters were chosen equal to the employed detector diameter, namely 40 mm. The $L_0 - L_0'$ distance has

[1] As explained on p. 24 and is evident from figure 7, the beam expands after the second lens, hence the beam diameter (for particles that can reach the detector) within the accelerator region should be smaller than the detector diameter.

similarly little importance and also does affect the aberrations. However, it is not obvious in advance whether placing the ionization region closer to the flat electrode (for flatter electric field) or farther from it (for more stable field curvature) is better. Therefore, the simulations were performed for several choices of $L_0 - L_0'$ (fortunately, the utilized simulation procedure allows this without much additional effort).

The family of solutions of (54) as dependences of L_1 and E_1/E_0 on L_0' is shown in figure 9 for various $L_0 - L_0'$ values. It is immediately evident that L_1 is an almost

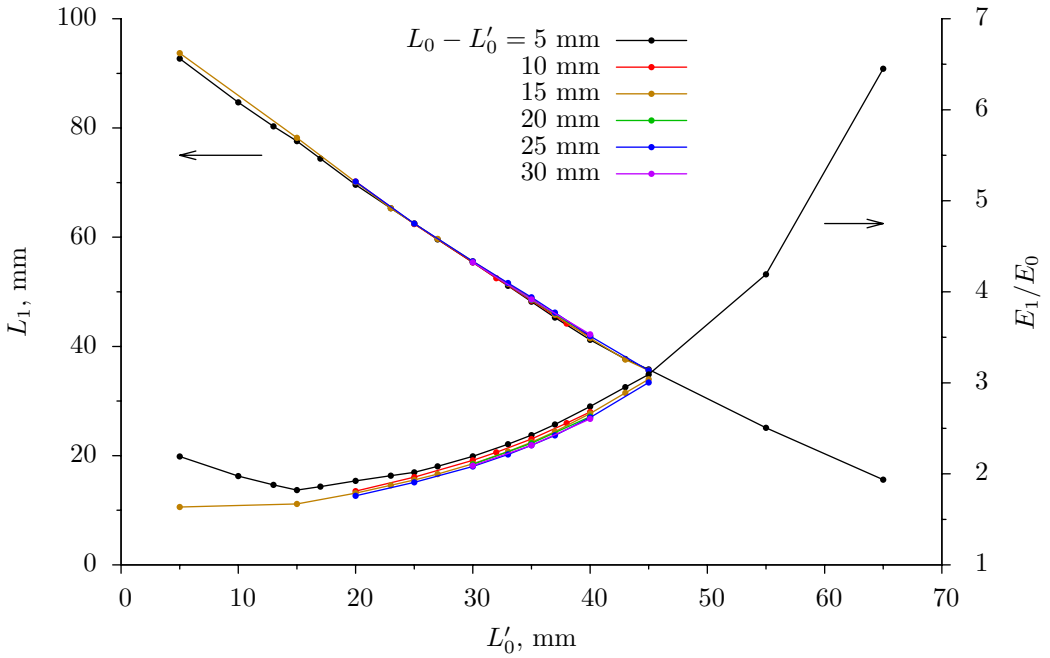

Figure 9 Interdependence of L_0', L_1 and E_1/E_0 for simultaneous TOF and radial focusing in the minimal SVMI system (Eppink–Parker arrangement, see figure 7). Calculated points are connected by straight line segments for clarity.

linear function of L_0', and that any of these lengths indeed uniquely determines the solution. E_1/E_0 is also smooth but has a more nonlinear relation to the lengths. The parameters are essentially independent on the $L_0 - L_0'$ distance, except for the case when both $L_0 - L_0'$ and L_0' are smaller than the aperture radius, which is the expected result (see p. 30). As a matter of fact, the solution allows a very broad selection of one of the parameters L_0', L_1 or E_1/E_0 (plus an almost free choice of $L_0 > L_0'$).

This freedom, as already mentioned, could be used for optimization of the important characteristics of the SVMI system. These characteristics include the total TOF, t_0, (determining the mass resolution by (42), since $\Delta\tau_{K_0}$ is fixed by fixing E_0), the

overall image size at the detector, $\max R$, and the imperfections in TOF and radial focusing (determining the effective slicing width and the achievable perpendicular velocity resolution, respectively).

The focusing imperfections are caused by unavoidable aberrations of ion optics, which lead to mapping of a parallel beam to a finite-size "spot" instead of the ideal "point" (in both arrival time and position). Since the SVMI setup must work well for all kinds of initial velocity distributions, the most relevant description of the focusing imperfections is given by the maximum size of these spots produced for all initial velocities within the whole measured range. Additionally, for photodissociation processes KER is a more interesting quantity than the initial velocity, and hence the relative KER resolution (the ratio of the resolved kinetic energy interval ΔK to the maximum measurable kinetic energy $\max K$) becomes the natural choice for characterization of the radial focusing quality. KER is directly related to the initial velocity of the detected particle. For example, for dissociation into two particles,

$$K = \left(1 + \frac{m}{M}\right) K_0 = \left(1 + \frac{m}{M}\right) \frac{m}{2} \cdot v_0^2, \tag{55}$$

where m is the mass of the detected fragment, and M is the mass of the cofragment. Since the radial mapping $v_r \mapsto R$ is approximately linear (see (47), and $v_r = |\mathbf{v}_0|$ for the central slice), the relative KER resolution can be expressed as

$$\frac{\Delta K}{\max K} \approx \max_{\frac{m v_0^2}{2} \leqslant \max K_0} \frac{2R(\mathbf{v}_0)\Delta R(\mathbf{v}_0)}{(\max R)^2}, \tag{56}$$

where ΔR is the radial spot size.

The simulation results for the performance characteristics are summarized in figure 10. The first noticeable feature of the shown dependences is a somewhat larger influence of the $L_0 - L_0'$ distance, although for its values larger than 5 mm the effect is still rather small. The most important fact evident from the figure is that both the TOF resolution Δt and the relative KER resolution ΔK have a distinct minimum located between $L_0' = 30$ and 40 mm. Perfect focusing is never reached, and the resolution deteriorates noticeably when the free parameter is changed from its optimal value.

The qualitative dependence of the resolution on the initial acceleration length L_0' is easily understood by considering the participating types of aberrations. The

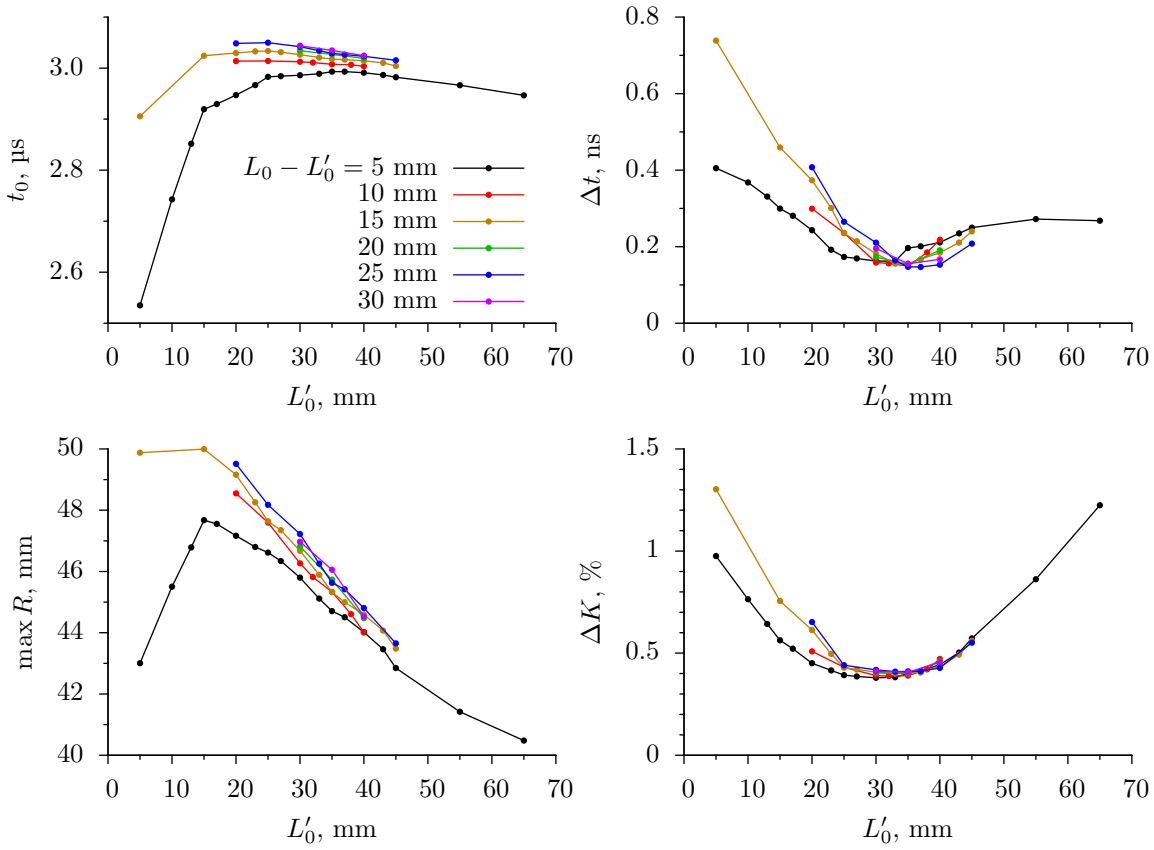

Figure 10 Performance characteristics for the minimal SVMI system under simultaneous TOF and radial focusing conditions.

chromatic aberrations — dependence of the focal length on the kinetic energy in (53) — increase when the relative range of kinetic energies at the first lens plane[1] increases. The absolute range is determined by the initial velocity distribution of the particles, but the average at the lens is governed by the energy gained from the electric field and is approximately equal to qE_0L_0'. Therefore, for smaller L_0' values the relative kinetic energy spread is larger, and the chromatic aberrations are stronger. On the other hand, the geometric aberrations — dependence of the focal length on the distance from the optical axis — are larger for larger beam radii at the lenses (breakdown of paraxial approximation). As can be seen from figure 7, the largest expansion of the beam occurs before the first lens, where the particles did not yet gain a substantial axial velocity but nearly conserved their radial velocities. Therefore,

[1]The relative range at the second lens is always smaller and thus has a smaller effect.

extension of the initial length L'_0 increases the filling factor[1] of the lenses and thus leads to stronger geometrical aberrations. Although these two types of aberrations have opposite L'_0 dependences, they are always present and have different origins, preventing their mutual cancellation. The aperture radius also plays an important role in the aberrations, mostly in the geometrical ones through the filling factor. This means that the *location* of the overall aberrations minimum should depend on the aperture radius. However, the simulations performed with aperture radii larger and smaller than the initially chosen 40 mm showed that the *value* of the minimum does not noticeably change with the radius. Therefore, the radius for which the locations of the minima for ΔK and Δt coincide (as in figure 10) is a wise choice.

As can be seen from the figure, the total TOF is always close to 3 µs and cannot be increased by variation of the parameters, meaning that the mass resolution remains constant and is determined by the total length L. Substitution of $t_0 = 3$ µs and $\Delta\tau_{K_0} = 144$ ns into (43) gives $m_{\max} \approx 10.4$ Da, which is obviously sufficient for separation of the imaged H^+ ions from all other particles, but is also clearly low for the design goal formulated on p. 13. However, this $m_{\max}$ value corresponds to the low-field limit used in the simulations and can be improved according to (42) by increasing the voltages applied to the ion optics. The maximum voltage used in the $E_0 = 20$ V/cm case is ~300 V (also nearly independent on the parameters), thus raising it to the upper practical limit of ~5 kV should yield $m_{\max} \approx 43$ Da for particles with 1 eV maximum initial kinetic energy. This is already acceptable for small organic radicals, as well as for Cl atoms (and HCl), but not for organic molecules containing a Cl atom. Nevertheless, if these heavier molecules have lower initial kinetic energy,[2] the mass resolution for them will be larger. For instance, for $\max K_0 = 0.1$ eV masses up to $m_{\max} \approx 135$ Da become resolved. The conclusion from these estimations is that the mass resolution with the chosen $L = 600$ mm can be considered acceptable, but any significant reduction of the total length would undermine the TOF-MS performance. A significant increase of L is also not particularly necessary regarding the mass resolution demands and would be undesirable due to practical considerations.

The last and the most problematic dependence illustrated by figure 10 is that the overall image radius can be varied by only ~20 %, and this variation would lead to

[1] Ratio of the beam radius to the aperture radius.

[2] For example, all parent molecules in the molecular beam have essentially zero kinetic energy (relative to the beam). Heavy fragments of dissociation processes should also have relatively small kinetic energy, as can be seen from inversion of (55).

deterioration of the kinetic energy resolution by ~3 times, as can be seen from comparison of the corresponding plots. From a practical point of view this means that the adjustable parameter must be used to minimize the aberrations, and the radial magnification can be controlled only by the overall electric field strength scaling according to (48). This unfavorable fact essentially shows that even the two-aperture system does not have sufficient flexibility to solve the problem with correlation between the radial magnification and the TOF stretching (see p. 25).

The overall image radius of ~46 mm for 1 eV ions means that, according to (48), only ions with $K_0 \lesssim 0.2$ eV can be captured by the employed ⌀40 mm detector. The TOF stretching $\Delta\tau_{K_0} \approx 64$ ns for this K_0 is close to the desired value (see p. 13). That is, the design goals for the low-KER limit (see p. 11) are actually satisfied by the considered two-aperture system with a total length close to 600 mm. The situation for higher kinetic energies is worse. For example, even for $K_0 = 1$ eV the electric field strength must be increased from $E_0 = 20$ V/cm to ~100 V/cm in order to fit the whole image into the detector, and at this E_0 value the TOF stretching drops, according to (35), to only $\Delta\tau_{K_0} \approx 27$ ns, which is already insufficient for good slicing. For distributions with higher kinetic energies slicing becomes completely impossible, as the TOF stretching approaches the inherent time resolution of the experiment. This indicates that some additional means for the radial magnification control independent on the initial acceleration field strength E_0 are required.

4.4 Additional lenses

Obviously, the radial image magnification can be controlled by adding more lenses to the ion-optical system. To be specific, only an image size reduction is required from the magnification control, since the original magnification provided by the system described in the previous subsection is large enough for the set experimental goals.

The freedom in selection of the optical scheme for the “zoom” control is somewhat limited by the general properties of electrostatic lenses. As can be seen from figure 8, the focal length is never shorter than a few aperture diameters. Moreover, the aberrations for lenses operating with such short focal lengths are significant. This means that construction of a compact “zoom lens” from many short-focus lenses, as in regular optics, is impossible, at least if high resolution is required. In other words, magnification control by addition of as few as possible relatively weak lenses is desirable.

A single negative lens added after the accelerator would not make any improvement. First, the output lens of the accelerator is already negative. Second, a negative lens increases the divergence of the beam and thus should lead to a higher magnification instead of a lower.

On the contrary, a single positive lens added after the accelerator can perform the desired magnification control, as illustrated in figure 11. The figure shows the

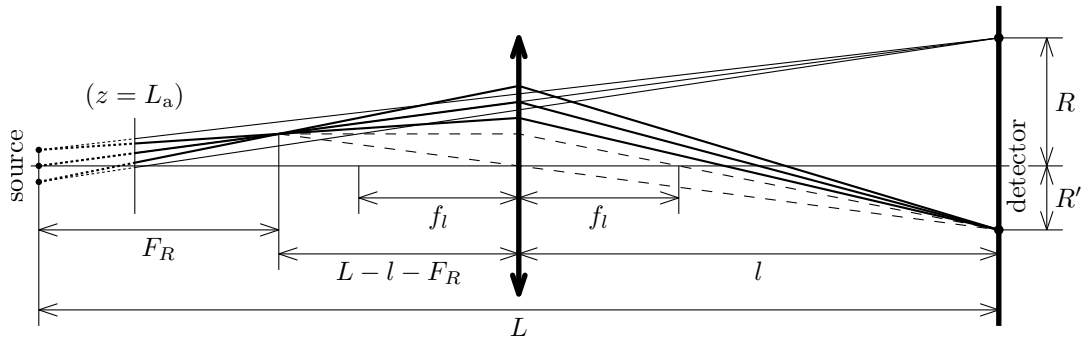

Figure 11 Optical scheme for a positive lens added in the drift region, showing particle trajectories with (thick lines) are without (thin lines) the lens.

most pictorial case, where F_R is positive and short, so that a real image is formed before the additional lens. This allows a trivial derivation of the zoomed image size R' directly from similar triangles in the drawing[1]:

$$R' = -\frac{F_R}{L} R \cdot \frac{l}{L - l - F_R}, \tag{57}$$

where the minus sign accounts for the reversed image orientation. Thus the relative magnification with the additional lens is

$$M_{\text{rel}} \equiv \frac{R'}{R} = -\frac{F_R l}{L(L - l - F_R)}. \tag{58}$$

Although (58) was obtained from consideration of one particular case, it remains valid even when no intermediate image is formed (that is, even when F_R is negative

[1]The treatment given here implicitly assumes that the magnification constant in (47) for the accelerator does not change when its focal length is varied, and that the virtual source formed by the accelerator is not displaced from the actual source (that is, the dotted continuations of the trajectories in the figure indeed come to the original positions of the particles). While these assumptions are not true in general (for example, if the straight parts of trajectories in figure 7 were continued to the left, the crossings would occur at $z < 0$ instead of $z_0 = 0$), they give sufficiently good approximations for the qualitative description, especially in the cases important for the present work.

or exceeds L), which can be checked by simple but somewhat lengthy manipulations with ray optics equations. One of these equations,

$$\frac{1}{f_l} = \frac{1}{l} + \frac{1}{L - l - F_R}, \tag{59}$$

gives the the general expression for the required focal length

$$f_l = l\left(1 - \frac{l}{L - F_R}\right) \tag{60}$$

of the additional lens.

Now the parameters for the additional lens, namely at what distance l from the detector it should be placed and what focal length f_l it should have, required to achieve a relative magnification $M_{\text{rel}} < 1$ can be studied. Since it was decided to keep the total system length L fixed, both M_{rel} and f_l depend on two free parameters: the accelerator focal length F_R and the lens position l. These relationships are illustrated in figure 12 as dependences on l for a few F_R values and on the optical power $1/F_R$ for a few l values (both l and $1/F_R$, as well as f_l, are given in relation to L, since this produces more convenient dimensionless plots). Reiterating the point that significant geometrical changes in a high-vacuum system should be avoided, the principal question in the analysis of (58) is the choice of the optimal single position l that would allow the largest range of magnification variations achievable by adjusting F_R in a reasonable range. According to figure 8 and the related discussion, F_R can be varied from the original value L in (54) to infinity and further to negative values $\sim(-L)$ by relatively small variations of the electric field strengths ratio E_1/E_0. Values $|F_R| < L$ are also possible, but require larger changes in the accelerator parameters and lead to stronger aberrations (see p. 39). In other words, the optical power $1/F_R$ can be varied in a finite range $|1/F_R| \lesssim 1/L$ without adverse effects, which explains why L/F_R was chosen instead of F_R for the plots in figure 12 (additionally, $1/F_R$ is a continuous function of E_1/E_0 and goes smoothly through zero where F_R has an infinite discontinuity between the negative and positive branches).

The first remarkable property of (58) is that for $0 < F_R < L$ (corresponding to the situation depicted in figure 11 and illustrated in figure 12 by the $F_R = 0.5L$ curves) the relative magnification is always negative and can be varied in the whole range from -0 (at $l \to 0$) to $-\infty$ (at $l \to F_R$, or $F_R \to l$ if l is fixed). This would be the general

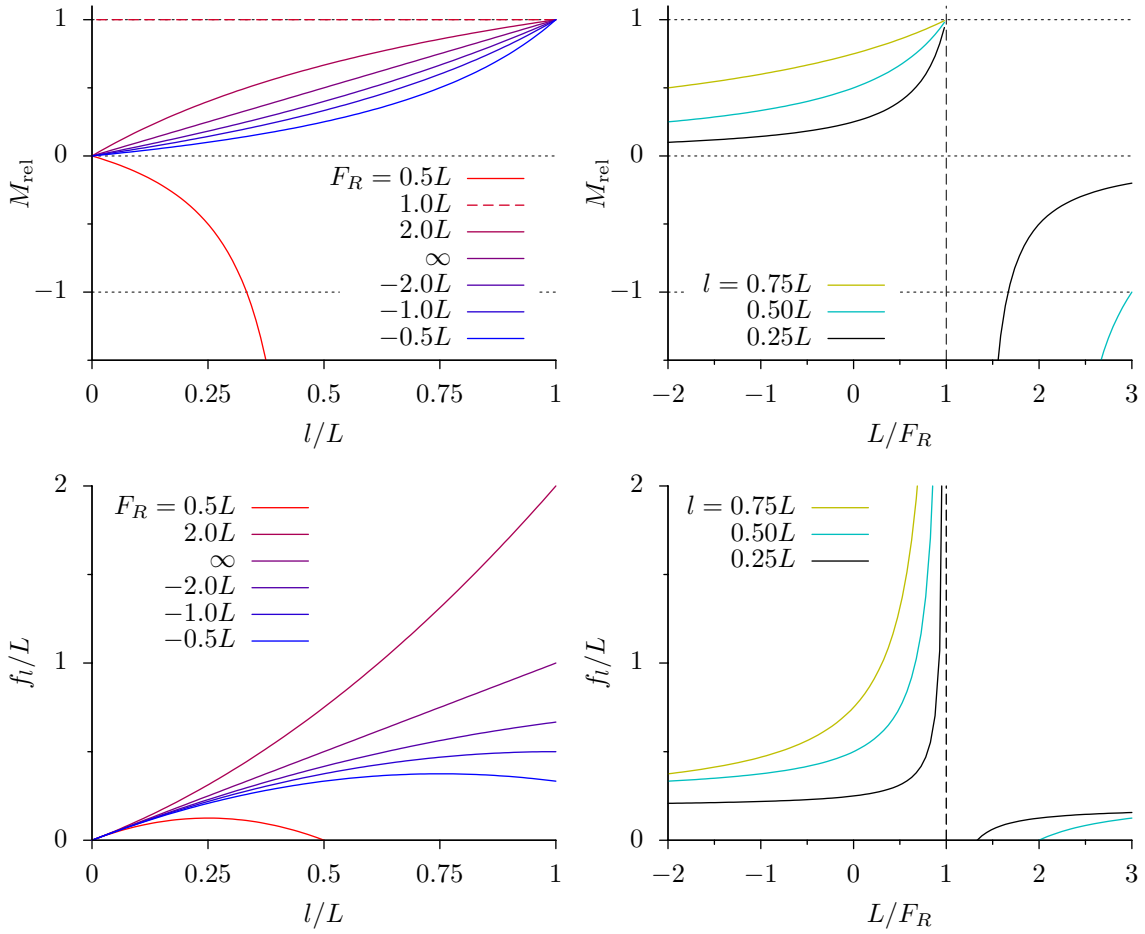

Figure 12 Relative magnification with additional lens and required focal lengths.

solution for the independent magnification control, but unfortunately it requires the shortest focal lengths F_R and f_l compared to all other cases, which means that this solution leads to the strongest aberrations and in practice has strong limitations, since the focal lengths cannot be made very short. Before discussing the other solutions, it should be mentioned that this case with intermediate focusing is the only one allowing an *increase* of the magnification and was successfully used for that purpose in experiments with low $K_0/(qV_0)$ ratios (either due to low produced K_0 or high required V_0), examples of which can be found in [22, 27, 28]. The need for increased magnification means that the original beam size was quite small, and therefore the mentioned problems with aberrations and relatively short focal lengths were not se-

vere in these systems.[1]

The two remaining cases, $F_R < 0$ and $F_R > L$, correspond to optical powers $1/F_R < 1/L$ and can be considered together. They have the property that the relative magnification always remains positive and can be varied from unity, when the additional lens is inactive ($f_l = \infty$), and all focusing is due to the accelerator ($F_R = L$), towards zero, when the accelerator produces a strongly diverging beam ($F_R \to -0$), and the image is produced by the additional lens with a finite focal length ($f_l \to l[1 - l/L]$). This lower limit is, of course, not reachable in practice, but even for a relatively mild variation of the accelerator optical power

$$-\frac{1}{L} \leqslant \frac{1}{F_R} \leqslant \frac{1}{L} \tag{61}$$

the relative magnification range is

$$\frac{l}{2L - l} \leqslant M_{\text{rel}} \leqslant 1 \tag{62}$$

with the required additional lens focal length range

$$l\left(1 - \frac{l}{2L}\right) \leqslant f_l \leqslant +\infty. \tag{63}$$

According to (62), the magnification range is broader when l is smaller, that is, the additional lens is placed *closer to the detector*. However, according to (63), in that case the required $\min f_l \approx l$ also becomes shorter, which places a practical limit on the range. Nevertheless, even for $l = 0.25L$ (see figure 12) a substantial magnification range of $1:7$ could be reached, with a seemingly reasonable minimal $f_l \approx 0.22L$.

The word "seemingly" in the last phrase refers to the fact that although $f_l \approx 0.22L$ is not too small compared to L and is large compared to the detector diameter (40 mm), which was used in subsection 4.3 for justification of the accelerator aperture diameters, the beam diameter (for the detectable particles) at the additional lens is actually $\frac{1}{M_{\text{rel}}}\frac{L-l}{L}$ times larger than the detector diameter. For $M_{\text{rel}} = 1/7$ and $L = 600$ mm this means 210 mm beam diameter for the lens with ~132 mm focal length. That is, the additional lens must have an overall size comparable to the total length of

[1]The small beam diameter allows to make the aperture diameters large compared to it (thus maintaining low filling factors) but at the same time small compared to the required focal lengths (thus keeping the lenses not very strong).

the SVMI system and will have very large geometrical aberrations. In other words, the practical magnification range expected for a system with such detector size is more modest.

At the same time, the radial magnification by itself is not the most important performance characteristic of an SVMI system, since fitting a higher velocity (or kinetic energy) range into the detector radius means that the total TOF spread of the detectable particles also increases according to (35), and hence the slice made by a fixed-duration detection pulse becomes relatively thinner. In order to keep the relative slicing thickness at the desired level[1] the overall electric field strength can be increased, which in turn leads to even higher kinetic energy range fitting into the detector radius (see (15)). This interdependence can be quantified using scaling relationships (35) and (48) and demanding that the TOF stretching and the overall image radius remain unchanged when M_{rel} is applied:

$$\begin{cases} \dfrac{\sqrt{K_0'}}{E'} = \dfrac{\sqrt{K_0}}{E}, \\ M_{\mathrm{rel}}\sqrt{\dfrac{K_0'}{E'}} = \sqrt{\dfrac{K_0}{E}}, \end{cases} \tag{64}$$

where K_0' and E' correspond to SVMI with the additional lens, and K_0 and E — without it. Simple algebraic transformations lead to

$$\frac{K_0'}{K_0} = \frac{1}{M_{\mathrm{rel}}^4}, \tag{65}$$

$$\frac{E'}{E} = \sqrt{\frac{K_0'}{K_0}}. \tag{66}$$

The fourth power in (65) shows that the possible KER range variation is actually significantly larger than the range of radial magnifications created by the additional lens. For example, even a lens with $M_{\mathrm{rel}} = 1/2$ added to the SVMI system studied in subsection 4.3 should allow slicing for distributions with $\max K_0$ from 0.2 eV to 3.2 eV, thus satisfying the main goal for the designed system (see p. 11). Moreover,

[1] Too thin slices do not lead to an improvement of the overall resolution, since other limiting factors (aberrations) start to prevail over the finite-slice blurring (7), but do proportionally decrease the signal level according to (5). Therefore, the optimal relative slice thickness must have some finite value.

only a fourfold variation of the electric field strength from $E_0 = 20$ V/cm (and $V_0 \sim 300$ V) to $E_0 = 80$ V/cm (and $V_0 \sim 1200$ V) would be required.

At $M_{\rm rel} \sim 1/2$ the maximum beam diameter at the lens should not exceed ~80 mm, which is quite reasonable for the considered system dimensions. Nevertheless, since the aperture diameter must exceed the maximum beam diameter (and, if possible, be a few times larger, to avoid excessive aberrations), and the overall diameter (with the brim) of an aperture lens must be additionally at least 3–5 times larger than the opening itself (to reduce the outer fringe effects), the required aperture lens would still remain rather bulky. Recalling that the designed ion-optical system was intended for retrofitting of an existing setup (see the beginning of section 2), which has the vacuum chamber diameter of only ~150 mm, the task appears challenging, if not impossible.

Fortunately, apertures are not the only means of creating inhomogeneous electric fields suitable for charged-particle beam lenses. The other simple type of lenses, called "cylindrical lenses", is created by electrodes assuming a shape of cylindrical surfaces with generatrices parallel to the optical axis (instead of planes perpendicular to it).[1] In contrast to aperture lenses, which separate two regions of different electric fields, cylindrical lenses separate two field-free regions with different electrostatic potentials, as illustrated in figure 13. The electric field formed between the

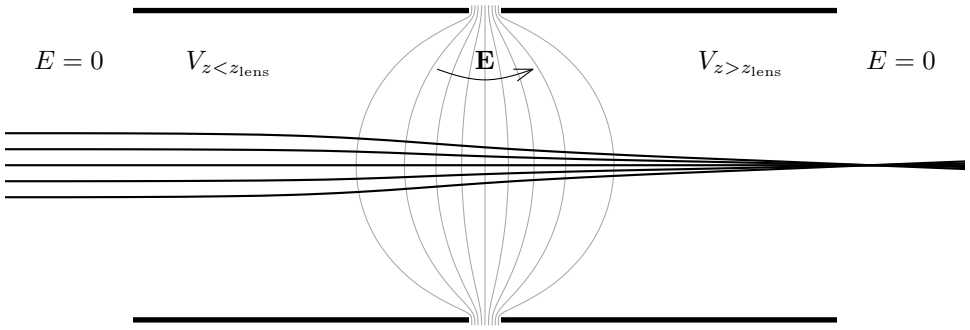

Figure 13 Cross-section of cylindrical electrostatic lens with equipotential contours shown by gray curves and particle trajectories by black ones.

electrodes must satisfy the same equation (50), and thus the arguments about its paraxial properties remain the same. The most useful feature of cylindrical lenses

[1] Although the term "cylindrical lenses" is also used in regular (photon) optics and is similarly due to the use of cylindrical surfaces, the optical lenses have the cylinder generatrices perpendicular to the optical axis and thus perform only 1-dimensional focusing. However, the electrostatic cylindrical lenses are symmetric around the optical axis and focus equally in 2 dimensions.

in the context of this subsection is that if the gap between the electrodes is much smaller that the cylinder radius, then the penetration of external fields inside the lens is negligible. Therefore, the overall diameter of the lens might be only slightly larger than its opening diameter. In other words, a cylindrical lens that fits into a $\varnothing$150 mm chamber might be expected to work with $\varnothing$80 mm beams without enormous aberrations.

Unlike aperture lenses, cylindrical lenses are optically thick, meaning that their front and rear principal planes and focal lengths do not coincide. No simple expressions for the focal lengths exist, but in the case of small gap and weak focusing both focal lengths behave as

$$f \sim \frac{K(K - q[V_{z>z_{\text{lens}}} - V_{z<z_{\text{lens}}}])}{(q[V_{z>z_{\text{lens}}} - V_{z<z_{\text{lens}}}])^2} D, \tag{67}$$

where D is the cylinder diameter, and the proportionality factor is about 5 (see [29] for the expansions with more terms and actual numerical coefficients). As can be seen from (67) (and remains true in the general case), the lens is always converging regardless of the applied potentials, as long as the particles have enough kinetic energy to pass through it. This allows a very useful combination of two sequential two-electrode lenses, which can be considered as a single three-electrode lens, with equal entrance and exit potentials and a different potential applied to the central electrode. Such lenses provide beam focusing without overall altering of the particle energies and are sometimes called "einzel" lenses.[1] They can be used in both modes — with the central potential either lower or higher that the outer potential. The particles are then temporarily accelerated or decelerated (depending on their electric charge) upon entering the lens. The intermediate acceleration mode is usually preferred, since it leads to lower chromatic and geometrical aberrations than the intermediate deceleration mode.

In practical applications the length of the central cylinder is usually made equal to its diameter D, and the gaps $\sim D/10$ between the cylinders are used. The outer

[1]The word "einzel" is a rather illiterate English adoption from the German term "die Einzellinse" meaning "the single lens" (the noun prefix "Einzel-" corresponds to the adjective "einzeln" — single, solitary, individual, discrete, separate and so on), which referred to the fact that this lens is self-contained, and its addition to a system does not change the electric fields and potentials outside the lens. A more meaningful English term used for these lenses is "unipotential", alluding to only one adjustable potential (of the central electrode).

electrodes of lengths D are also sufficient to contain the electric field inside the lens, so that the lens properties do not depend on its surroundings. Therefore, the overall length of the additional cylindrical lens can be slightly smaller than 3 vacuum chamber diameters (that is, ~400 mm), occupying almost the whole "drift" region of the designed SVMI system but fitting into it without obstacles.

The above discussion mentioned explicitly that the radial focusing focal length of the accelerator must be changed when the magnification control with the additional lens is utilized. However, since the particles are temporarily accelerated inside the additional lens, their total TOF is also affected, and the TOF focusing conditions for the accelerator must change accordingly as well. Therefore, the last two equations of (54) have to be replaced with expressions depending on the parameters of the additional lens. The new equations for the actual system are formulated and solved in the next section, but it is appropriate to make here a general remark about their properties. According to the discussion on p. 43, the required F_R variation is relatively small. The central length of the additional lens, where the particles fly faster than they would without the lens, is also relatively small compared to the total length of the system, and thus the required F_t correction should be relatively small as well. As can be seen from figures 6 and 8, relatively small changes in the accelerator parameters should be sufficient to accommodate these variations. Therefore, although the solution for a system with the additional lens must be different from what is shown in figure 9, these differences are not outstanding.

And a final remark before going to the description of the actual setup. Even though the idea of using a separate lens for independent magnification control is not completely new (see p. 42), all applications reported in the literature have been designed only for the 2-dimensional VMI without time resolution. Additionally, in only one case [30] the problem was in reducing the magnification for distributions with high kinetic energies, as in the present work. The optical scheme chosen there was very similar to the one described in this section,[1] however, the authors did not provide its justification (literally: "we had no prior knowledge of the optimal configuration") and obtained the final geometry solely by numerical optimizations. Some

[1]This is not surprising, since similar problems often lead to similar solutions. (In reality, the development was largely independent: although [30] was published before the present work began, it was devoted to a rather different task, and I discovered it only after the general ideas discussed above were already formulated.)

attempts of magnification control in SVMI were made in [11], but since the authors tried to achieve it by adding more lenses to the accelerator (contrary to what is said on p. 43), the resulting range was not much larger than the range shown in figure 10, despite the fact that no attention was paid to TOF focusing and aberrations (that is, the free parameter space was significantly larger).

5 Simulations and final design

The actual design is heavily based on the ideas and results discussed in the previous section. It was deliberately kept as simple as possible because of two factors. First, I had no previous experience in design or construction of ion optics. Second, the used numerical simulations do not predict the behavior of a real system exactly. Therefore, it was desirable to start with a minimal system, which could be built and experimentally characterized without additional complications. It should serve as a proof of concept and a test case for future developments, but at the same time must be usable as an instrument. Thus this section is focused on the issues that were absolutely necessary or at least very useful for the SVMI operation according to the goals stated in section 2. Some possible future improvements of the present system are discussed in section 9.

Although SIMION can perform all calculations in a truly 3-dimensional geometry, the required amount of computational resources is much larger than in the case of cylindrically-symmetric configuration of the electrodes. Taking into account that the real setup was designed to have deviations from cylindrical symmetry only in the outer (in the radial direction) parts, and these deviations are relatively small, the electric field in the important regions should be very well described by the solution obtained for the cylindrically symmetric configuration from which all nonsymmetric features were removed. Therefore, in all simulations reported below the relatively small dielectric holders and connecting wires were removed completely.[1] Nonsymmetric parts of metallic holders were also removed, but the large cylindrical parts were left intact.

[1] In any case, the calculations with dielectrics became available in SIMION only since version 8.1, which appeared after the present system was already built.

5.1 Accelerator

The minimal accelerator design requires two electric field regions, as discussed in section 4. That is, it should include one flat, terminating, electrode with a small opening for entrance of the molecular beam and two flat electrodes with larger apertures serving as electrostatic lenses.

The preliminary results (see figure 9) indicate that the required separations L_0 and L_1 between the electrodes should be ~50 mm each. It means that the overall diameter of the electrodes must be of the order of 240 mm (⌀40 mm aperture, and at least 2×50 mm brim width required to avoid field distortions due to fringe effects[1] and asymmetric environment), which creates the first design problem, since the internal vacuum chamber diameter is only ~150 mm, as mentioned earlier.[2]

The second problem arises from the fact that, according to the actual simulations (see subsection 5.5 below), the optimal values for both L_0 and L_1 depend on the magnification level. In other words, operation at different magnifications requires variation of the distances between the electrodes. Although the variation should be relatively small (from 30 to 80 mm), a precise mechanical movement of relatively thin plates inside a confined high-vacuum chamber and with high voltages applied is not a simple task.

Both of these problems can be solved simultaneously by a simple modification of the electrode configuration. Namely, the fringe effects can be reduced not only by making the brims wider than the gaps, but also by making the electrode-free gaps smaller. Insertion of intermediate electrodes with applied potentials equal to the potentials that should have existed in the original field configuration does not change the field inside the apertures, but allows to make the brims much narrower. For example, electrodes with 10 mm spacing do not require brims wider than 20 mm and thus can have the overall diameter of 80 mm, which should fit well with all additional holders into the given chamber. This configuration is shown in figure 14.[3] Since the original fields E_i $(i = 0, 1)$ between the corresponding adjacent electrodes

[1] No outer fringe effects are visible in figure 7 because the electrodes of the shown system actually extend vertically far beyond the depicted portion.

[2] And the aperture lenses cannot be replaced by cylindrical lenses, as discussed in subsection 4.4, because the ionization region must have a nonzero and relatively homogeneous electric field.

[3] Please not that from this point onwards V_0 refers to the potential of the accelerator terminating electrode, instead of the potential at the initial position of the particles, as it was in the previous sections.

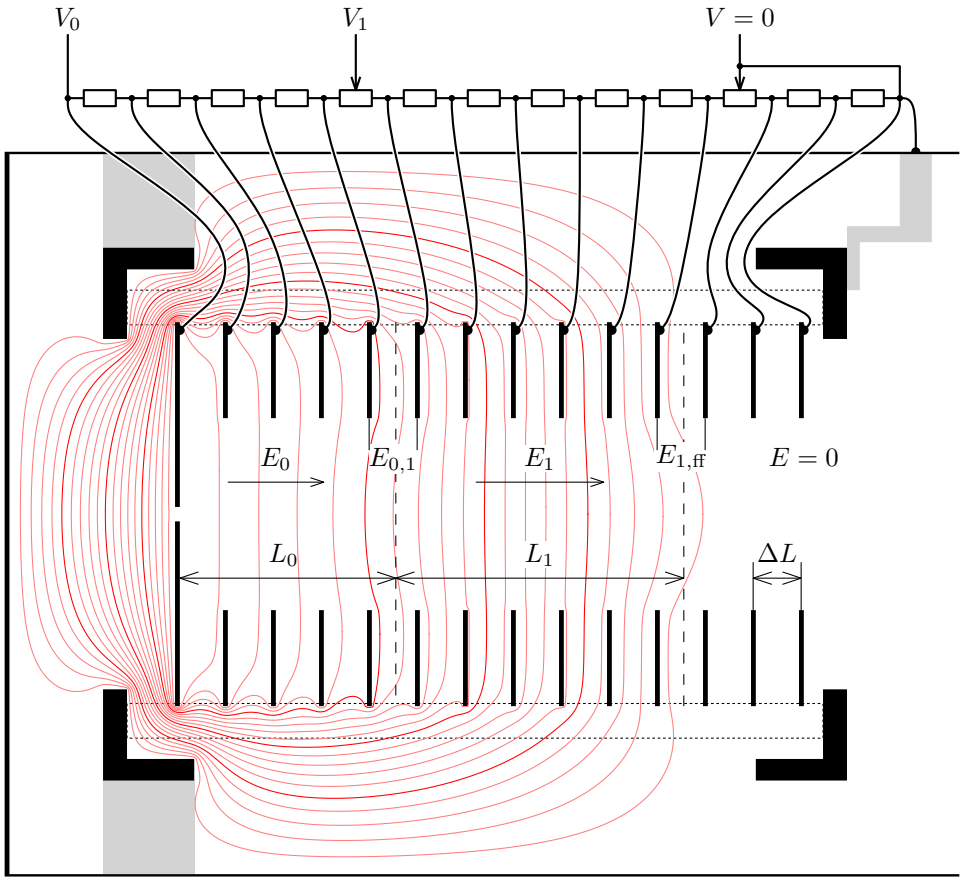

Figure 14 Cross-section of accelerator. Electrodes and metallic holders are shown in black, nonsymmetric parts are schematically given in gray (insulators — by dotted lines). Red lines show an example of equipotential contours. The top part includes an electric circuit diagram of the resistive voltage divider.

were homogeneous, the original potential was a linear function of the z coordinate within each gap. Therefore, the original potential differences must be split among the intermediate electrodes proportionally to the spacings. For equally spaced electrodes this splitting is trivially achieved by a resistive divider with identical resistors, as shown in the figure.

In principle, if the intermediate apertures have the same diameter as the lens apertures, then the resulting electric field should be slightly different from the original one,[1] but this difference is rather small, at least in the most important region near the axis, and does not significantly affect the focusing properties of the lenses.

[1] As can be seen from figure 7, the equipotential contours between the electrodes do not become straight immediately at $r = r_{\mathrm{aperture}}$.

At the same time, if all electrodes have the same shape, than the lengths L_i can be chosen arbitrarily by purely electrical commutation of the applied potentials, without any mechanical movements inside the vacuum system. It is obvious that any distance divisible by the interelectrode step $\Delta L = 10$ mm can be created by this approach. However, if ΔL is small compared to L_i, then arbitrary *effective* distances, not limited to multiples of ΔL, can be created by applying potentials such that the electric field strengths in the "intermediate" regions (see figure 14) are

$$\begin{aligned} E_{0,1} &= \{L_0/\Delta L\}E_0 + (1 - \{L_0/\Delta L\})E_1, \\ E_{1,\mathrm{ff}} &= \{(L_0 + L_1)/\Delta L\}E_1, \end{aligned} \tag{68}$$

where $\{\cdot\}$ denotes the fractional part of the number ($0 \leqslant \{\cdot\} < 1$), $E_{0,1}$ corresponds to the transition between E_0 and E_1, and $E_{1,\mathrm{ff}}$ — between E_1 and the field-free region. The values given by (68) are equal to the average field strengths in the respective regions calculated for the field configuration with real electrodes present at the positions corresponding to the actual "aliquant" L_0 and L_1. The required potentials at all electrodes can be generated by the same resistive network, but with the "intermediate" resistors replaced by potentiometers of equal total resistance, as shown in figure 14. Numerical simulations show that this approach indeed allows continuous variation of both accelerator lengths, and the resulting performance characteristic have smooth dependences on the effective lengths, as illustrated by an example shown in figure 15.[1]

For the final design the "round" step $\Delta L = 10$ mm was chosen, so that the lengths L_i expressed in centimeters correspond to the numbers of interelectrode gaps, making the electric commutation more convenient for the user. All electrode plates were made 1 mm thick and with 80 mm external diameter (see above) for 40 mm internal diameter of the apertures (see p. 38). The small ($\varnothing 3$ mm) orifice in the terminating plate was used in the simulations, but its presence apparently does not affect the electric field at the ionization region that was placed at 15 mm from the terminating electrode[2], in the middle between the first two apertures. According to figure 9, an

[1] The absolute values of ΔK and Δt from the plots shown in figure 10 should not be compared to the data presented here and below because the preliminary simulations described in section 4 were performed with a smaller initial volume and thus showed smaller blurring.

[2] It was important to keep this distance small in order to make the accelerator more compact, but the field at 5 mm (between the terminating plate and the first aperture) might be noticeably distorted by the $\varnothing 3$ mm orifice. At the same time, according to figure 10, the distance $L_0 - L_0' = 15$ mm is already

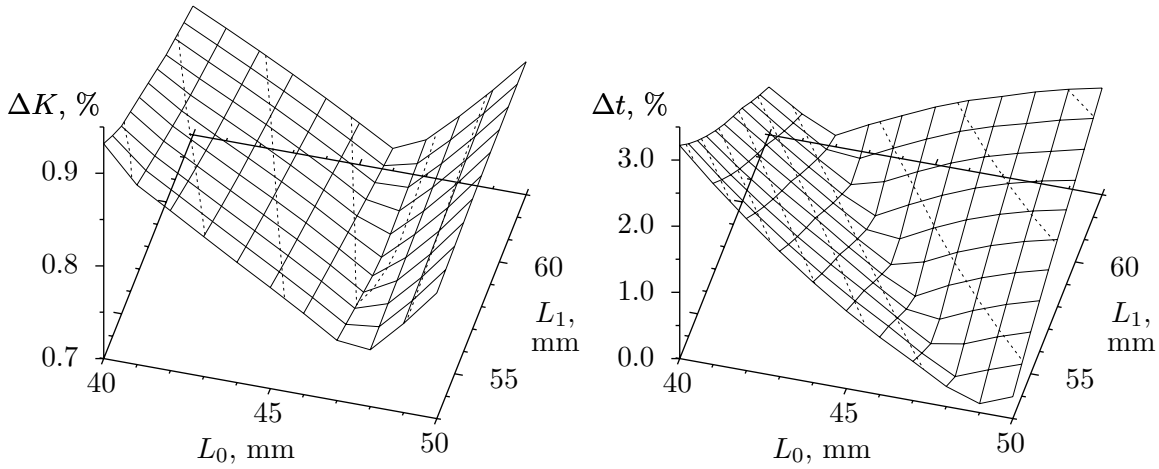

Figure 15 Example of smooth variation of KE and TOF resolutions for effective accelerator lengths changing in 1 mm steps.

overall length $L_0 + L_1 = 110$ mm would be sufficient for operation without the additional lens, but for greater flexibility the length 130 mm was chosen, resulting in 14 electrode plates total. This number might appear excessive (especially for a configuration with only two field regions), but, for example, the system described in [10] used 29 plates for the same purpose. The only significant difference is that the design in [10] was not intended for lengths variations, and thus all voltage-dividing resistors could be placed inside the vacuum chamber, requiring only two high-voltage electrical feedthroughs for the input voltages,[1] whereas the present system requires a facile commutation of the plates and thus demands either a remote-controlled commutator inside the chamber or an external commutator with separate electrical connections to each plate. The latter approach was chosen as more practical for the given number of plates (see subsection 6.1 for details).

5.2 Lens

The most "usual" configuration was chosen for the additional lens of unipotential type: all three cylindrical electrodes have equal diameters, all lengths equal to the diameter, and both gap widths equal to 1/10 of the diameter, as show in figure 16. The outer electrodes are kept at the vacuum chamber potential (that is, grounded), and

sufficient to suppress the effect of the terminating plate on the system characteristics.

[1] Maybe even one input voltage was divided — it is not clear from the published description.

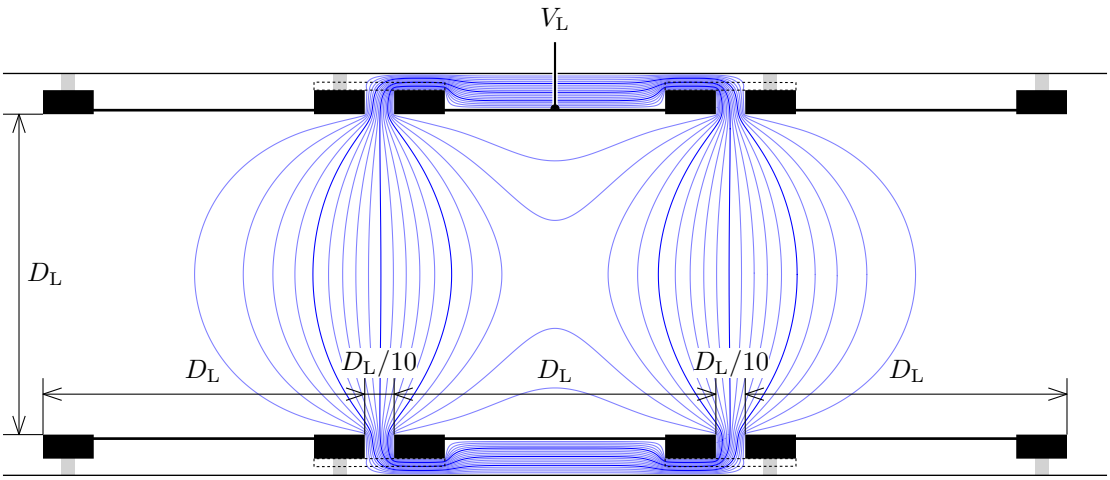

Figure 16 Cross-section of additional lens. Blue lines show an example of equipotential contours for intermediate acceleration mode.

the optical power of the lens is controlled by the potential V_L applied to the central electrode. Since the electric field configuration inside the lens is defined mostly by the edges of the electrodes, the middle part of each electrode was made out of less rigid but much lighter sheet metal inserted into strong and well-shaped holders that form the electrode edges. To be on the safe side, this construction was preserved in the simulations (see the figure).

Since the maximum voltage applied to the lens can be estimated at a few kilovolts, the gap between the outer surface of the electrode and the grounded vacuum chamber wall must be at least a few millimeters for stable and safe operation. The electrode "wall thickness" must be also of the order of a few millimeters in order to have sufficient stiffness for maintaining the geometry of the lens. These factors determine the maximum internal diameter of the electrodes. For the present system with internal vacuum chamber diameter ~150 mm the value of $D_\mathrm{L} = 120$ mm, close to the practical limit, was chosen. This led to the total length of the lens equal to 384 mm. The lens was placed at the detector end of the chamber, in accordance with the conclusion made on p. 43, leaving a small gap (20 mm) between the last electrode edge and the detector flange for better vacuum pumping of the space between the electrode and the chamber wall.

5.3 Focusing criteria

Before proceeding to the actual simulations, it is important to define explicitly and formalize the characteristics that should be optimized. Some of these quantities, such as the central TOF and the maximum radius for a given kinetic energy, have relatively obvious definitions, and their values do not depend significantly on the particular method of estimation, as long as the ion-optical system accomplishes TOF and radial focusing. At the same time, the criteria determining whether the focusing is accomplished and how good it is are less obvious. The finite longitudinal size of the ionization region[1] and the existence of aberrations, which essentially *are* the causes of imperfect focusing, mean that at any given ion optics parameters the focusing for different parts of the initial momentum and position distribution is different. Thus the answer to the question, how good is the focusing, should depend substantially not only on the definition of "focusing", but also on the distribution being mapped.

As it was already mentioned on p. 36, the most reasonable requirement from the SVMI system is to work well for all possible distributions, since the system must have sufficient versatility in order to be usable in many experiments, even not yet planned. Therefore, the main goal chosen for the simulations in this section was optimization of *the worst case*, which means that the performance for *all* particular cases is guaranteed[2] to reach at least these "general" results, but might be somewhat better in favorable situations.

The initial distribution has two independent factors: position distribution and velocity distribution. The uncertainty in the initial position, as mentioned on p. 12, is determined by the size of the ionization region and by the uncertainty in its position relative to the ion optics. In order to perform the worst-case optimization, the maximum possible uncertainty must be assumed in the calculations. As can be seen from figure 17, the Δx uncertainty comes from the molecular beam diameter.[3] An effective

[1] Since the ionization region is located in a nonzero axial electric field, different initial positions of particles with equal initial velocities nevertheless lead to different kinetic energies of such particles in the system.

[2] Of course, "guaranteed" only to the extent of the simulation accuracy. However, optimization for particular cases has exactly the same problems with reliability of the simulations. Since the systematic errors are expected to be relatively small and similar for all interesting particular cases, the optimization of the worst case is still a sensible approach.

[3] Even for a focused laser beam its depth of focus is not short enough to be a limiting factor. Also, for one-photon processes the focusing has no effect on Δx, since the number of photoreaction events is determined by the integral flux, which remains constant along the beam.

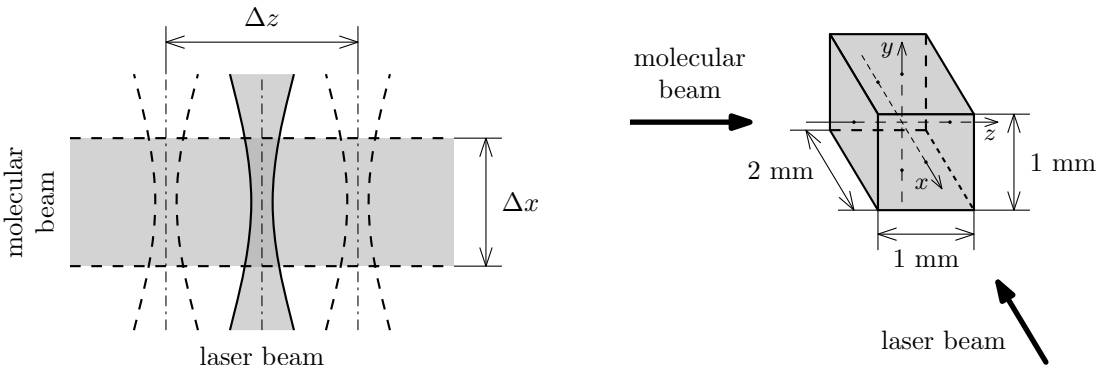

Figure 17 Diagram illustrating initial position uncertainties and the initial volume used in focusing calculations (coordinate system corresponds to figure 1).

value $\Delta x = 2$ mm was used for it in the present calculations.

The uncertainties Δy and Δz come from the laser beam diameter and the uncertainty in the beam alignment relative to the system. The laser beam diameter (for focused beams) is actually much smaller than the alignment uncertainty, and thus the values of Δy and Δz in each particular experiment practically do not exceed a small fraction of a millimeter. However, the alignment relative to the SVMI system and its stability and repeatability between experiments (for example, between the calibration of the mapping and the actual measurements) cannot be guaranteed with such precision. Therefore, the simulations are required to find the conditions that would be robust with respect to these possible variations in the alignment. This approach also guarantees that the possible deviations between the calibration and the measurements performed with different alignments will not exceed the simulated scatter. With this in mind, the values of Δy and Δz were set to the practical laser beam alignment precision estimated at 1 mm, leading to the initial volume depicted in figure 17. The origin of the coordinate system used in the simulations was set to the center of this volume (this obviously does not affect the results, but is a useful convention).

In order to optimize the worst-case resolution, the sample of velocity distribution used for scatter calculations must be representative for all possible cases. Since the mapping is continuous and nearly linear (see (34) and (47)), the sampling does not need to be dense, but it must include the limiting cases, as well as at least a few intermediate points to account for nonlinear distortions.[1] Although there are many

[1]The following discussion is devoted to minimization of the sample size. A larger sample should,

different methods of systematic sampling in spherical coordinates[1], a regular grid was used in this work as the simplest one. It should be noticed that the shape of the trajectories can depend on the relative orientation of the initial velocity and position vectors, but, due to cylindrical symmetry of the electric field, it does not depend on their azimuthal angles (θ in figure 1) with respect to the system. Moreover, test simulations indicated that initial displacements from the z axis in the direction perpendicular to it and to the initial velocity vector (that is, $\delta\mathbf{r} \parallel \mathbf{e}_z \times \mathbf{v}_0$, where $\mathbf{e}_z$ is the axial basis vector) have a very minor effect on the resolution in comparison to all other factors. This means that sampling of velocities in only one plane (xz in this case, since $\Delta x > \Delta y$) is sufficient for estimation of the maximum scatter. Additionally, due to the reflection symmetry of the system (ion optics and initial volume), velocity samples with equal z-components and opposite x-components (that is, (v_x, v_z) and $(-v_x, v_z)$) should yield exactly the same results. Therefore, the variation of v_x can be limited to $v_x \geqslant 0$ without losing generality.

Based on these considerations, the following velocity distribution sample was constructed (see figure 18): 3 different values of kinetic energy $K_0 = K_{\max}$, $0.4K_{\max}$, $0.1K_{\max}$ define the speeds (magnitudes of velocities), spanning the range from the maximum speed to the zero[2] with approximately uniform intervals; for each speed value 5 velocity directions $\alpha = \alpha_0 + n\Delta\alpha$ ($n = 0 \ldots 4$) relative to the z axis are used, starting from $\alpha_0 = 10°$ with $\Delta\alpha = 40°$ steps.[3]

The final representative sample for position and velocity distribution was obtained as direct product of this velocity distribution sample and a representative

obviously, give more reliable and smooth estimations than a smaller sample, but the simulation time depends linearly on the number of particles in the sample. The time is not negligible even for a single run with a few tens of particles and becomes appreciable when multiple runs are performed in an optimization process. Therefore, selection of a small but representative sample is desired for speeding up the optimizations. In principle, more accurate performance estimations for each particular case can be obtained afterwards with a larger and more relevant sample.

[1]The use of spherical coordinates here is dictated only by convenience: they provide separation of the kinetic energy ($K_0 = m|\mathbf{v}_0|^2/2$) from the angular part (direction of $\mathbf{v}_0$). The distribution is not required to be spherically symmetric, but its description in spherical coordinates facilitates the consideration in terms of kinetic energy.

[2]The zero velocity is not included by itself, since it would convey no information on the kinetic energy resolution ($dK_0 = v_0\, dv_0 = 0$ when $v_0 = 0$). At the same time, the family of lowest speed particles (with $K_0 = 0.1K_{\max}$) provides enough information for the lower part of the distribution in the important cases of not very large aberrations and distortions.

[3]These values were selected in order to include $\alpha = 90°$ (which should sample the central slice and reproduce $\max R$ for each K_0) and perform symmetric sampling relative to it. Angles $\alpha = 0°$ and $180°$ were not included for the same reason as $K_0 = 0$ (they produce $R = 0$ for any K_0).

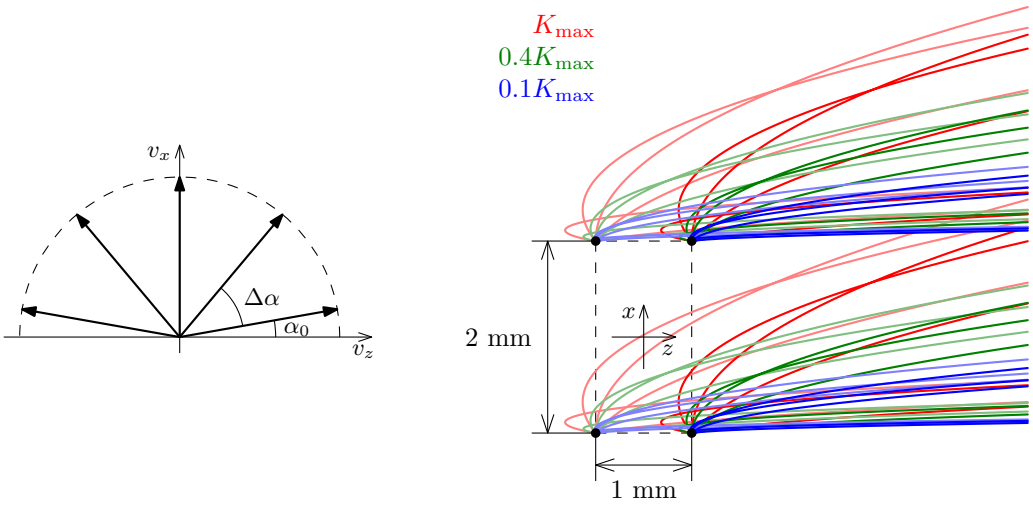

Figure 18 Velocity and position sampling used in focusing calculations.

position sample. As mentioned above (p. 56), displacements along the y axis have minor effect on the resulting arrival positions and times and therefore do not need to be sampled, which means that taking initial positions from the rectangle $\Delta x \times \Delta z$ at $y_0 = 0$ (projection of the initial volume shown in figure 17) is sufficient. Moreover, the test simulations also demonstrated that the geometric shape of a group of particles with a common initial velocity is distorted as they travel through the system[1], but its convexity is approximately preserved. In other words, particles originated from internal points of the initial volume arrive at the detector in between (both in space and time) the "boundary" particles and thus make no contribution to the overall spot size. Therefore, the space distribution sample consisting of only the 4 corner points of the rectangle is representative for the purpose of the worst-case optimization and is also the minimal representative sample. The final sample thus consists of $3 \times 5 \times 4 = 60$ particles. An example of the initial parts of their trajectories in the system is shown in figure 18.

Now, after the initial conditions were defined, the focusing criteria can be discussed. According to the idea of VMI (see p. 5), each group of "equivalent" particles, that is all particles with equal initial velocities, must arrive at the detector at a single point (position of which depends on the initial velocity) regardless of initial positions of the particles within the group. In practice this ideal situation is impossible, and

[1] In the case of ideal focusing the whole initial volume should shrink to a single point when the group reaches the detector position.

each group forms a spot of a finite size instead of a single point. Therefore, it is natural to define the quality of focusing through the spot size — the smaller is the spot, the better is the focusing. For example, for each group (parallel monochromatic ion beam, in terms of ion optics) the focal distance F_R of the optical system is the distance at which the spot reaches its minimum size:

$$F_R(\mathbf{v}_0) \equiv \arg\min_z \left(\Delta r_{\mathbf{v}_0}|_z\right), \tag{69}$$

where

$$\Delta r_{\mathbf{v}_0}|_z \equiv \max_{\delta\mathbf{r}} \left(r(\delta\mathbf{r},\mathbf{v}_0)|_z\right) - \min_{\delta\mathbf{r}} \left(r(\delta\mathbf{r},\mathbf{v}_0)|_z\right) \tag{70}$$

is the scatter of radial distances $r(\delta\mathbf{r},\mathbf{v}_0)$ corresponding to particles with initial positions $\delta\mathbf{r}$ and velocity $\mathbf{v}_0$, measured at distance z.

This focal distance, however, depends on the initial velocity of the particles, as illustrated in figure 19, which constitutes the notion of chromatic aberrations in ion

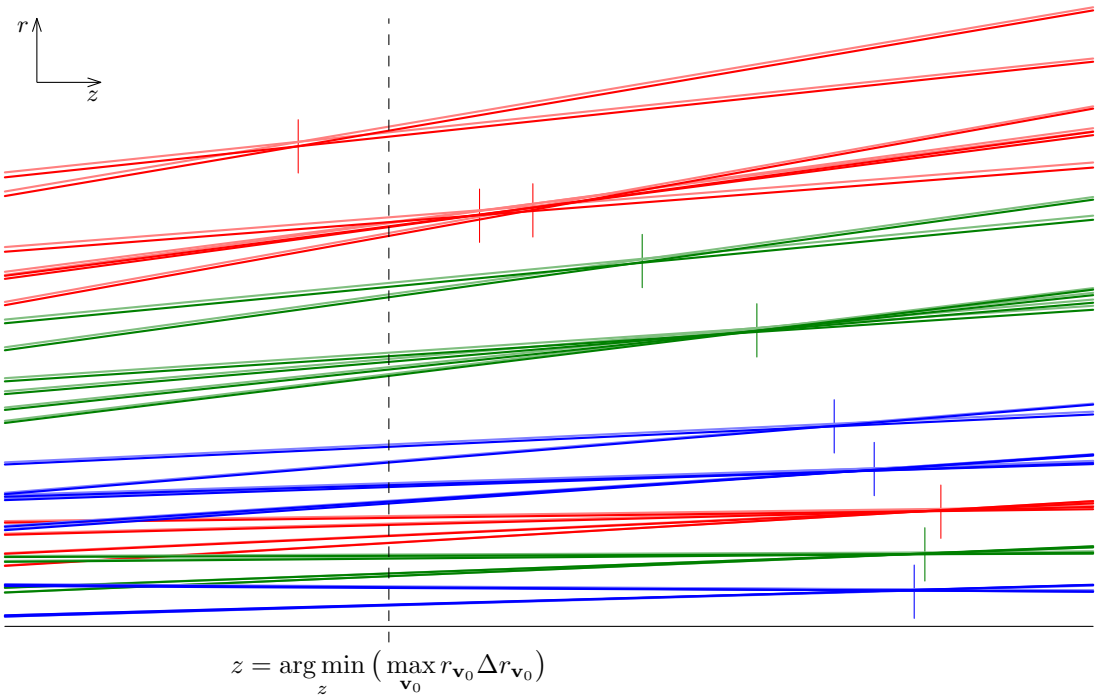

Figure 19 Illustration of focusing with aberrations (vertical scale expanded and aberrations exaggerated for clarity). Positions of minimum blur spots for each initial velocity are indicated by vertical bars.

optics. The worst-case optimization for the whole velocity distribution must therefore

minimize the maximum spot size for all possible initial velocities to find the optimal focal distance:

$$F_{\mathbf{v}} \equiv \arg\min_{z} \left(\max_{\mathbf{v}_0} \Delta r_{\mathbf{v}_0}|_z \right). \tag{71}$$

The subscript $\mathbf{v}$ of $F_{\mathbf{v}}$ signifies that this optimum is for the overall *velocity* resolution. Namely, according to (47), the mapping from the velocity to the radius is nearly linear, thus the scatter in the arrival positions is transferred directly to the scatter of the measured velocities by the inverse, also nearly linear, mapping. If the final goal of the measurements is to obtain the KER distribution, as is usually the case, the optimality criterion must minimize the *kinetic energy* scatter instead of the velocity scatter. The difference between these two approaches comes from nonlinearity of the relationship $K_0 = mv_0^2/2$, which means that $dK_0 = mv_0\,dv_0$, and the relative KE resolution

$$\frac{\Delta K_0}{K_{\max}} = \frac{2v_0\,\Delta v_0}{(v_{\max})^2} \tag{72}$$

is not directly related to the relative velocity resolution $\frac{\Delta v_0}{v_{\max}}$. The focal distance optimal for kinetic energy measurements is therefore

$$F_K \equiv \arg\min_{z} \left(\max_{\mathbf{v}_0} (r_{\mathbf{v}_0} \Delta r_{\mathbf{v}_0}|_z) \right). \tag{73}$$

It is evident that for KE focusing the spot sizes corresponding to faster particles in the distribution are more important than those of slower particles (see also footnote on p. 56). Due to an almost monotonic character of chromatic aberrations (see figure 19) the maxima in (71) and (73) are reached at $v_0 = v_{\max}$,[1] and thus the overall relative KE resolution at $F_{\mathbf{v}}$ is $\max \Delta K_0/K_{\max} \approx 2 \max \Delta v_0/v_{\max}$ — approximately two times worse than the overall relative velocity resolution. However, the test simulations showed that the value of $\max \Delta K_0/K_{\max}$ at F_K is actually comparable to the value of $\max \Delta v_0/v_{\max}$ at $F_{\mathbf{v}}$. That is, even though the difference between the focal distances F_K and $F_{\mathbf{v}}$ in practically important cases is relatively small, the correct choice of the focusing criterion appropriate for a particular type of measurements makes a twofold difference in the resulting resolution.

The focal distance defined by (73) or (71) is useful for general considerations (see, for example, figure 8), but not so convenient for optimization of ion optics parame-

[1] Because of the minimization in these expressions the maxima must also be reached at some lower v_0 values, but this is not important here.

ters: the operation of an SVMI system requires fulfillment of the condition $F_K = L$ (see (54)) in any case, thus instead of adjusting ion optics parameters for simultaneous satisfaction of this equation and optimization of resolution, it is more rational to optimize the resolution by direct minimization of the maximum spot size at the detector. With this approach the overall relative kinetic energy resolution is calculated as

$$\frac{\Delta K}{K_{\max}} \equiv \frac{\max_{\mathbf{v}_i}[\langle R(\mathbf{v}_i)\rangle \Delta R(\mathbf{v}_i)]}{(R_{\max})^2}, \tag{74}$$

where the average arrival position R for particles with initial velocity $\mathbf{v}_i$ is

$$\langle R(\mathbf{v}_i)\rangle \equiv \frac{1}{N_{\text{pos}}} \sum_{\delta\mathbf{r}_j} R(\delta\mathbf{r}_j, \mathbf{v}_i), \tag{75}$$

and the corresponding scatter is

$$\Delta R(\mathbf{v}_i) \equiv \max_{\delta\mathbf{r}_j} R(\delta\mathbf{r}_j, \mathbf{v}_i) - \min_{\delta\mathbf{r}_j} R(\delta\mathbf{r}_j, \mathbf{v}_i). \tag{76}$$

The maxima, minima and sums are taken over the respective velocity or position samples described above (see p. 56 and figure 18; $N_{\text{pos}} = 4$ is the number of initial positions in the sample). The maximum radius $R_{\max} \equiv \max_{\mathbf{v}_i} \langle R(\mathbf{v}_i)\rangle$ corresponds to the maximum kinetic energy $K_{\max}$ and usually should be equal to the detector radius.

The overall TOF characteristics can be defined similarly, but with a small difference stipulated by the fact that the present SVMI system is not intended for recovery of the initial kinetic energies from the TOF data and requires minimization of the TOF scatter only in the direct sense in order to minimize its contribution to the effective slice thickness. Therefore, the following expressions for the overall TOF resolution

$$\Delta t \equiv \max_{\mathbf{v}_i} \Delta t(\mathbf{v}_i), \quad \Delta t(\mathbf{v}_i) \equiv \max_{\delta\mathbf{r}_j} t(\delta\mathbf{r}_j, \mathbf{v}_i) - \min_{\delta\mathbf{r}_j} t(\delta\mathbf{r}_j, \mathbf{v}_i), \tag{77}$$

and the total TOF spread

$$\Delta\tau_{\max} \equiv \frac{\max_{\mathbf{v}_i} \langle t(\mathbf{v}_i)\rangle}{\max_{\mathbf{v}_i} \cos\alpha_i} + \frac{\min_{\mathbf{v}_i} \langle t(\mathbf{v}_i)\rangle}{\min_{\mathbf{v}_i} \cos\alpha_i}, \quad \langle t(\mathbf{v}_i)\rangle \equiv \frac{1}{N_{\text{pos}}} \sum_{\delta\mathbf{r}_j} t(\delta\mathbf{r}_j, \mathbf{v}_i) \tag{78}$$

were used (here $t(\delta\mathbf{r}_j, \mathbf{v}_i)$ denote the arrival times of the corresponding particles). The seemingly complicated form of (78) is caused by the lack of the limiting angles $\alpha = 0°$ and $180°$ in the used sample. Hence the total TOF spread is estimated from

extrapolation of the extremal present angles according to (34) and the relationship $v_z = \cos\alpha \cdot v_0$. (For a sample with the limiting angles the expression for the total TOF spread becomes simply $\Delta\tau_{\max} = \max_{\mathbf{v}_i}\langle t(\mathbf{v}_i)\rangle - \min_{\mathbf{v}_i}\langle t(\mathbf{v}_i)\rangle$.)

Besides the TOF resolution (77), the operation of a system in SVMI mode is also sensitive to TOF distortions produced by the ion optics. These distortions manifest themselves as deviations from the simple mapping $v_z \mapsto t$ described by (34) with the arrival time becoming additionally dependent on the radial component v_r of the initial velocity. While this dependence is relatively small and is not detrimental in case of 3-dimensional detection with time resolution[1], its presence is very undesirable for slicing, since slices taken by selection of arrival times no longer result in images of (v_x, v_y) distributions corresponding to particular v_z values. Therefore, this effect must be taken into account in assessment of the ion-optical system performance. For that purpose one additional characteristic, the TOF distortion of the central slice ($v_z = 0$), was introduced in the simulations. It is defined as

$$\Delta t_0 \equiv \max_{\mathbf{v}_i \perp \mathbf{e}_z} \langle t(\mathbf{v}_i)\rangle - \min_{\mathbf{v}_i \perp \mathbf{e}_z} \langle t(\mathbf{v}_i)\rangle, \tag{79}$$

where the maximum and minimum are taken over the velocities with zero z-component. In the actual simulations, due to the lack of $\mathbf{v}_0 = 0$ in the sample, the following estimation

$$\Delta t_0 = \langle t(v_{\max}, \alpha = 90°)\rangle - \frac{1}{2}\left[\langle t(v_{\min}, \alpha_{\min})\rangle + \langle t(v_{\min}, \alpha_{\max})\rangle\right] \tag{80}$$

was used. It is based on the observations made from the test simulations that: 1) the TOF distortion is monotonic with respect to v_r, 2) particles with higher v_r have longer flight times (due to longer flight paths and shorter intermediate acceleration in the additional lens, which is the main source of the distortion), 3) the average of TOFs of the particles with $v_{\min}$ and extremal angles provides a better TOF estimation for $v_0 = 0$ than the TOF of the particle with $v_{\min}$, $\alpha = 90°$ (the particles with extremal angles have smaller v_r and thus are less affected by TOF distortions).

[1] In that case both radial and TOF distortions can be corrected by postprocessing of the recorded data.

5.4 Simulation details

As mentioned earlier, all numerical simulations were performed using SIMION 8 package. In general terms, the simulation process begins from defining the geometry of all electrodes (that is, all conductive bodies, including the vacuum chamber walls, the detector and so on). This geometry is projected onto a suitable spatial grid, and SIMION numerically solves Laplace's equations on this grid in order to find the dependence of the electrostatic potential in the whole space on the electrode potentials. Due to the linearity of Laplace's equation this procedure requires solution of N_{el} (the number of electrodes) Laplace's equations each of which has boundary conditions with all, except one, electrodes grounded (zero potential). The potential distribution in free space is then obtained for arbitrary combination of electrode potentials as the corresponding linear combination of these particular solutions. The particular solutions are found only once, when the geometry is defined, and stored for further use. This makes any adjustments of electrode potentials during the simulations an easy and fast process. (On the other hand, any modifications of the geometry require complete recomputation of all Laplace's equations and therefore is time-consuming.)

Once the electrostatic potential in free space is available, the particles with defined initial positions and velocities can be propagated according to the equations of motion (9). SIMION uses an adaptive numerical integration method to solve these equations[1] and reports the arrival times and positions for each particle. These data can be saved for further analysis by external means or passed to a user-defined subroutine within the simulation process.

The latter method was chosen in the present work because it allows smoother integration of the preparation of the initial conditions, the simulation itself and the analysis of its results. In particular, all these steps can control each other, providing the possibility of automatic optimization of some characteristics with minimal user's intervention. These capabilities were not only useful during the design process, but are also quite important in the practical use of the system, since, as shown in the next subsection, the system offers a broad range of operation conditions, and the complete summary of optimal parameters and characteristics for each particular case cannot

[1]The electric field at trajectory integration points is found by interpolation of the numerical derivative of the electrostatic potential. The trajectory integration points generally do not coincide with the potential grid points and are usually denser and irregular. Moreover, the equations of motion are always solved in the full 3-dimensional space (in rectangular coordinates), even for potentials defined in restricted geometries (for example, cylindrically symmetric, as in the present case).

be provided here. Therefore, the most practical approach is to use the most important plots (given in the next subsection) for selection of the desired regime of operation and then to find the detailed data for it by simulations and/or optimizations stating from the chosen point.

Listings of all files required for SIMION simulations are given in appendix A. They consist of the geometry definition file, the particles definition file and the user program file.

The geometry definition file (appendix A.1) formalizes the descriptions of the accelerator and the lens given in subsections 5.1 and 5.2. Additionally, it describes the internal shape of the vacuum chamber and the detector, with some simplifications immaterial to the problem. Since the design optimization involved some changes of the geometry, the file was also changing during the development, but the present listing corresponds to the final version, which should be very close to the geometry of the physical implementation.

As mentioned above, cylindrical symmetry was used for the electric potential, and thus the geometry is defined in cylindrical coordinates[1]. A grid step of 0.5 mm was chosen to adequately represent all relevant details (the finest of which is the 1-mm thickness of the accelerator plates). The file defines 17 logical electrodes: 1 grounded and 16 adjustable, out of which 14 are the accelerator plates, 1 is the central element of the lens, and 1 is the front plate of the detector. The reason why the latter is not grounded is explained in subsection 6.2 below.

The particles definition file (appendix A.2) defines the initial states of the particles as described on p. 56 and illustrated in figure 18. In principle, as shown in subsections 3.1 and 3.2, all characteristics of the system in any mode of operation can be extracted, using the corresponding scaling relationships, from simulations based on a sample with fixed kinetic energies and particle mass, if the electric potentials are scaled appropriately. On the other hand, the simulations can be performed with the actual potentials and parameters of the particles. The choice between these two approaches is merely a matter of convenience.

The convenience has two aspects — for the end user and for the implementation

[1]Attention! Cylindrical geometry in SIMION is always defined with the x axis as the cylindrical axis. This does not coincide with the coordinate system used in the present work. Therefore, (x,z) coordinates here correspond to (Y,X) coordinates in SIMION. This should not lead to a confusion in reading, nor in using the provided program, but must be kept in mind if modifications to any of the files are to be made.

of the simulation algorithm. It should be noted that SIMION does not allow dynamic creation of particles for the simulations. That is, all needed particles must be defined beforehand, using only a static description. At the same time, the potentials can be varied freely, as mentioned above, which suggests that the first approach is simpler to implement, even though it is less convenient for the user.[1]

However, *parameters* of each defined particle can be changed during the simulations in the same way as the electrode potentials. It means that if all particles in the desired sample are defined in some "generic" manner, their parameters can be adjusted at the beginning of the simulation according to the actual properties (particle mass and maximum kinetic energy) of the sample, and then the simulations can proceed with the actual values of all parameters, presenting a totally consistent picture to the user. This approach is obviously preferred from the user's perspective, and since it is also not more difficult than the first approach from the programming point of view, it was chosen in this work.

Specifically, $K_{\max} = 1$ eV and $m = 1$ Da were used for the sample described by the particles definition file. The particle initialization subroutine described below scales the particle mass and the resulting velocity[2] for each particle according to the user's input at the beginning of each simulation cycle.

The initial spatial distribution of the particles was defined symmetrically around the origin (as shown in figure 18). It is not modified in the simulations — instead, the potential array that describes the ion-optical system is placed in the workbench in such a way that the origin (and thus the center of the ionization region) falls into the desired position relative to the accelerator. On the one hand, this placement is fully controlled by the standard means from the SIMION interface, on the other hand, the coordinate system in this approach is always associated with the ionization region center, which is a natural reference point.

The user-program file (appendix A.3) contains definitions of all necessary variables and subroutines used for control of the simulations, calculation of performance characteristic from the simulation outcome and optimization of some of these char-

[1] The drawbacks come from the fact that while the user-defined subroutine can present the analyzed characteristics in the appropriately scaled form, it cannot affect other useful information available through the SIMION interface, such as isopotential contours, electric field readings and time markers on the trajectories.

[2] SIMION internally works with velocities only, although the initial conditions can be defined by specifying kinetic energies, which is more convenient for the present problem.

acteristics. Details of working with the program and some SIMION-specific aspects are given in the appendix.

The optimizations are performed with the help of the SIMION built-in implementation of the simplex method (Nelder–Mead algorithm [31]). Although the simplex optimization is extremely universal (it works for all continuous objective functions and even for some discontinuous ones) and robust, this generality comes from the fact that only numerical values of the objective function at several points of the parameter space are used. Hence, even if the objective function has some "good" properties (for example, is smooth or doubly differentiable), that information is not used, and the required number of iterations is generality large compared to more specialized optimization methods. Nevertheless, the practical use of the program showed that this number is not overwhelming (normally $\lesssim$200 optimization steps, resulting in the overall time of a couple minutes), and the simplicity of use and modifications outweighs the imperfect time efficiency.

The present program can optimize the overall kinetic energy resolution ΔK and solve for the maximum measurable kinetic energy $\max K$. The latter is also achieved through minimization, with the objective function $|R_{\max} - R_{\det}|$, where $R_{\det}$ is the detector radius. Since the condition $R_{\max} = R_{\det}$ can always be satisfied by an appropriate value of $K_{\max}$, the objective function

$$\Delta K + \lambda |R_{\max} - R_{\det}| \tag{81}$$

is used for optimization of the overall resolution under the constraint that the image exactly fills the detector.[1] The constant factor λ compensates the difference in dimensions of the two terms and plays an important role in ensuring that the second term indeed imposes a constraint. Namely, both ΔK and $R_{\max}$ depend on all adjustable parameters (see p. 123) and therefore, if λ is sufficiently small, then the decrease in ΔK upon variation of the parameters might overpower the increase in $\lambda|R_{\max} - R_{\det}|$, leading to shifting of the minimum of (81) to a point where $R_{\max} \neq R_{\det}$ (obviously, in the limit $\lambda \to 0$ the optimization becomes unconstrained). On the other hand, the dependences are nonlinear, and thus very large values of λ would cause (81) to form a narrow curved valley, which is known to present difficulties for all numerical opti-

[1] The optimization result in that case obviously includes the maximum detectable kinetic energy $\max K = K_{\max}$ as well.

mization methods. The empirical value $\lambda = 10$ (for ΔK in % and R in mm) was found to be a good choice for all relevant simulations in the present work.

The selection of ΔK as the optimized characteristic is explained by its importance for the SVMI performance. Indeed, with the present ion-optical system the imaged kinetic energy range and the TOF stretching for it can be *set* to the desired values, and the optimization goal is to maximize the resolution for the selected regime. It should be clear from the previous discussion that among the characteristics determining the total resolution of an SVMI system the radial focusing, characterized by ΔK, has the greatest effect. Since simultaneous optimization of all contributions is not possible (see p. 73 for a detailed discussion), this most important one was chosen for the "elementary" optimization by the program.

Only one parameter, V_1, is varied in the present program for the minimization of ΔK. The reasoning behind this choice is simple. The problem has five adjustable ion optics parameters: L_0, L_1, V_0, V_1 and V_L. The lens voltage V_L is associated mostly with the magnification factor and has a relatively small effect on the focusing. The highest voltage applied to the accelerator is equal to V_0 and is a less flexible parameter than V_1 from an experimental point of view. Although the lengths L_0 and L_1 are also adjustable, their variation for optimization of focusing at fixed V_1 is not a good idea — first, the variation of the lengths is much more limited than that of the voltage,[1] second, the precision of adjusting the voltage at fixed chosen lengths is much higher than of adjusting the lengths to some general values. Hence V_1 seems to be the most convenient adjustable parameter for minimization of ΔK, both theoretically and practically.

In principle, variation of V_1 at fixed values of all other ion optics parameters achieves variation of the focusing by changing both E_1 and E_0 electric field strengths and in that way also leads to changes in R_max and $\Delta\tau_\mathrm{max}$ for a given K_max. Therefore, if a ΔK minimization under strictly fixed $\max K$ and $\Delta\tau_\mathrm{max}$ is required, the varied parameters must also include V_0 (for E_0 compensation, to keep $\Delta\tau_\mathrm{max}$ constant) and V_L (to compensate the magnification changes). However, in practice ΔK is a very strong function of V_1, and thus no significant differences in $\max K$ and $\Delta\tau_\mathrm{max}$ upon the ΔK minimization by V_1 adjustment should be expected, unless the starting point for the optimization was chosen very far from the working conditions. That is, for

[1] For example, configurations with $L_i < 0$ or $L_0 + L_1 > 130$ mm are not physically feasible, whereas the voltage can be set to any value.

practical applications, which require only coarse settings of $\max K$ and $\Delta\tau_{\max}$, the difference between the simple approach with only V_1 and the more complicated one with $\{V_0, V_1, V_L\}$ is not important. Nevertheless, if a more constrained optimization is needed, the modification of the objective function (81) and inclusion of additional variables in the parameter space are straightforward.

5.5 Simulation results

The goals of the simulations were the study of the operational limits, determination of the resolution and optimal conditions for each achievable imaged kinetic energy range, and verification of the chosen geometrical parameters.

The exact scaling relationships discussed in subsection 3.1 allow to limit variation of the ion optics parameters to 4 variables: $\{L_0, L_1, V_1/V_0, V_L/V_0\}$. That is, the maximum voltage on the accelerator, V_0, can be used as the overall electric field strength scale, with the shape of the electric field described by the geometrical parameters L_0 and L_1 and the relative potentials V_1/V_0 and V_L/V_0. Then, according to (15), the imaged kinetic energy range should scale proportionally to V_0. The TOF, according to (18), should be proportional to $\sqrt{m/V_0}$, and the maximum TOF stretching, according to (35) and the $\max K \sim V_0$ scaling, should have the same $\sqrt{m/V_0}$ dependence. It means that the "magnification index"[1] introduced here as

$$M \equiv \Delta\tau_{\max}\sqrt{K_{\max}/m} \quad (\text{for } K_{\max} = \max K) \tag{82}$$

does not depend on V_0 and thus can be determined as a function of the 4 free variables mentioned above at any fixed V_0 value.

The magnification index plays the major role in selection of the ion optics parameters for SVMI operation. Namely, it is completely and unambiguously determined by the experimental conditions: the particle mass m, the desired imaged KE range $K_{\max}$ and the TOF stretching $\Delta\tau_{\max}$ required for slicing. Therefore, expressing other performance characteristics and the required ion optics parameters as functions of the magnification index should provide the most convenient representation of the simulation results.

[1] This quantity is not directly related to the relative magnification M_{rel} used in subsection 4.4. The index rather describes the combination of the temporal and radial characteristics and is numerically equal to the total TOF stretching for a distribution of $m = 1$ Da particles with $K_{\max} = 1$ eV under the voltages scaled such that the image fills the whole detector.

The performance characteristics related to resolution also can be expressed in a more universal form than they were defined above. The relative overall kinetic energy resolution ΔK defined by (74) is already a dimensionless quantity independent on the V_0 and m scalings, but the overall TOF resolution Δt defined by (77) and the central slice distortion Δt_0 defined by (79) are absolute quantities (with the dimension of time) and scale with V_0 and m as the TOF itself. However, being divided by $\Delta\tau_{\max}$ they become dimensionless, independent on V_0 and m, and directly representing the quantities important for slicing — the relative time resolution of the axial velocity mapping (34) and the shape distortion in realization of the entire mapping (1).

Therefore, the relationships between the ion optics parameters and the resulting performance characteristics are represented here as follows. The magnification index M is taken as the main independent variable, which determines a subset of the electric field configuration parameters $\{L_0, L_1, V_1/V_0, V_\mathrm{L}/V_0\}$ corresponding to this value of M and with V_1/V_0 satisfying the KE focusing condition (see (81) and the discussion about it). This subset has two free parameters,[1] which were chosen simply as L_0 and L_1, and corresponds to a set of relative resolutions and distortions $\{\Delta K, \Delta t/\Delta\tau_{\max}, \Delta t_0/\Delta\tau_{\max}\}$ obtainable for the given value of M. Selection of the optimal combination from the latter set thus determines the required L_0 and L_1 lengths and, through them, the required voltage ratios. The absolute voltage scale is determined by the desired $K_{\max}$ or $\Delta\tau_{\max}$ in (82). The relationship between $\max K$ and V_0 was chosen for this purpose in the present work, since it allows a more evident representation, and selection of $\max K$ is more relevant from the experimental point of view.[2]

Presentation of characteristics dependent on three parameters (M, L_0 and L_1) is a difficult task, especially if all these parameters can vary continuously and in broad ranges. The decision made in this work was to use graphical representation and to plot the characteristics as functions of the main variable M for a discrete set of L_0 and L_1 values. Namely, a regular grid with 5 mm steps in each variable was used for $\{L_0, L_1\}$ combinations. This produces a reasonable balance between the density

[1] Out of 4 degrees of freedom one (V_1/V_0) is determined by the KE focusing condition, and one more is constrained by M, on which V_L/V_0 has the largest effect.

[2] Namely, $\max K$ must be set according to $K_{\max}$ in the studied distribution, which should be appropriately known from preliminary experiments or theoretical estimations, while $\Delta\tau_{\max}$ must simply have some value determined by the desired slice thickness and not directly dependent on the particular distribution.

of the parameter space sampling and the number of plotted curves. Additionally, the current implementation of the system uses a voltage divider that employs fixed resistors instead of continuously variable potentiometers (see p. 83) and allows lengths selection with exactly these 5 mm steps, thus the plots are directly related to the operation of the actual system.

Since the program used for generation of the simulated characteristics and described in the previous subsection operates in terms of the

$$\{L_0, L_1, V_0, V_\mathrm{L}\} \mapsto \{\max K, \Delta\tau_\mathrm{max}, \Delta K, \Delta t, \Delta t_0; V_1\} \tag{83}$$

transformation instead of the

$$\{M, L_0, L_1\} \mapsto \left\{\Delta K, \frac{\Delta t}{\Delta\tau_\mathrm{max}}, \frac{\Delta t_0}{\Delta\tau_\mathrm{max}}; \frac{V_1}{V_0}, \frac{V_\mathrm{L}}{V_0}, \frac{qV_0}{\max K}\right\} \tag{84}$$

one required for the chosen data representation, the algorithm for constructing the (84) dependences from (83) data was organized in the following way. A fixed value $V_0 = 1000$ V was used in all simulations.[1] For every combination of lengths $\{L_0, L_1\}$ (with L_i divisible by 5 mm, as mentioned above) the lens voltage V_L was sampled from 0 to 2700 V (with variable steps, from 50 to 200 V, adaptively selected for sufficient smoothness of the results), and for each V_L value the optimal values of V_1 and K_max were found, as described on p. 65, together with the corresponding performance characteristics. This resulted in a large set of data in the form (83). Then the values of M were computed from $\max K$ and $\Delta\tau_\mathrm{max}$ for each sampled combination of the ion optics parameters, and the resulting sampling of the mapping $V_\mathrm{L} \mapsto M$ for each $\{L_0, L_1\}$ was inverted to obtain the sampling in the form $M \mapsto V_\mathrm{L}$, as needed for (84). The relative characteristics in the right side of (84) were subsequently calculated from the corresponding absolute values in (83). This resulted in transformation of the initial simulations data set from the form (83) to the desirable form (84), although with nonuniform (and irregular with respect to $\{L_0, L_1\}$) sampling over M. Nevertheless, since all interdependences are continuous and relatively smooth, and the original sampling was sufficiently dense, the results can be resampled to any

[1] This value is arbitrary, but lies roughly in the middle of the actual working V_0 range and thus should be suitable for all simulations (meaning that the simulated condition would not differ drastically from the actually used ones and therefore should not lead to unexpected numerical errors in the simulations).

desired grid using interpolation. In the present work a resampling to a regular grid with 0.1 ns$\sqrt{\text{eV/Da}}$ step in M with linear interpolation was used for plotting and analysis of the data.

The resulting performance characteristics are presented in figure 20, and the corresponding operational parameters — in figures 21 and 22. The quantity "total Δt" plotted in figure 20 is defined as the sum of Δt and Δt_0 and is a more relevant temporal characteristic for SVMI operation than Δt and Δt_0 by themselves. Namely, the quality of slicing performed by time gating of the detector is sensitive to the total deviation of the actual arrival times of particles with $v_z = 0$ from the arrival time expected for perfect velocity mapping. This deviation has contributions from both the imperfect TOF focusing described by Δt and the distortion of the $v_z \mapsto t$ mapping described by Δt_0. The maximum TOF scatter important for the worst-case performance should therefore include both these components and for the whole imaged distribution is equal to the sum of the worst-case estimations of these deviations.[1]

Nevertheless, the dependences for the constituents Δt and Δt_0 are also plotted, since they are determined by different factors and might have different contributions and degrees of importance in particular cases. For example, Δt is due to finite dimensions of the initial volume, and the plotted scatter corresponds to their specific values (see figure 18). If the ionization region or the uncertainty in its location in a particular experiment is smaller, then the TOF scatter Δt would be accordingly smaller and hence having a smaller effect on the total Δt for SVMI. At the same time, the plotted Δt_0 values correspond to the whole velocity distribution from 0 to $v_{\max}$ (or KE from 0 to $K_{\max}$). If the actual imaged distribution has a narrower range of

[1] In principle, the overall TOF scatter described by Δt is calculated for the whole velocity distribution, and thus the scatter for particles with $v_z \approx 0$ — the only important part of the distribution for recording of the central slice — might be smaller. However, for the vast majority of the practically important conditions the velocity-dependent part of the TOF scatter is negligible (as a reminder, the scatter is due to the initial position distribution, assumed to be velocity-independent), and the scatter is nearly symmetric around the average TOF. Thus the overall scatter Δt gives a good estimation of the TOF scatter for *any* initial velocity value, and the "total Δt" for the central slice can be expressed as

$$\begin{aligned}\max_{\delta\mathbf{r},\mathbf{v}\perp\mathbf{e}_z} t(\delta\mathbf{r},\mathbf{v}) - \min_{\delta\mathbf{r},\mathbf{v}\perp\mathbf{e}_z} t(\delta\mathbf{r},\mathbf{v}) = \max_{\mathbf{v}\perp\mathbf{e}_z}\left(\max_{\delta\mathbf{r}} t(\delta\mathbf{r},\mathbf{v})\right) - \min_{\mathbf{v}\perp\mathbf{e}_z}\left(\min_{\delta\mathbf{r}} t(\delta\mathbf{r},\mathbf{v})\right) \approx \\ \approx \max_{\mathbf{v}\perp\mathbf{e}_z}\left(\langle t(\mathbf{v})\rangle + \frac{\Delta t}{2}\right) - \min_{\mathbf{v}\perp\mathbf{e}_z}\left(\langle t(\mathbf{v})\rangle - \frac{\Delta t}{2}\right) = \left(\max_{\mathbf{v}\perp\mathbf{e}_z}\langle t(\mathbf{v})\rangle - \min_{\mathbf{v}\perp\mathbf{e}_z}\langle t(\mathbf{v})\rangle\right) + \Delta t = \\ = \Delta t_0 + \Delta t, \quad (85)\end{aligned}$$

where definitions (77) and (79) were used.

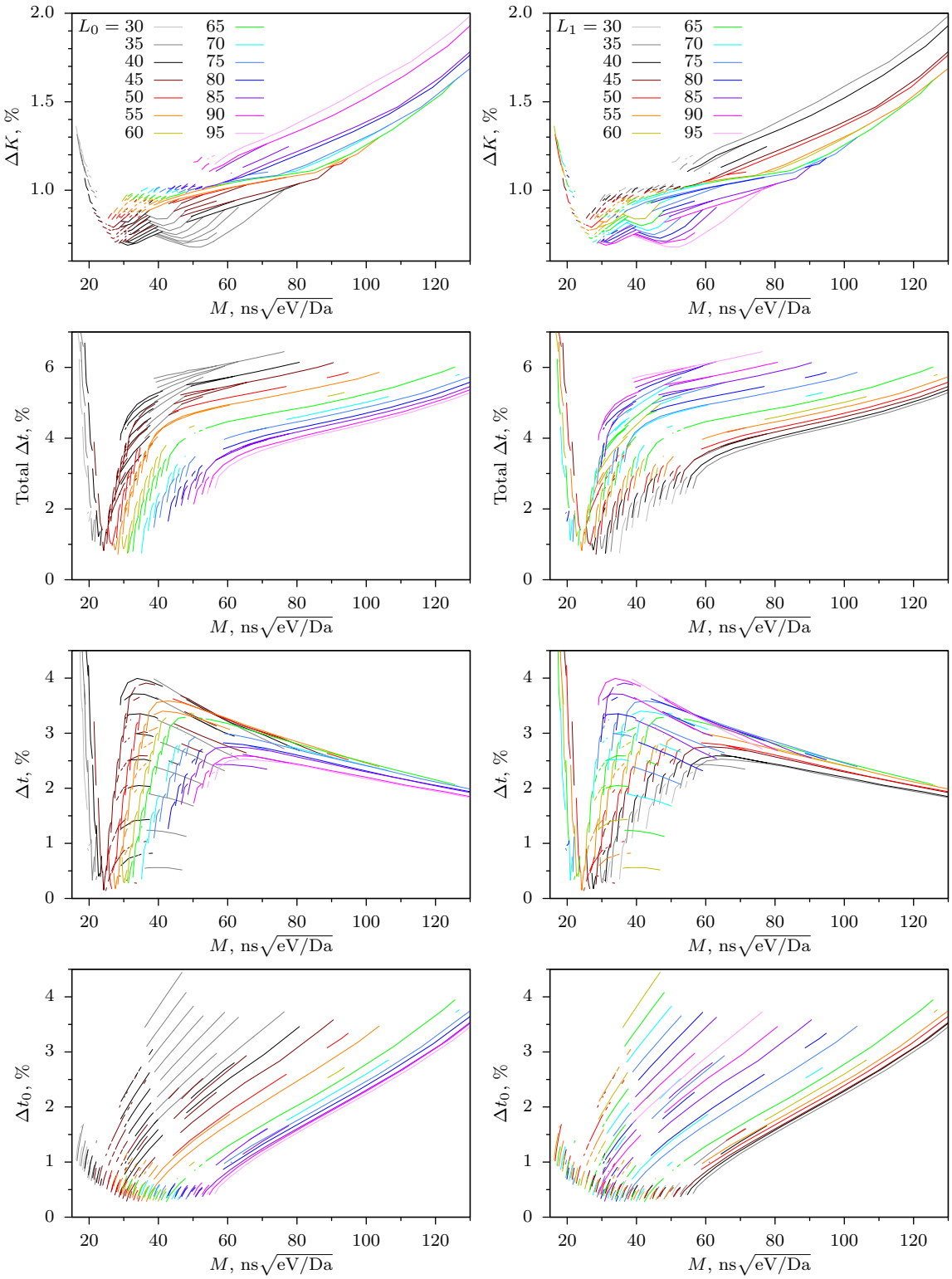

Figure 20 Relative overall kinetic energy and TOF resolutions as functions of magnification index. (Lengths L_0 and L_1 are in mm.)

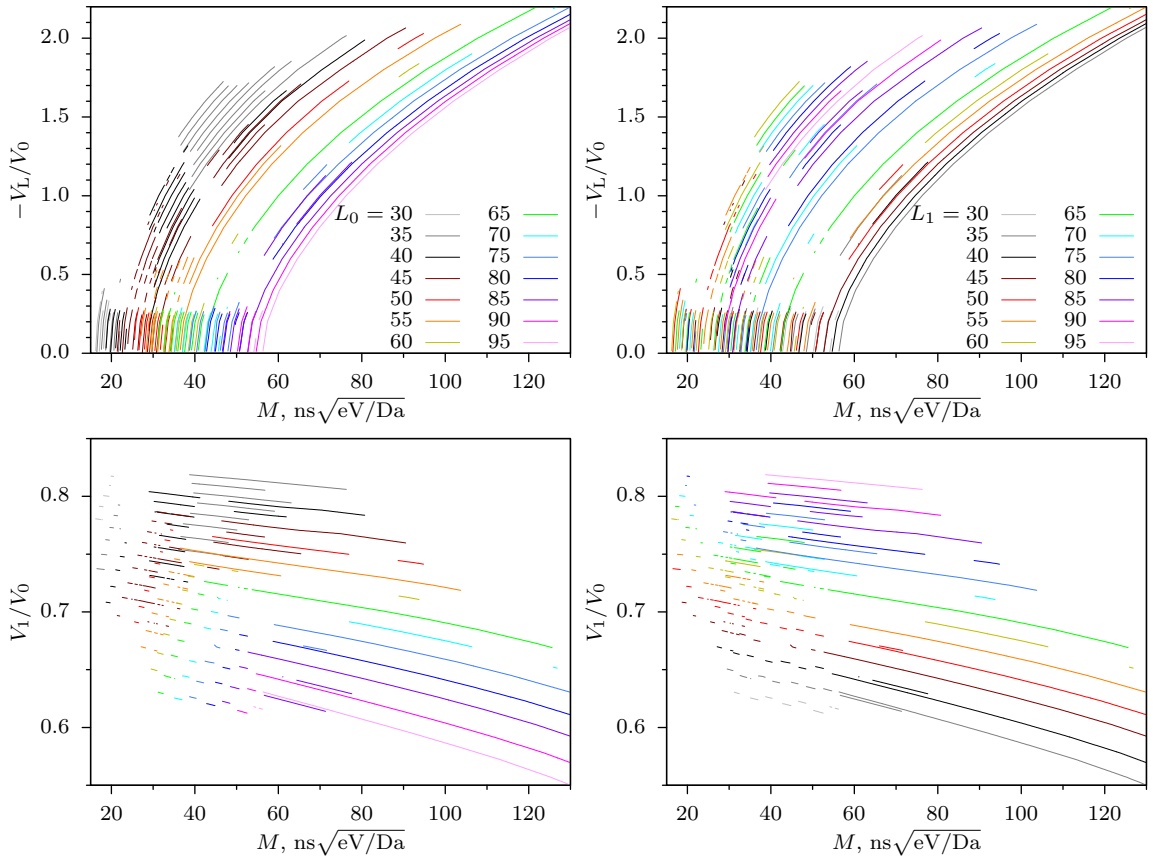

Figure 21 Interdependence of ion optics parameters and magnification index. (Lengths L_0 and L_1 are in mm.)

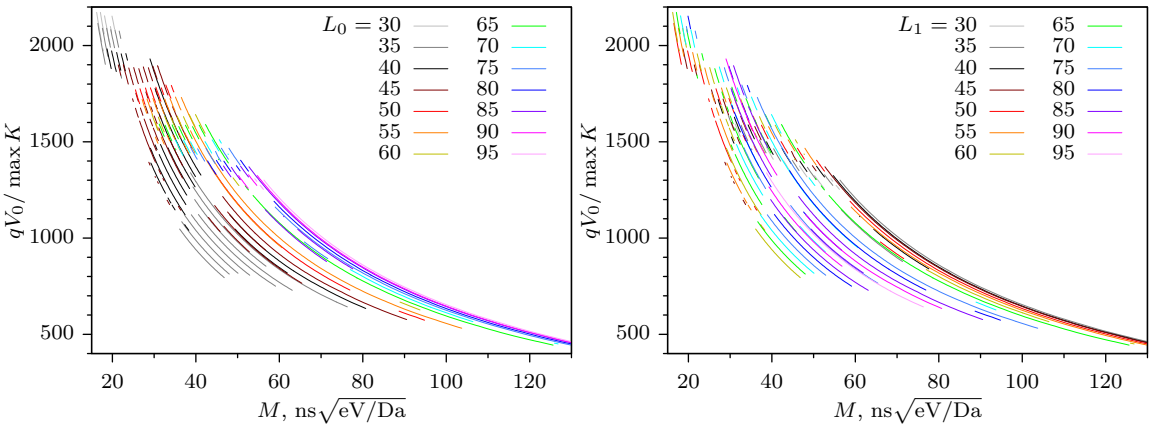

Figure 22 Dependence of voltage scale on imaged kinetic energy range and magnification index. (Lengths L_0 and L_1 are in mm.)

KEs (or only a narrow range is interesting for a particular measurement), then the distortion only for that range is relevant from the practical point of view. Such "partial" Δt_0 would be of course smaller than the overall Δt_0 and even becomes negligible for nearly monochromatic particles (not a very common but sometimes encountered case). Moreover, from a broader perspective, the designed ion-optical system can be used with a complete 3-dimensional detection with time resolution instead of slicing, and in that case the TOF distortion has no effect on the performance, since it can be corrected by data processing, but the TOF scatter becomes crucial for the final resolution.

These considerations show that the relative importance of different characteristics depends on the specific application. Comparison of the dependences plotted in figure 20 reveals that they often have mutually opposite behaviors, so that no conditions can reach the best performance in all respects at once. Therefore, it is fundamentally impossible to provide "the best" ion optics parameters for all cases.[1] Instead, the data shown in figures 20–22 provide the Pareto-optimal characteristics and parameters, out of which a specific combination should be selected based on the specific requirements in a particular experiment. The Pareto optimality with respect to ΔK and total Δt was used here, since these are the most important criteria for SVMI operation, but the plots optimal with respect to $\{\Delta K, \Delta t\}$ and $\{\Delta K, \Delta t_0\}$ are also provided in appendix B.

Although the figures might appear too small for practical use, this is not a prob-

[1] Simultaneous optimization of more than one characteristic is generally infeasible because simultaneous minimization of N objective functions $\{f_n\}_{n=1}^N$ dependent on M common parameters $\{p_m\}_{m=1}^M \equiv \mathbf{p}$ requires simultaneous satisfaction of $N \times M$ equations $\frac{\partial f_n}{\partial p_m} = 0$, which clearly cannot be done if $N > 1$. However, since such multi-objective optimization problems emerge quite often, some approaches to their solution were devised. In maximalistic approach, where the finite goal is well-understood and can be formalized, a single overall "aggregate objective function" is constructed from the individual objective functions (for example, as a linear combination $f = \sum_{n=1}^N w_n f_n$, where the weights w_n might depend on $\mathbf{p}$ as well), reducing the mathematical problem to a regular single-objective optimization. In the opposite, minimalistic, approach the trade-off decisions are postponed, and only the subset of parameter space is found from which the final "optimal" selection must be made based on some additional considerations. This subset, called the *Pareto set*, contains all parameter combinations that are optimal in the sense that for them no single characteristic can be improved without deteriorating other characteristics. All definitely worse parameter combinations $\mathbf{p}$, for which an unambiguously better $\mathbf{p}'$ exists (such that $f_i(\mathbf{p}') \leqslant f_i(\mathbf{p})$ for every i, and the inequality is strong for at least one i), are eliminated. However, giving a preference to one Pareto-optimal $\mathbf{p}$ over another is a trade-off decision and can be done only after an assessment of the relative importance of each characteristic, which might be different in different situations. So, although this approach does not provide a univocal answer to the optimization problem, it is still very useful because it maximally reduces the amount of data for further analysis.

lem in reality. First of all, the operation of the system is impossible without a computer (at least for data collection and analysis), and the figures in the electronic version of this dissertation can be magnified as much as necessary. If a greater precision in the numbers in needed, the tabular data used for the plots is also available on the working system. In addition, these data can be easily generated using SIMION and the files provided in appendix A, and the presence of this simulation framework is practically indispensable for efficient operation of the system. Second, as mentioned on p. 63, the main purpose of these plots for practical use is to provide sufficient information for selection of the starting point in optimization that should be performed for each particular situation. From this point of view, the precision of the plots is satisfactory even in the printed form.

For example, if a distribution of H fragments with $\max K \approx 0.5$ eV is to be recorded using SVMI with 5 ns effective slice thickness, a total TOF stretching of ~50 ns is required. These conditions lead to $M = 50\ \text{ns} \cdot \sqrt{0.5\ \text{eV}/1\ \text{Da}} \approx 35\ \text{ns}\sqrt{\text{eV/Da}}$. Using figure 20, many possible combinations of ion optics parameters can be chosen for this value of M. One of such combinations, corresponding to $\Delta K \approx 0.8\,\%$ and total $\Delta t \lesssim 4.5\,\%$ ($\Delta t \approx 2.5\,\%$, $\Delta t_0 \lesssim 2\,\%$) — intermediate values for all these performance characteristics, has $L_0 = 40$ mm, $L_1 = 70$ mm and, according to figure 21, $V_\text{L}/V_0 \approx -0.95$ and $V_1/V_0 \approx 0.76$. From figure 22, the ratio $qV_0/\max K \approx 1350$, and thus $V_0 = 1350 \times 0.5$ eV$/1e = 675$ V should be used. This corresponds to $V_1 = 513$ V and $V_\text{L} \approx -640$ V (rounded for convenience). Optimization starting from these parameters yields a more accurate value $V_1 = 516$ V and the characteristics: $\max K = 0.506$ eV, $\Delta K = 0.786\,\%$, $\tau_\text{max} = 49$ ns, $\Delta t = 1.24$ ns (~2.5 %), $\Delta t_0 = 0.92$ ns (~1.9 %) — all very close to the initial values taken from the plots.[1]

The temporal characteristics obtained for this combination of parameters indicate that if the worst case is indeed realized in the experiment, the total effective slice thickness would be $\gtrsim$7 ns (5 ns + total Δt), which comprises ~1/7 of the total TOF stretching and thus leads to an inner "wing" in the recorded distribution due to finite slicing thickness (see figure 2) with ~1 % $\Delta v/v$ extent for the max-

[1] Molecular beam velocity $v_\text{beam} = 0$ was used in these illustrative simulations, as well as for generation of the plots. This parameter has a relatively minor effect on the results for H fragments but becomes increasingly important for heavier particles (for example, for $v_\text{beam} = 1600$ m/s the initial kinetic energy due to the motion with the beam reaches 1 eV at $m \approx 80$ Da; this clearly causes a shift in the total TOF comparable to the TOF spread, but also has a noticeable effect on other characteristics due to chromatic aberrations of the ion optics). Optimization with the actual molecular beam velocity is recommended for all practical simulations.

imum velocity, or ~2 % $\Delta K/\max K$ for the whole kinetic energy range[1]. Although this additional broadening seems large compared to the resolution quoted above ($\Delta K = 0.786\,\%$), these 2 % correspond to the total spread, and the actual *effective* broadening is much smaller. Nevertheless, the wing length can be reduced to, say, ~1 % in KE by choosing longer TOF stretching. For instance, according to figure 20, at $M \approx 71\text{ ns}\sqrt{\text{eV/Da}}$ required for $\Delta\tau_{\max} \approx 100$ ns the ion optics parameters can be chosen to yield $\Delta K \approx 1\,\%$ and total $\Delta t \approx 5.5\,\%$ (that is, the total effective relative slice thickness will be about $(5\text{ ns}/100\text{ ns}) + 5.5\,\% \approx 1/10$ leading to $\Delta_s K \approx 1/100$). These parameters are: $L_0 = 45$ mm, $L_1 = 85$ mm, $V_L/V_0 \approx -1.72$, $V_1/V_0 \approx 0.77$ and $V_0 \approx 760 \times 0.5\text{ eV}/1e = 380$ V, from where $V_1 \approx 293$ V and $V_L \approx 655$ V. Optimization starting from these values results in $V_1 = 292$ V and $\max K = 0.497$ eV ($\Delta K = 0.99\,\%$) with $\Delta\tau_{\max} = 100$ ns (total $\Delta t = 5.8\,\%$).[2]

On the other hand, if the initial position distribution is known to be narrow along the ion-optical axis (that is, the ions are created by a focused laser) and stable during the experiment, then the experimental TOF scatter should be much smaller than the Δt values used for the present plots and thus can be mostly ignored. In that case the plots in figures B.4–B.6 (appendix B) would be more helpful. For example, parameters leading to minimal Δt_0 and maximal (but still reasonable) $\Delta K < 0.9\,\%$, namely, $L_0 =$ 55 mm and $L_1 = 70$ mm, can be selected for given $M = 35\text{ ns}\sqrt{\text{eV/Da}}$. This presents an example of operation without the additional lens ($V_L = 0$ according to figure B.5). The optimized parameters $V_0 = 865$ V and $V_1 = 645$ V (starting from $V_1 \approx 650$ V) yield $\max K = 0.499$ eV ($\Delta K = 0.875\,\%$) and $\Delta\tau_{\max} = 49.7$ ns with $\Delta t_0 = 0.15$ ns (only ~0.3 %). If, in addition to the initial position distribution properties specified above, the position of the ionization region is also known with precision better than the

[1]The extent of the wing becomes larger for lower velocities in the velocity scale, as can be understood from figure 2 and expression (7) multiplied by v_ρ, but remains constant everywhere in the KE scale. Namely, using figure 2 and relationship (48), for any given KE the maximal radius is $\max_{v_z} R(K) \sim \sqrt{K}$, and the minimal radius satisfies $\min_{v_z}[R(K)]^2 = \max_{v_z}[R(K)]^2 - (R_{\max}\Delta t_s/\Delta\tau_{\max})^2$, where Δt_s denotes the absolute time slice thickness. Substitution of the first relationship into the second and rearrangement of the terms shows that the range of projections in the KE scale does not depend on K and is simply $\Delta_s K = (\Delta t_s/\Delta\tau_{\max})^2 K_{\max}$. Obviously, for $K \leqslant (\Delta t_s/\Delta\tau_{\max})^2 K_{\max}$ the distribution is not sliced at all (for the considered example this limit is ~0.01 eV).

[2]The same parameters, but with all voltages increased by 2 times ($V_0 = 760$ V, $V_1 = 584$ V, $V_L = -1310$ V) can be used for D fragments with $K_{\max} \approx 1$ eV (since $M = 100\text{ ns} \cdot \sqrt{1\text{ eV}/2\text{ Da}} \approx 71\text{ ns}\sqrt{\text{eV/Da}}$ has the same value), or with all voltages increased by 4 times ($V_0 = 1520$ V, $V_1 = 1168$ V, $V_L = -2620$ V) — for SVMI of H distribution with $K_{\max} \approx 2$ eV with 50 ns stretching. However, the relative TOF characteristics in the latter case will be not as good, leading to the worst-case $\Delta_s K/\max K \approx [(5\text{ ns}/50\text{ ns}) + 5.8\,\%]^2 \approx 2.5\,\%$.

assumed ±0.5 mm, then the actual kinetic energy resolution should be better than this worst-case value. However, it would be advisable to redo the optimizations with a sample more relevant to the actual distribution, since the optimal parameters for such tightened conditions might be somewhat different and thus result in even better performance.

Of course, the ion-optical system can also be used for "regular" full-projection VMI without slicing. All temporal characteristics are unimportant for such application,[1] hence the best selection of ion optics parameters should correspond simply to the lowest ΔK value. As can be seen from the plots, these parameters are $L_0 = 45$ mm, $L_1 = 75$ mm, $V_1/V_0 \approx 0.77$ for operation without the additional lens ($V_\mathrm{L} = 0$) or $L_0 = 35$ mm, $L_1 = 95$ mm, $V_1/V_0 \approx 0.815$, $V_\mathrm{L}/V_0 \approx -1.5$ for operation with the lens. The latter option results in slightly better resolution, somewhat higher imaged KE range for the same maximum voltage (or lower required voltages for the same KE range), but ~1.5 times worse mass resolution due to greater TOF stretching. Unless the KE range is too large, requiring very high voltages applied to the accelerator, operation without the lens is preferred, since, besides providing better mass separation, it uses higher acceleration potentials, which leads to higher detection efficiency by the MCP detector.

Overall, the simulation results presented in figures 20–22 demonstrate that the magnification index can be changed from ~20 to ~130 ns$\sqrt{\mathrm{eV/Da}}$ while keeping the worst-case overall relative KE resolution better than 2 % and the total relative TOF deviations below ~6 %. For a broad range of magnifications (namely, below ~80 ns$\sqrt{\mathrm{eV/Da}}$) relative KE resolution of 1 % or better is achievable. For SVMI of H fragments using 50 ns TOF stretching, this $\Delta K \leqslant 2\,\%$ range corresponds to kinetic energies from ~0.16 to ~6.8 eV (or to ~2.5 eV for $\Delta K \leqslant 1\,\%$), although the upper limit might pose some practical difficulties due to relatively high required voltages ($V_\mathrm{L} \sim 7000$ V), and the low acceleration voltages ($V_0 \sim 300$ V) for the lower KE limit might lead to decreased detection efficiency. Nevertheless, the design goals set in section 2 can be considered satisfied. Example of simulations for operation near the lower and upper KE limits are shown in figure 23.

The optimizations described above dealt only with electrical parameters of the

[1] However, mass resolution, determined by some of the temporal characteristics, might be important in certain cases.

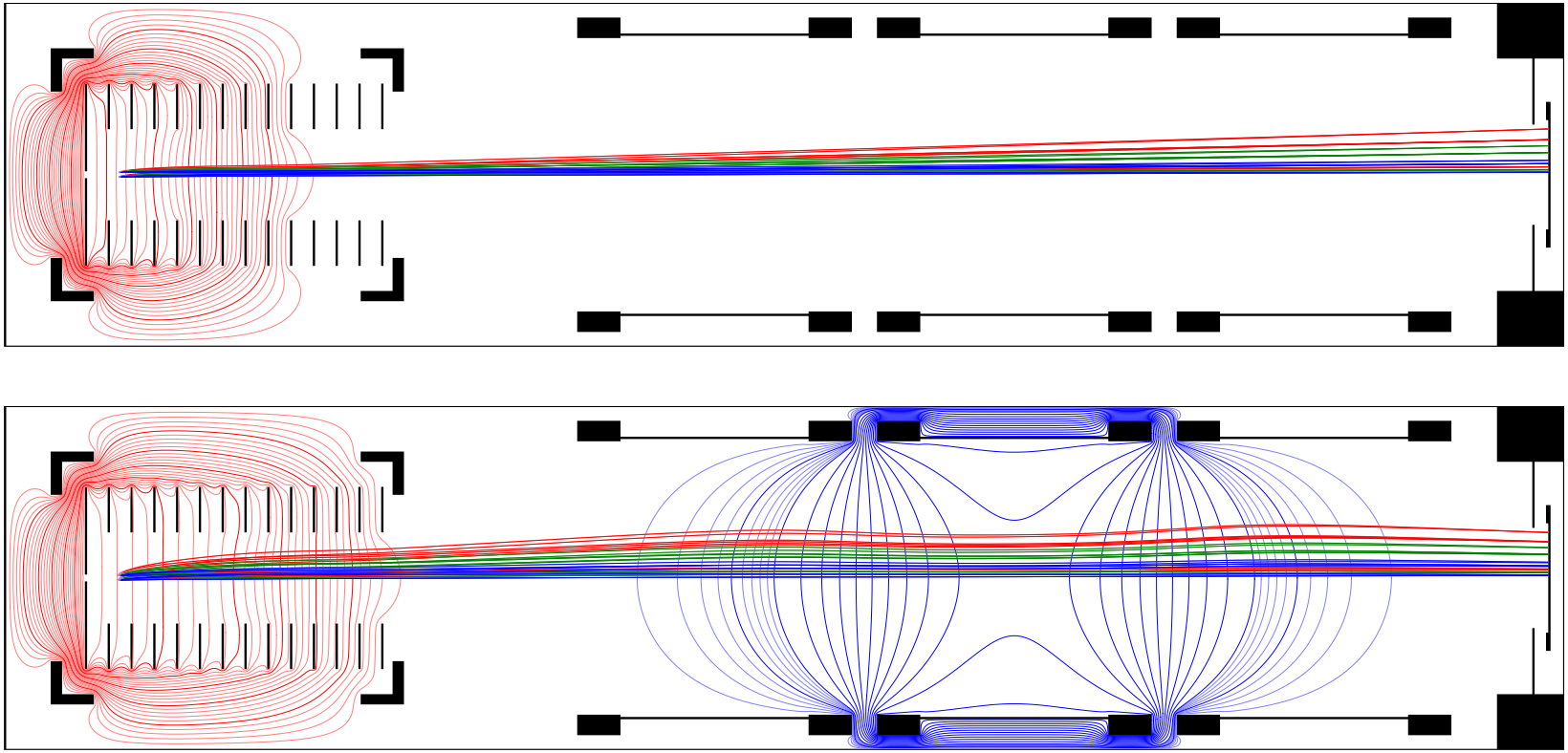

Figure 23 Illustration of electrostatic potentials and particle trajectories for the extreme operating conditions.
Top: lower KE limit ($K_{\max} = 0.163$ eV; $L_0 = 40$ mm, $L_1 = 50$ mm, $V_0 = 320$ V, $V_1 = 231.1$ V, $V_L = 0$); equipotential contours drawn with 10 V steps.
Bottom: upper KE limit ($K_{\max} = 6.75$ eV; $L_0 = 75$ mm, $L_1 = 55$ mm, $V_0 = 3000$ V, $V_1 = 1891$ V, $V_L = -6600$ V); equipotential contours drawn with 100 V steps (500 V steps below −1000 V).
In both cases $\Delta\tau_{\max} \approx 50$ ns. Trajectories correspond to the initial sample illustrated in figure 18.

system at a fixed geometry of the electrodes,[1] and therefore are not truly complete. As mentioned at the beginning of subsection 5.4, any changes to the geometry of the electrodes require complete recomputation of the electrostatic potential arrays. While this process is not more computationally demanding than a single voltage-optimization run, its integration with user programs in SIMION 8 is less smooth. Moreover, in contrast to the studied "electrical" optimizations, the geometry optimization must be performed for the whole operational range of the system, since by design the geometrical parameters cannot be adjusted in a working machine. That is, every geometry optimization cycle must involve a complete recomputation of all the datasets presented in this subsection. And even though their dependences on the varied geometrical parameters must be relatively smooth, which might be used for speeding up the recomputations to some extent, the effort required for such complete optimization and analysis significantly exceeds the amount of work needed to produce the partially optimized results described above.

Therefore, instead of the full optimization, it was decided to perform only several test simulations for a few variations of the geometry starting from the one described in subsections 5.1 and 5.2 in order to ensure that the chosen layout is not too far from the possible optimum. The accelerator was not modified from the arrangement optimal for the low-KE range operation without the additional lens (see subsection 4.3), but the influence of the additional lens position and the length of its central element on the resolution for operation at large M values was studied. It was found that a shorter lens ($0.5:1$ length-to-diameter ratio) leads to higher aberrations than the "standard" one ($1:1$ ratio), in accordance with the general results (see [29]), regardless of its position. At the same time, neither an increase of the length within the available space, nor small possible shifts of the lens within the drift region led to evident improvements of the performance. Since the lens already had the maximum practical diameter, it could be varied only towards smaller values, but simulations with 100 mm diameter expectedly showed larger aberrations.

Based on these tests, it was concluded that even if the present geometry is not perfectly optimal, it is still quite close to the optimum, and no significant improvement of the performance characteristics can be achieved within the used optical scheme. As mentioned at the beginning of this section, this scheme was chosen as the simplest

[1] Although the accelerator lengths were extensively varied, this was achieved by purely electrical means and thus is not an *electrode geometry* optimizations in the strict sense.

approach to the posed problem. Thus after a satisfactory solution was obtained in the numerical simulations, it was appropriate to perform experimental tests of the designed system and refine the practical demands from it before considering more complicated arrangements.

6 Implementation

As mentioned in section 2, the designed SVMI system was intended for retrofitting of the free-radical molecular beam apparatus used in the laboratory since 1998. A description of the apparatus construction is given in [13] and will not be repeated here. The only modifications to the vacuum chamber done in the present work were related to the "detection region" part and included removal of the TOF spectrometer assembly mounted on the top flange and replacement of the end flange[1] by a nipple[2] of the same diameter for axial extension of the chamber. The SVMI components added to the machine are described in the following subsections.

6.1 Ion optics

Since the arrangement of the electrodes in the designed ion-optical system is very simple, its implementation was relatively straightforward. However, some practical aspects had to be taken into account in the design of the supporting structures. The fact that the system must operate in high vacuum poses some restrictions on the selection of materials and requires to minimize the number of mating surfaces and avoid tight or enclosed spaces in order to reduce outgasing. The high voltages (up to a few kilovolts) applied to the electrodes require careful electrical insulation and sufficient spacings among them and from the grounded parts. For operation at lower voltages the possible electric charge accumulation[3] can lead to significant electric field distortions and thus must be eliminated at least in the vicinity of the important regions.

[1] Which had no function except hosting the vacuum gauge port.

[2] A standard $\varnothing 6''$ (~154 mm), $13.12''$ (336 mm) long nipple with $8''$ ConFlat-type flanges modified by addition of one port for vacuum gauge and one small flange for electrical feedthrough was ordered from MDC Vacuum Products. The whole piece was welded from nonmagnetic type 304 stainless steel standard components, and the inner surface electropolished by the company.

[3] From spurious charged particles hitting electrically insulating surfaces and from photoelectron emission caused by scattered light.

From a mechanical point of view, the supporting structures must provide reliable and precise positioning of the ion optics elements with respect to each other, as well as relative to the rest of the system — most importantly, the ionization region and the detector. For example, 1 mm displacement of the accelerator relative to the vacuum chamber will lead to the same 1 mm displacement of the ionization region from the designed position, which exceeds the initial volume dimensions assumed in the design and simulations. The 20 mm radius of the detector located ~600 mm away from the ionization region means that even ~2° misalignment of the accelerator axis from the vacuum chamber axis will place the center of the formed image outside the detector, and for efficient use of the whole detector area very careful centering of the image on the detector is required, leading to much tighter alignment tolerances.

Nevertheless, all of these problems are not unusual and can be solved with commonly available materials and manufacturing facilities available in a regular machine shop. For example, all custom-made parts required for assembly of the present system were made in the USC machine shops using materials ordered from McMaster-Carr Supply Company. The mechanical drawings of these parts are given in appendix C for reference. A schematic cutaway view of the whole ion-optical system installed in the "detection chamber" part of the apparatus is also shown in figure 24.

Accelerator assembly

The accelerator plates were made from stock oxygen-free copper sheets (1 mm thickness) by machining. All plates, except the first one, have the same shape as in the simulations (see p. 51): 80 mm outer diameter and 40 mm aperture diameter. The first plate has the same outer diameter, but instead of the aperture uses an orifice with ⌀3 mm opening and 90° chamfer on the inner side to admit the molecular beam inside the accelerator. All plates were electrochemically polished in the laboratory using the standard method [32] of anodic dissolution in 85 % (14 M) H_3PO_4. Although copper has a relatively poor machinability, this was not a problem for parts with such simple shapes. At the same time, it has excellent vacuum properties and allows very simple attachment of wire leads by soldering. Moreover, in contrast to many other metals and alloys, copper oxides are electrically conductive, which makes accumulation of stray surface charges impossible.

Mechanical fixation and electrical insulation of the plates was achieved by insert-

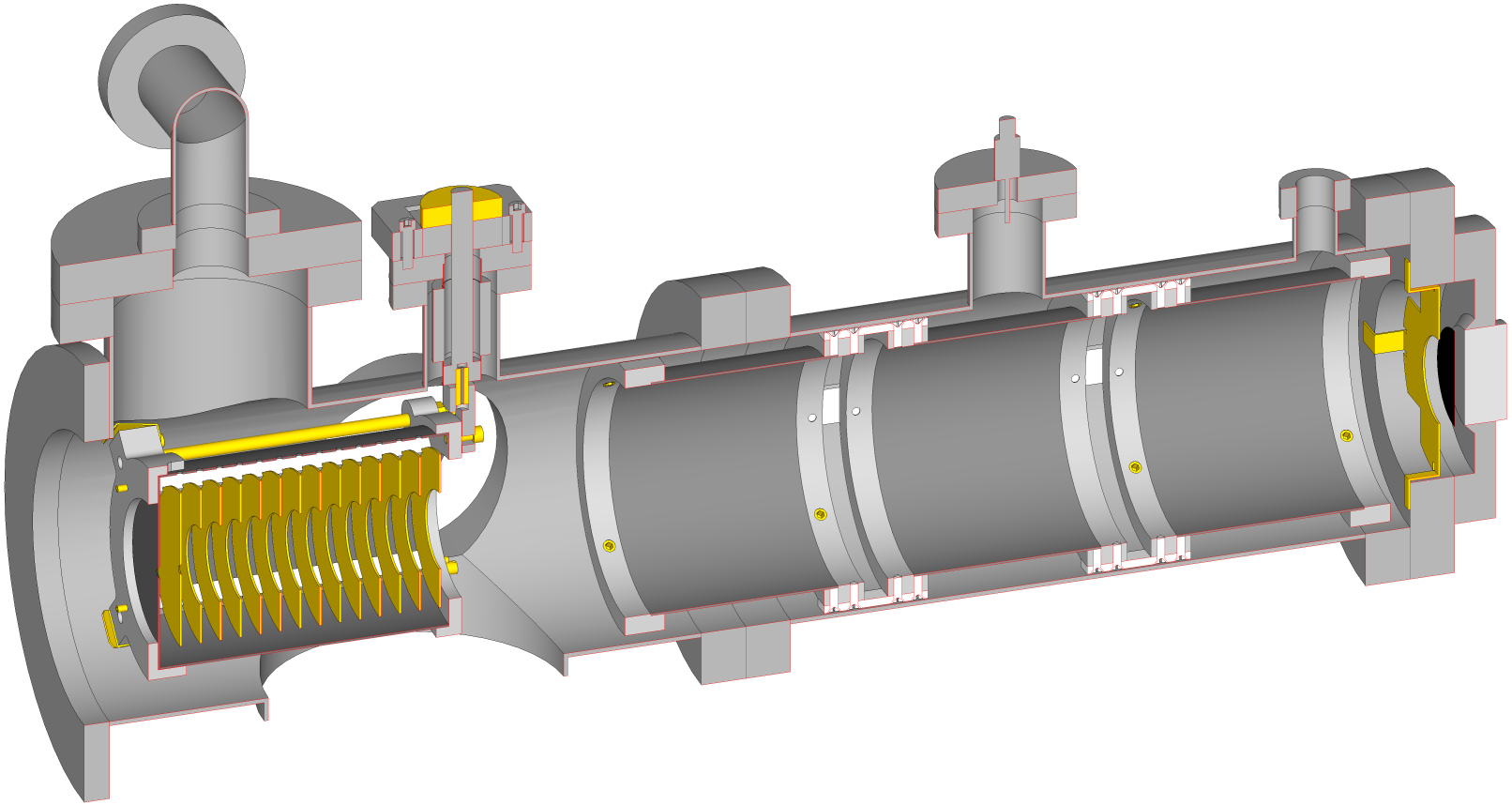

Figure 24 Schematic cutaway view of the designed VMI ion optics inside the detection chamber. Connecting wires and other parts of the apparatus are not shown. (The actual implementation also has minor differences mentioned in the text.)

ing them between four MACOR[1] bars with shallow grooves (see figure C.1). The bars are held between two nonmagnetic stainless steel rings, fixed and centered in radial direction by set screws on each side. The rings are tied together with four partially threaded bronze screws and nuts. The screws have an additional purpose of pushing out the bronze pins that anchor the entrance side of the whole accelerator assembly inside the vacuum chamber, as illustrated in figure 25.[2] Such design solution allows

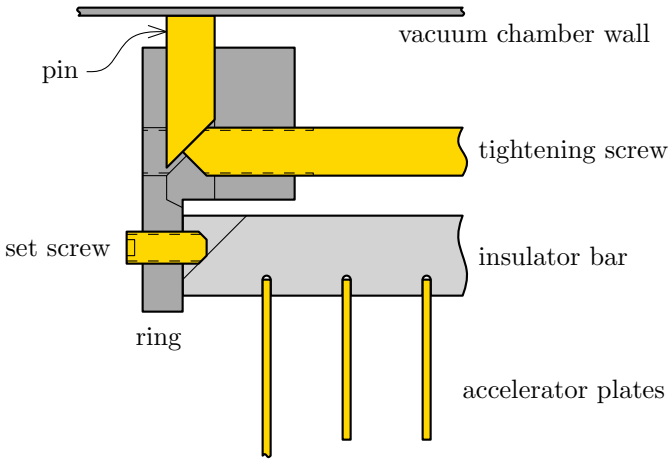

Figure 25 Schematic cutaway view (partial) of the accelerator assembly near the molecular beam entrance end.

very simple alignment of the accelerator entrance with the molecular beam skimmer (and hence the apparatus axis) by adjusting the four screws from the exit end (see figure C.3). This ability is very important in the present setup because the existing vacuum chamber has only a small ($\varnothing \sim 2$ cm) opening for the skimmer in the wall separating the source and detection regions, practically preventing any access from that end. Also, hanging the whole accelerator assembly on the top flange (see figure 24) in a sufficiently rigid and precisely adjustable manner would required a much more complicated construction.

On the other hand, the exit side of the accelerator could not be supported in the same fashion due to the large-diameter vacuum pump port located below it. More-

[1] A variety of glass-ceramic material with good machinability and vacuum properties.

[2] The original design, reflected in figure 24 and the drawings in appendix C, involved leaf springs between the pins and the chamber wall, but upon the implementation it became evident that the anchoring works fine even without these additional details, and they were not installed. The only practical disadvantage of the lack of these springs is that installation into (and removal from) the vacuum chamber must be done carefully in order to prevent the lower pins from falling through the vacuum pump port.

over, the tight angular alignment requirements (see p. 80) meant that the ability to perform adjustments from outside the vacuum chamber during system operation (for prompt feedback) would be very desirable. Therefore, the exit side was attached to a translational stage installed on the smaller top flange, as shown in figure 24. The stage allows small vertical and horizontal movements (perpendicular to the main apparatus axis)[1] of the exit end of the accelerator, and through that the accelerator axis can be aligned with the desired direction. While this alignment system does not provide a good precision or accuracy by itself, practical operation showed that its use with real-time feedback from the VMI acquisition system allows very simple and fast centering of the image with radial deviation $\lesssim 1\,\%$, and centering within ~1 pixel (at 1024×1024 px resolution) is possible with meticulous adjustments. The alignment stability was also found sufficient for all practical purposes.[2]

Figure 24 also shows mu-metal[3] magnetic shielding (in dark gray) of the accelerator consisting of an additional plate at the entrance and a cylindrical sheet surrounding the plates and insulator bars. It was included in the design as an option, but not installed in the present machine, since no operations with photoelectrons were planned in the initial stages of the present work, and the necessity of magnetic shielding for ions is relatively small. However, the shielding can be installed in the future if needed.

All electrical connections to the electrodes were made by means of high-vacuum compatible high-voltage insulated wires soldered to the outer edges of the copper plates. The wires, collected in one bunch (see figure C.1), were routed through the top flange of the vacuum chamber to a pair of multipin electrical feedthroughs.[4] Selection of the effective lengths L_0, L_1 and appropriate division of the voltages V_0, V_1 (provided by two commercial adjustable high-voltages power supplies) is performed

[1] Figure C.2 shows close-up pictures of this assembly. Rotation of the big brass nut moves the central screw vertically. The screw passes through the rectangular plate that can slide on the flange surface and thus displace the central screw horizontally. The bellows providing a vacuum seal between the central screw and the flange can be seen in the bottom view. The accelerator assembly is attached to the bottom of the central screw by means of a hook, the lower part of which can be seen in figure C.3.

[2] It appears that for the ion-optical system without magnetic shielding, image shifts due to variable stray magnetic fields might be more important than the alignment instability.

[3] A nickel-iron alloy with high magnetic permeability.

[4] Since all accelerator electrodes (except the last one, which is always grounded) require applications of different potentials, a high-voltage feedthrough with at least 13 pins was needed. However, no commercially available feedthroughs with such parameters were found at the time of construction, and thus a pair of 8-pin feedthroughs (from Insulator Seal, a part of MDC Vacuum Products) installed on a tee adapter (see figure 24) was used instead.

with a voltage divider (see figure D.1 in appendix D) installed outside the vacuum chamber.

Lens assembly

Implementation of the lens was more straightforward than that of the accelerator. It basically followed the construction described in subsection 5.2 and is clearly seen in figure C.4. All rings were made from the same nonmagnetic stainless steel as the accelerator rings. The central parts of each electrode were made from cylindrically bent metal sheets.[1] The grounded outer elements use four brass set screws in each ring for anchoring inside the vacuum chamber. The rings of the central element are attached to the inner rings of the outer elements by MACOR insulator strips fastened with stainless steel (to the grounded parts) and nylon (to the high-voltage parts) screws.

The whole assembly was radially centered in the vacuum chamber by symmetric adjustment of all 16 set screws such that the assembly can be inserted into the chamber freely but without radial play, then positioned correctly in the axial direction relative to the open detector end of the chamber extension, and fixed by symmetric tightening of the set screws.

6.2 Charged particle detector

A standard ⌀40 mm double-stack imaging MCP detector assembly (Galileo Electro-Optics[2] 3040FM series; ⌀10 μm pore) already kept in the laboratory as a spare for the other VMI setup (see [14]) was used in the initial stage of the work. The CF6″ flange of the detector was mounted at the end CF8″ flange of the extended vacuum chamber through a "zero-length" adapter[3], as shown in figure 24. An electric shield made from oxygen-free copper sheet was attached at the vacuum side of the adapter in order to protect the near-detector part of the drift region from electric fields created by the unshielded high-voltage wires of the detector assembly.

[1] Perforated nonmagnetic stainless steel sheet was used in the present machine, but it can be replaced with mu-metal sheet, if magnetic shielding of the drift region is desired.
[2] Now PHOTONIS USA.
[3] Ordered from MDC Vacuum Products and slightly modified in the USC machine shops to accommodate the electrical feedthroughs of the detector.

The detector can be used in two different modes. The main, imaging, mode is employed in all VMI measurements. The other, electrical signal pickup, mode, where the total amplified ion (or electron) signal is collected from the phosphor screen electrode, is used for TOF-MS measurements, TOF spectrum examination in preparation for VMI (and especially SVMI) measurements, and auxiliary diagnostics. Despite significant differences between these two modes, they share some common properties.

For example, the detector input (front plate of the MCP stack) is always kept at the same voltage. This voltage was assumed to be zero in the simulations (see subsections 5.4 and 5.5) in order to have a field-free region near the detector. However, experimental tests of the implemented system (see next section) revealed that during operation with negative voltages applied to the additional lens, spurious "tails" can appear in the TOF signal after otherwise normal peaks. The origin of this effect is very simple. The particles (ions) being detected produce secondary electrons upon impact on the detector input surface. Those electrons that enter the MCP channels create the useful signal by avalanche amplification. At the same time, some electrons are ejected from the detector and do not contribute to the signal immediately. In absence of electric fields they fly away and are eventually absorbed by the grounded vacuum chamber walls or other surfaces. But when a negative voltage is applied to the lens, some of the electrons are diverted by it back to the detector and upon arrival are "detected" as genuine particles. The initial velocity distribution of these secondary electrons and the electric field strength in the lens determine the temporal extent and the intensity of the produced signal tails. However, the experiments indicated that the electrons contributing to the unwanted effect have relatively small kinetic energies, and application of a small negative voltage (-5 V in the presented case) to the detector input creates a sufficient electric field to divert the majority of them[1], so that the spurious tails disappear. Yet the employed potential is much smaller than characteristic energies of the actual particles accelerated from the ionization region and therefore does not introduce noticeable changes in the system properties.[2] The circuit diagram of the bias voltage supply is given in figure D.2 (appendix D). Besides

[1] Obviously, no voltage can *prevent* the particles from returning, since the total energy is conserved in electrostatic fields, and the returning particles will regain their initial kinetic energies at the detector, regardless of its absolute potential.

[2] Minor decreases in the total TOF were observed only starting from -20 V. No effect on VMI operation even at low ion optics voltages was observed for the -5 V detector bias. Nevertheless, the simulations framework (see subsection 5.4) allows variation of the detector potential, and the actual value -5 V was used in all simulations mentioned below.

the DC bias voltage, it provides AC grounding for the front of the MCP stack, so that the transient performance (for both signal pickup and gating) is not affected.

Detector operation in electrical signal pickup mode requires application of up to ~2 kV potential difference across the MCP stack and ~200 V bias of the phosphor screen, working as the anode, relative to the MCP output for effective collection of the produced electrons. The signal is usually picked up as anode current. Operating the whole assembly with input at nearly ground potential means that the output inevitably has an ~2 kV potential above ground, and the small useful signal must be separated from this large DC voltage offset. All these demands are handled by a simple divider–decoupler (see figure D.3). It rejects high-frequency noise from the single supplied high voltage, divides the potential between the anode and the MCP stack, and decouples the anode current from the high-voltage supply. The input impedance (50 Ohm) of a fast voltage amplifier (KOTA Microcircuits KE104, 1100 MHz bandwidth, 5× voltage gain) connected to the circuit output converts this current to voltage, and the amplified signal is transmitted to the measurement system.

The operation in imaging mode requires application of a much higher voltage (~5 kV) to the phosphor screen for improved conversion efficiency. This voltage is provided by a simple custom-built power supply (see figure D.4). Mass gating in "regular" VMI experiments and slicing time selection in SVMI experiments are performed by application of short (~100…200 ns for mass gating and ~5 ns for slicing) high-voltage pulses to the back of the MCP stack at appropriate times. Two different HV pulse generators are used for this purpose.

The mass gating pulse for full-projection VMI is produced by an AV-HVX-1000A high-voltage pulser commercially produced by Avtec[1]. The pulser essentially consists of a fast high-voltage MOSFET switch with triggering electronics and connects an external voltage supply to the load for an amount of time specified by the incoming TTL trigger pulse. While the voltage rise time provided by the switch is ~10 ns, the pulser has no discharge circuit, and thus the voltage fall time for loads with nonzero capacitance (such as the MCP stack) is much longer. Moreover, the maximum output voltage is strictly limited to 850 V, which is insufficient for operation of the detector. Nevertheless, with a simple additional circuit (see figure D.6) that provides quick discharging of the load and impedance matching between the pulser and the detector (to

[1]Now Directed Energy (DEI).

avoid electrical ringing), and allows addition of a DC bias voltage V_{bias} to the output from another voltage supply, electrical pulses of trapezoidal form shown in figure 26 with rise and fall times $t_{\text{rise}} \approx t_{\text{fall}} \approx 20$ ns and sustained voltages V_{max} up to 2 kV

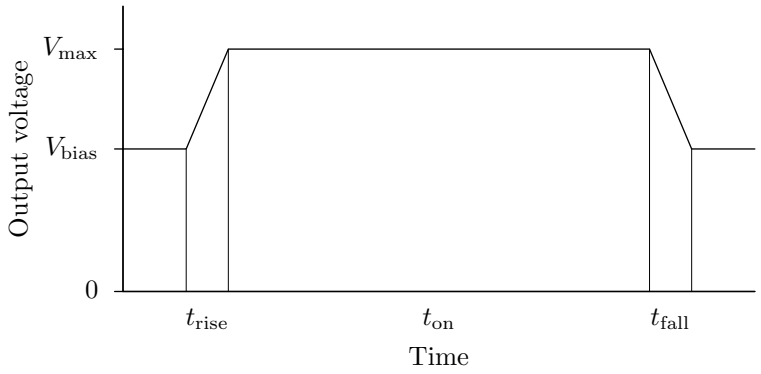

Figure 26 Mass gating pulse shape.

for adjustable duration t_{on} from ~70 ns to ~1 μs can be obtained. A simple custom-built power supply (see figure D.5) installed with the pulser and the combiner circuit near the detector provides voltage for the fixed 700 V pulse amplitude[1], whereas the bias voltage is provided and controlled by a commercial power supply installed in the common electronics rack. Despite the ~1200 V bias constantly supplied to the MCP stack, no detectable background signal is produced outside the active pulse phase thanks to the exponential voltage–gain characteristic of the detector.[2]

The slicing pulse for SVMI measurements is provided by a fast high-voltage electrical pulser built in the laboratory, under guidance of Dr. András Kuthi from the Pulsed Power Laboratory at USC. A detailed description of the pulser is given in appendix E. The features relevant to SVMI applications include the ability to gate the employed detector with a relatively clean electrical pulse[3] having fixed duration with ~5 ns halfwidth and amplitude adjustable in the whole working range of the detector (that is, up to ~2 kV). Although the delay between the trigger input and the high-voltage pulse output is ~900 ns, the jitter of the output pulse timing is $\lesssim$1 ns, which

[1] An amplitude somewhat below the maximum allowed 850 V is used in order to protect the MOSFET switch from breakdown by possible voltage overshots during transient processes after the fast switch opening.

[2] The gain increase is approximately two times per each 100 V, thus 700 V difference leads to >100-fold gain suppression, lowering the signal intensity well below the event counting threshold.

[3] The electrical pulse consists of one narrow high-amplitude peak and some surrounding stray oscillations that have a much lower amplitude and thus do not affect the detector gating.

does not exceed the timing jitter of the employed lasers used for fragment ionization.

The effective slice thickness is determined by convolution of the ionization intensity time profile, the detector gain time profile, and the relative timing jitter distribution (see p. 12). Although the optical intensity of the ionizing laser pulse also has temporal halfwidth of a few nanoseconds,[1] the nonlinearities in the ionization process, as well as in the voltage–gain dependence of the detector, lead to some narrowing of the effective temporal distribution. The characteristics of the resulting effective slicing pulse can be easily determined experimentally by "slicing" the photoelectron distribution produced by the ionizing laser. Due to the very small mass of the electrons, their TOF spread, especially if high acceleration fields are used, is also small, as evident from (35). For example, electrons with initial energies $K_0 = 1$ eV created in electric field $E_0 = 100$ V/cm have TOF spread $\Delta\tau_{K_0} \approx 0.7$ ns, and it can be reduced even more by using stronger electric fields. Therefore, the total photoelectron signal intensity measured as a function of the delay between the ionizing laser trigger and the slicing pulse trigger reproduces the effective slicing pulse profile with <1 ns resolution. An example of such profile measured during experimental tests of the present system (see next section) using H atom ionization laser is shown in figure 27. As

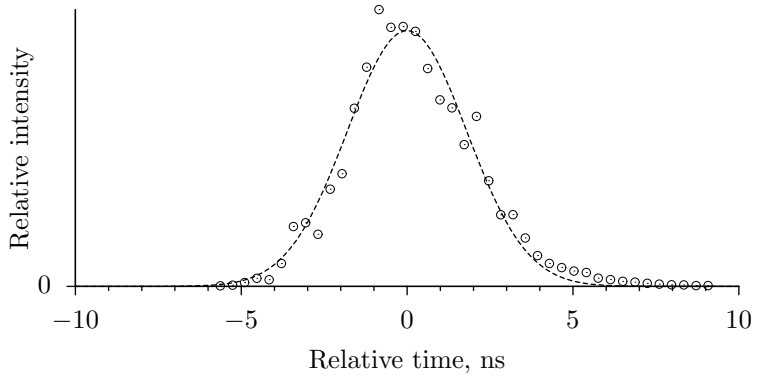

Figure 27 Time profile of effective slicing pulse. Points represent experimental data. Fitted Gaussian profile is shown by dotted line.

can be seen from comparison with the fitted curve, the actual profile has a nearly Gaussian shape. The halfwidth of the fitted Gaussian is 4.24 ± 0.13 ns in this particular case, and this value is typical for all experiments conducted using the present experimental setup.

[1] Which means that the ~5 ns halfwidth of the detector gating pulse is a good match in regard to the intensity–resolution tradeoff, as mentioned on p. 12.

6.3 Image acquisition and analysis

The optical image produced on the detector phosphor screen is captured by a regular digital videocamera (PixeLINK PL-B741F) connected to a personal computer. The camera has a 8.58 mm × 6.86 mm CMOS sensor with 1280 × 1024 px resolution, out of which the central 1024 × 1024 px region is used for image acquisition in the present system. Although the quantum efficiency of CMOS sensors is generally lower than that of CCD sensors, they are several times cheaper (for the same physical size) and allow several times faster readout (up to ~30 frames per second in the present case), which facilitates synchronous real-time analysis of the data for each laser pulse (10 Hz repetition rate in the current experiments).

The objective lens was carefully selected for maximum performance of the image transfer from the detector screen to the camera sensor. The Tamron 23FM25SP lens with 25 mm focal length and $f/1.4$ aperture was chosen for this purpose. It has extremely low geometrical distortions and guarantees megapixel resolution over the whole field of view, perfectly matching the employed camera sensor characteristics. The minimal object distance of 15 cm results in exact matching of the produced image size with the detector size, maximizing both the resolution and the light collection efficiency.

The images captured by the camera for each laser pulse are transferred to the experiment-controlling computer for real-time processing. Out of 10-bit intensity resolution of the camera only 8 bits are used, as this was found sufficient for analysis and reduces the computational costs[1]. An event-counting algorithm used for determination of particles arrival positions from the raw image data is similar to the approach described in [33].

Each frame, after subtraction of the background (see below), is scanned for connected groups of pixels[2] with intensities above a predefined threshold. Each found group is analyzed in the following way. If the number of pixels in the group is below one predefined value, it is considered as a noise fluctuation and ignored. On the other hand, if the number exceeds another predefined value, the spot is treated as a cluster of multiple close-lying particle hits and is written to the output file as raw data

[1] However, with the current implementation the processor load of the employed regular desktop computer (AMD Athlon II X2 250, 3 GHz processor) usually does not exceed ~30 %.

[2] 4- and 8-connectivity were tested, and 4-connectivity was found to perform better, in particular with respect to separation of close-lying spots and rejection of near-threshold noise.

for further analysis.[1] If the group passes these preliminary tests, it is regarded as a candidate for a single-hit spot, and additional statistical parameters are calculated from the pixel values. The most important parameters are the hit coordinates (X,Y) determined as weighted averages of pixel coordinates (X_i,Y_i):

$$X = \frac{\sum I_i X_i}{\sum I_i}, \quad Y = \frac{\sum I_i Y_i}{\sum I_i}, \tag{86}$$

where I_i are the pixel intensities, and the sums are taken over all pixels in the group. Besides that, the geometrical form of the spot is estimated from the standard deviations

$$\sigma_X = \sqrt{\frac{N}{N-1}\frac{\sum I_i (X_i - X)^2}{\sum I_i}}, \quad \sigma_Y = \sqrt{\frac{N}{N-1}\frac{\sum I_i (Y_i - Y)^2}{\sum I_i}} \tag{87}$$

(where N is the number of pixels in the group) of the intensity distribution, and if they do not fall into a predefined interval, the group is again treated in the same way as in the initial coarse size filtering.

For all groups that passed these tests the determined parameters (plus the maximal and total intensities within each group) are recorded to the output file grouped by frames. The frame sequence number and time of acquisition are also recorded. While in the simplest case further processing of the data in order to obtained a rasterized velocity map image uses only the hit coordinates of all spots, the additional information turns out to be very useful for more advanced filtering and analysis of the data, including diagnostic and optimization purposes. Each acquired frame is also displayed on the computer screen in real time, with the analyzed spots highlighted by different colors according to their types, facilitating initial experimental preparations and providing convenient visual monitoring during data collection.

The background subtraction mentioned above is implemented with a fully automatic adaptive method. It is based on background estimation using a pixelwise

[1] For example, more complicated multipeak fitting algorithms can be used to extract the positions of each hit within the cluster. In the present work, however, the number of such clusters was much smaller than the number of single hits, and therefore it was decided to simply ignore them. This might be not the best solution, since rejection of multihit spots, in principle, leads to nonlinear intensity response of the system, decreasing the measured intensity of the most intense image parts (where the multihit probability is higher). On the other hand, another simple treatment, where a single hit is assigned to the cluster center, is not much better from the intensity perspective, but additionally introduces spurious hit positions (which were not present in the actual distribution) into the measurement results.

average of a certain number[1] of previous frames. The average, however, is not unconditional: from each frame only the pixels that were not identified as belonging to particle hit spots are taken, but all detected spots are excluded from the background estimation. This approach prevents estimated background intensity buildup leading to desensitization in the high-intensity areas of the image, and at the same time completely eliminates any fixed-pattern background, as well as all background contributions slowly changing in time. From a practical perspective, this allows reliable event counting operation even in the presence of ambient light.[2]

7 Experimental tests

The newly built system required experimental characterization before it could be used in actual scientific experiments. The test program carried out for that purpose included: experimental validation of the numerical model (see subsection 5.4), studies of the reliability of the optimal parameters obtained in the simulations (see subsection 5.4), development of experimental procedures, and calibration of the velocity mapping for further measurements.

The experimental tests were performed with ions created by well-studied processes and thus having well-known properties. For most tests the multiphoton dissociation of O_2 molecule at $\nu = 44\,444$ cm^{-1} ($\lambda = 225$ nm) eventually producing O^+ ions was used. This reaction has been widely employed for characterization of VMI systems since their invention [7] and has several appealing properties. First, the initial step involves a resonant 2-photon absorption [34], which allows selection of a single rotational level as the initial state of the molecule by proper tuning of the excitation laser. Second, the following steps involve either dissociation of the excited neutral molecule into atomic fragments created in a few different electronic (spin–orbit) states and subsequent photoionization of the produced excited atoms, or photoionization of the molecule with formation of O_2^+ ion in several vibrational states[3] and its subsequent photodissociation. In both cases the internal energy of the parent

[1] 8 was found to be a good choice, at least for the present system.

[2] For example, regular room lighting in the laboratory has no obvious detrimental effect on the present setup. However, a few frames immediately after abrupt changes in the lighting conditions might be spoiled, and therefore optical shielding of the detector–camera pair from external light sources is still preferable.

[3] The rotational state associated with nuclear motion is not strictly preserved upon ionization, but the probability of changing it by more than a few quanta is very low.

molecule (or molecular ion) immediately before the photodissociation step is well-defined, and the possible internal energies of the fragments (O^* or O^+) are known precisely. Therefore, the kinetic energy distribution of the dissociation products consists of several sharp peaks,[1] positions of which are determined by the excitation photon energy and the energy conservation law and thus can be accurately predicted.[2] These peaks have different intensities and anisotropies and span a KE range from ~0.1 to ~1.65 eV, presenting a very convenient distribution for characterization of VMI setup capabilities. Although the creation of O^+ from O_2 requires a total of 4 photons (in either case), the overall efficiency is high enough, so that laser pulse energies well below 1 mJ (focused) and only a few percent of O_2 in the molecular beam[3] are sufficient for the experiments. Moreover, only one laser is required, eliminating mutual alignment and synchronization issues. In addition to all these favorable properties the process has a useful side effect: some of the created "intermediate" O_2^+ ions do not dissociate. They retain essentially zero velocity and also present a convenient tool for other types of studies (for example, TOF properties and spatial effects).

Testing of performance for H fragments — the main object of the intended applications — was more difficult. Unfortunately, no convenient sources of them were found. Among all stable volatile diatomics containing H, only HBr was suitable from the experimental point of view. On the one hand, it has favorable properties: photodissociation in a broad range of photon energies, including $\nu = 44\,444$ cm^{-1} (facilitating switching from experiments with O_2), and formation of fragments in only two possible states, $H(^1S_{1/2}) + Br(^2P^\circ_{3/2})$ and $H(^1S_{1/2}) + Br^*(^2P^\circ_{1/2})$, with well known energies[4]. On the other hand, the resulting KE distribution with only two peaks is too sparse for complete characterization of VMI. Photodissociation of HBr is a 1-photon process with excitation directly to a repulsive electronic state. Therefore, no selectivity of initial states is possible. Nevertheless, the characteristic rotational temperature in the employed molecular beam is of the order of 10…20 K, meaning that the initial

[1] The velocity change due to electron recoil upon ionization is quite small because of the large ion/electron mass ratio and does not exceed the initial velocity spread in the molecular beam.

[2] The dissociation energy of O_2 involved in the energy balance equation has been experimentally determined with accuracy exceeding the VMI resolving capabilities (namely, $D_0(O_2 \to 2O(^3P_2)) = 41\,268.6 \pm 1.1$ cm^{-1}, according to the analysis reported in [35]). Other energies are known with even better "spectroscopic" accuracy.

[3] Even ordinary atmospheric air at somewhat higher concentration can be used instead of pure oxygen.

[4] HBr dissociation energy is $30\,210 \pm 40$ cm^{-1} [36] for the H + Br channel and 3685 cm^{-1} higher [37] for the H + Br* channel.

internal energy distribution is already sufficiently narrow.[1]

Dissociation of polyatomic molecules usually produces H fragments with broad kinetic energy distributions due to the high density of states available in the molecular cofragment and the absence of strong selectivity among them. The resulting kinetic energy spectrum is therefore too dense to be resolved by VMI instruments. A relatively sharp distribution is possible only when the cofragment is a diatomic with broad vibrational and rotational structures. That is, triatomic volatile hydrides might be suitable sources of well-structured H fragments distributions. The most common of them, H_2O, could be a good choice. As shown in [38], it is photodissociated by Ly-α radiation ($\nu = 82259$ cm, $\lambda = 121.57$ nm) — the same radiation that is used in detection of H fragments (by REMPI through the $2p$ state), allowing experiments without additional light sources — and produces a distribution with rich and sharp structure in the $0\ldots\sim3.1$ eV KE range.[2] However, the overall process of creating H^+ ions from H_2O requires two Ly-α photons. Unfortunately, the intensity of the VUV radiation produced by the employed tripling cell (see [13] and also [39] for more details), being acceptable for H detection purposes, was found too low for obtaining a sufficient signal level in such experiments. Attempts to perform multiphoton dissociation of H_2O with a separate laser also did not lead to a ready success and were abandoned. On the other hand, photodissociation of H_2S in the same UV range as in O_2 and HBr experiments is quite efficient and was successfully used in this work. It produces H($1s$) atom and HS radical in two spin-orbit states $X^2\Pi_{3/2,1/2}$ separated by only ~380 cm^{-1} (~0.05 eV)[3] and with some rotational excitation.[4] This situation is somewhat closer to the expected applications of the system (photodissociation of small polyatomic organic radicals) and allows to examine the SVMI performance for close-lying peaks broadened by rotational envelopes.

[1] The first vibrational level of HBr is ~2600 cm^{-1} above the ground state and should not be populated even at room temperature.

[2] The distribution actually extend to the limiting KE value $h\nu - D_0 \approx 5.1$ eV, but its intensity above ~3.1 eV drops significantly.

[3] The more accurate value 376.8 cm^{-1} and the H_2S dissociation energy 31451 ± 4 cm^{-1} are summarized in [40].

[4] Experiments at higher excitation energy ~52000 cm^{-1} (193 nm from ArF excimer laser) indicate that excitation of a few vibrational levels in HS ($\omega_e \sim 2700$ cm^{-1}) is also possible (see, for example, [41]). However, it was not observed in the present work, perhaps due to a difference in dissociation dynamics at different excitation energies.

7.1 Using O^+ and O_2^+ from O_2

The tests started from obtaining O_2^+ and O^+ signals in mass-spectrometer mode. After the experimental condition "external" to the VMI system were established, the detection was switched to imaging mode, and the accelerator configuration and voltages were set according to one of the suitable simulations results.[1] A preliminary velocity-map image was observed similar in appearance to the expected one, indicating that the system is functioning correctly at the basic level.

The first VMI test was the validation of the simulated parameters required to satisfy the focusing conditions. The radial and TOF focusing parts were tested separately, but using very similar approaches. As discussed in subsections 4.1 and 4.2, the radial focusing deals mostly with the initial position uncertainty in the radial direction (δx and δy), whereas the TOF focusing — with displacements along the ion-optical axis (δz). The intersection of the focused laser beam with the molecular beam creates an ionization region narrow in the y and z directions but elongated in the x direction, as depicted in the left part of figure 17. While the Δx elongation (or position along the x axis) cannot be easily varied in the experiment, the position of the ionization region along the y and z axes can be changed simply by parallel shifting of the laser beam before in enters into the vacuum chamber. In practice this shift was achieved by placing a 3.2-mm thick fused silica plano-parallel plate[2] after the laser beam focusing lens, as shown in figure 28. Rotation of the plate around its

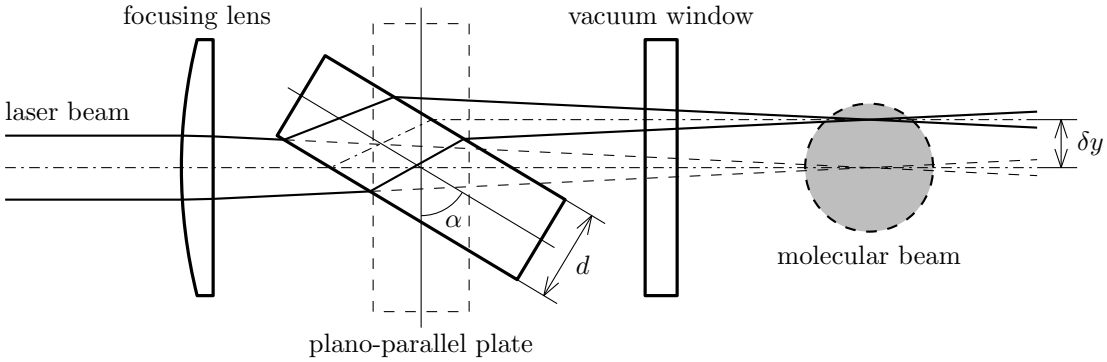

Figure 28 Diagram of using rotating plano-parallel plate for changing ionization region position in focusing tests. (Drawing not to scale.)

[1] Since the tests were organized in a stepwise manner, to make sure that simple components work as expected before studying the behavior of more complicated arrangements, the initial operation did not involve the additional lens (that is, its central element was grounded).

[2] A regular 1/8-inch thick spare vacuum chamber window was used.

horizontal axis displaces the transmitted beam, and therefore the ionization region, vertically without significantly affecting other parameters. The displacement δy can be controlled quickly and to a good precision by adjusting the rotation angle α:

$$\delta y = \frac{\sin(\alpha - \beta)}{\cos\beta} d, \quad \text{where} \quad \beta = \arcsin\frac{\sin\alpha}{n}, \tag{88}$$

d is the thickness of the plate and n is the refractive index of its material ($n \approx 1.52$ at $\lambda = 225$ nm). For example, rotation by 5° shifts the beam by ~0.1 mm, and the shift at 60° is ~1.7 mm.

If the focusing conditions are met, the image produced at the detector should not depend on the initial position of the particles. Conversely, if the conditions deviate from the proper ones, then the images taken at the laser beam displaced upward and downward are shifted with respect to each other in the vertical direction. Hence studying the dependence of this relative shift on the ion optics parameters allows to find the experimental values at which the shift turns to zero, and therefore the focusing is achieved. This procedure was performed for several combination of the accelerator lengths using fixed V_0 and varying V_1, first without the additional lens ($V_\mathrm{L} = 0$) and then at a few different V_L values.

Likewise, the TOF focusing was tested by displacing the laser beam in the horizontal direction (accordingly, the plano-parallel plate was rotated around its vertical axis for that purpose) and observing the temporal shifts in the TOF detection mode. The O_2^+ signal was very convenient in these studies, since it produces a single narrow peak, whereas the time resolution of the system[1] did not allow to distinguish sufficient structure in the O^+ signal. Otherwise, the experiments were performed similar to the radial focusing tests and for the same $\{L_0, L_1\}$ and V_L combinations.

In all cases the agreement between the experimentally found V_1 values and the values obtained by numerical optimizations (see section 5) was excellent, with the deviations being well below 1 %. The central TOF values were also in $\lesssim$1 % agreement with the simulations. Accurate TOF stretching measurements were not possible due to the limited time resolution, but no deviations from the predictions were observed either. Therefore, it was concluded that the simulations yield reliable optimal conditions for both radial and TOF focusing in all modes of operation and also

[1] Several nanoseconds, determined mostly by the laser pulse duration and to a smaller extent by the electrical detection bandwidth.

satisfactorily predict the TOF properties.

A few velocity map images of O^+ were taken at selected ion optics parameters to test the actual operation in VMI and SVMI modes. One of the settings tested the operation without the additional lens, and the other — with it. Due to the "large" mass of the O^+ ion (in comparison to that of H^+) the TOF stretching was sufficient in both cases, so that the ~5 ns slice was thin (~6 %) in one case and even thinner ($\lesssim$4 %) in the other. "Regular" full-projection velocity map images were also taken at the same conditions for comparison.

The resulting raw images are presented in figure 29. The data were collected for ~100 000 laser shots (~3 hours) for each full-projection image and for ~70 000 laser shots (~2 hours) for their sliced counterparts. It should be noted that the experimental conditions (molecular beam parameters and the laser power) were not exactly the same for each of the experiments and even varied slightly during the measurements. Therefore, the integrated intensities of the images should not be compared quantitatively. Moreover, due to the multiphoton nature of the involved processes and competition among different channels leading to O^+ products the intensity distributions within each image are very sensitive to the used laser power and thus differ between the experiments.[1] Nevertheless, the overall structure of the kinetic energy spectrum does not depend on these variations and can be compared.

Figure 30 shows the kinetic energy distributions obtained from the sliced images. The raw images were rectified, and the intensity distributions were integrated over the polar angles (with the appropriate weighting factor) to obtain radial distributions. The results were converted to KE distributions using videocamera calibration (pixels $\mapsto$ physical dimensions) and SIMION simulations (radii $\mapsto$ kinetic energies). As can be seen from the figure, in both cases this procedure yielded KEs in good agreement with the predicted peak positions. Since the fine structure[2] cannot be fully resolved, it is difficult to make a precise conclusion about the discrepancies, but they definitely do not exceed the observed peak halfwidths[3] and can be estimated to

[1] In addition, the images in figure 29 are shown with enhanced contrast for better demonstration of the structured features. That is, their visual intensities should not be relied upon.

[2] The ground electronic term $2s^2 2p^4\ ^3P_J$ of O atom is split into three sublevels with energies 0, 20, and 28 meV (0, 158 and 227 cm^{-1}) for $J = 2$, 1 and 0 respectively [37]. The splitting for each of the excited terms $2s^2 2p^3(^4S^\circ)3p\ ^5P_J$ and $\ldots 3p\ ^3P_J$ does not exceed ± 3 cm^{-1} and can be neglected. All other participating terms are not split.

[3] One of the broadening mechanisms in addition to VMI focusing imperfections is the initial velocity distribution in the molecular beam. The assessment of ~50 m/s given on p. 12 and found not very

$L_0 = 50$ mm, $L_1 = 50$ mm, $V_0 = 3000$ V, $V_1 = 2117$ V, $V_\mathrm{L} = 0$
($\max K \approx 1.7$ eV, $\max \Delta\tau \approx 82$ ns):

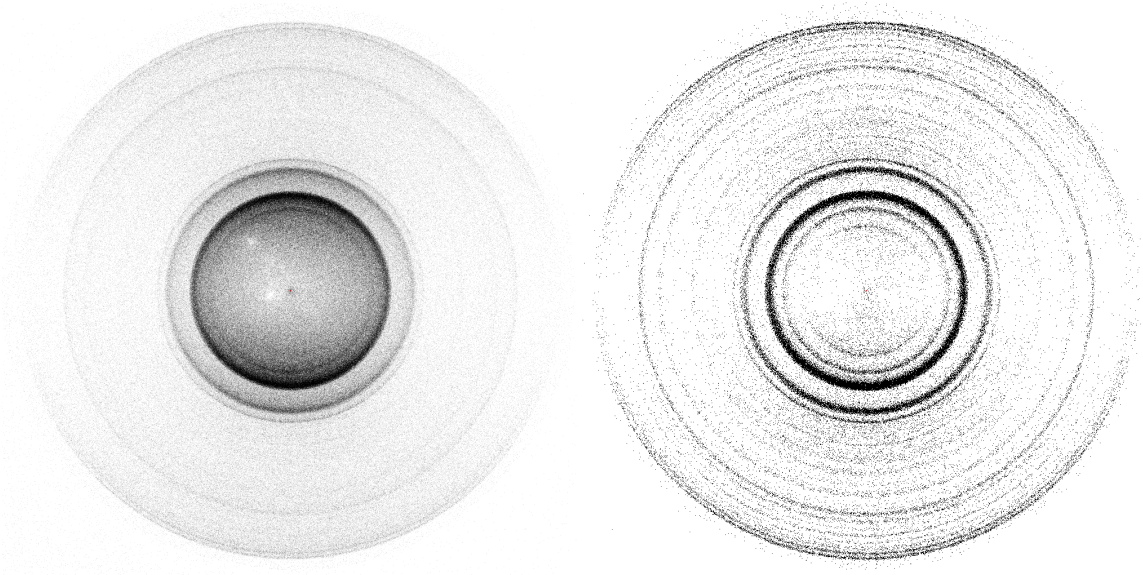

full projection (~1 000 000 events) central slice (~96 000 events)

$L_0 = 35$ mm, $L_1 = 60$ mm, $V_0 = 1500$ V, $V_1 = 1130$ V, $V_\mathrm{L} = -2400$ V
($\max K \approx 1.7$ eV, $\max \Delta\tau \approx 131$ ns):

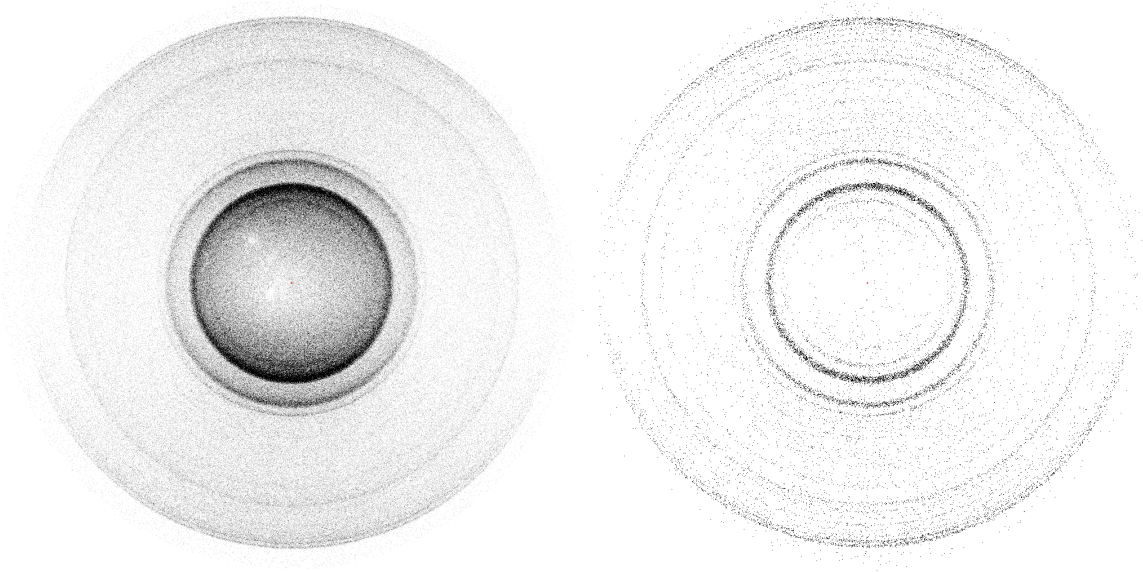

full projection (~630 000 events) central slice (~22 000 events)

Figure 29 Velocity map images of O^+ from O_2 photodissociation at $\nu = 44\,444$ cm^{-1} taken in two different ion optics regimes. (Raw event-counting data rendered at the native 1024 × 1024 px resolution is shown.)

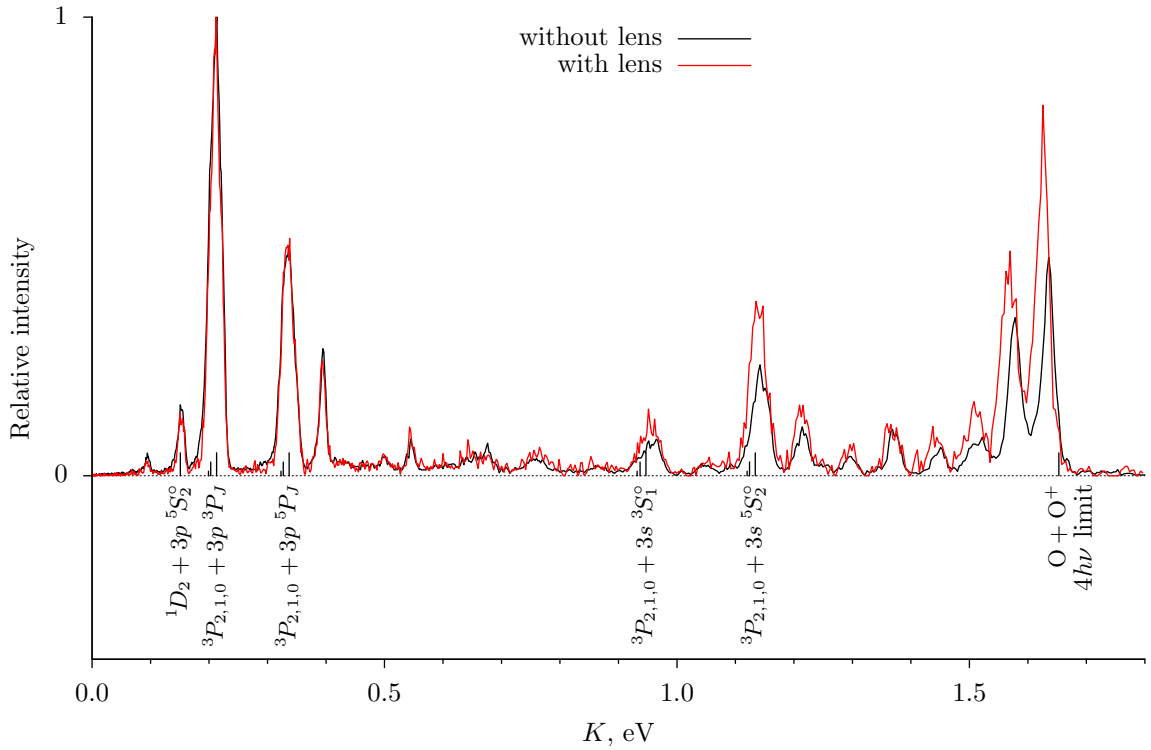

Figure 30 Kinetic energy distributions of O^+ extracted from sliced images shown in figure 29. Peaks due to 3-photon dissociation of neutral O_2 are marked according to atomic states of the two O fragments, other peaks correspond to O_2^+ dissociation.

lie within ~1 %. However, the raw images had radial distortions ~1.3 % for operation without the lens and ~1.9 % — with the lens, and the choice of the reference direction that must be made in the rectification process could lead to that much uncertainty in the speed transformation (and accordingly, up to ~3.5 % in the KE scale). In both studied cases the *horizontal* direction was found to give results consistent with the expectations and between each other, whereas the mentioned distortions corresponded mainly to various degrees of vertical shrinking of the images. The causes of this shrinking, which apparently depends on the ion optics parameters, remained unknown.

The two distributions plotted in figure 30 can serve as an illustration to the discussion on p. 74 about the relative slicing thickness and its effect of the resulting

important for H fragments becomes more critical for the heavier O fragments, constituting ~1.4 % of the speed for O with $K \approx 1.13$ eV and ~2.5 % for $K \approx 0.33$ eV (~2000 m/s). That is, this effect is likely to limit the final KE resolution regardless of the ion optics performance. In addition, the peaks corresponding to the 3*s* states are apparently overlapped by peaks from O_2^+ dissociation.

KE resolution. Comparison of the low-KE parts of the plots clearly shows that even for the peaks near $K \sim 0.1 \max K$, having relative slice thickness 5 ns/$\left(\sqrt{0.1} \cdot 82 \text{ ns}\right) \approx$ 19 % in the one case and 5 ns/$\left(\sqrt{0.1} \cdot 131 \text{ ns}\right) \approx 12\,\%$ in the other, the "wing" hardly stands out against the overall resolution and is not significantly affected by the appreciable (~1.6 times) variation of the relative slicing thickness. However, this situation holds as long as the slice thickness for the whole distribution remains reasonable. For example, at ~30 % slicing of the whole KE range the central part of the "sliced" image would effectively look like that of the full-projection image (left side of figure 29) with the sharp structure completely washed out. On the other hand, the signal-to-noise ratio drops for thinner slicing, and from that point of view the ~6 % slice is definitely better than the $\lesssim$4 % one, which is also evident from figures 29 and 30.[1]

7.2 Using H^+ from HBr and H_2S

The slicing performance for H^+ ions was tested mostly with HBr photodissociation. Although the same laser as in the O_2 experiments ($\nu = 44444$ cm^{-1}) was used for HBr excitation, the H fragments cannot be ionized by this radiation, and an additional separate "H-detection" arrangement was employed.[2] It consists of a laser producing tunable radiation near $\nu = 27420$ cm^{-1} ($\lambda_{\text{vac}} = 364.7$ mn) and a Kr/Ar tripling cell attached to the vacuum chamber for production of radiation near the Ly-α line ($2s \leftarrow 1s$ transition of H atom, $\nu = 82259$ cm^{-1}). This frequency-tripled VUV radiation passes to the vacuum chamber through a MgF_2 lens[3] and excites the H atoms to the $2p$ state. The unconverted part of the fundamental UV radiation then ionizes the excited atoms: $H(2p) \xrightarrow{h\nu} H^+ + e^-$. Since the energy difference between H^+ and $H(2p)$ is exactly 1/3 of the difference between the $2p$ and the ground $1s$ states of H, the ionization produces no recoil, and the formed H^+ ions inherit the velocity distribution of

[1] Strictly speaking, the intensity of the image taken with the additional lens is lower than what should be expected from the TOF stretching considerations. This is partly due to the different experimental conditions, as mentioned above, and partly because of lower detection efficiency for ions accelerated by the lower electric potential. Nevertheless, the point is that reduction of the signal level without noticeable improvement of the resolution makes identification of the signal structure more difficult, and this is well illustrated by the figures.

[2] This arrangements is in fact used for H fragment ionization in all actual experiments and thus was incorporated in the original apparatus. Its description can be found in [13].

[3] Also serving as a window separating the gas-filled cell from the vacuum chamber.

the H fragments without additional broadening.[1] Unlike the O_2 experiments, where O^+ was produced by O_2^+ dissociation or nonresonant ionization, the $1+1'$ REMPI of H is possible only in a relatively narrow frequency range. Moreover, the small mass of H atoms means that their velocity distribution has a large v_x spread (along the laser beam direction), and the resulting Doppler shifts of the resonant frequency exceed the bandwidth of the employed laser even for $K \ll 1$ eV. That is, frequency scanning of the "detection" laser over the whole Doppler profile is necessary for recording of the complete velocity distribution. Therefore, all H^+ images in this subsection were taken with the detection laser continuously sweeping the required range multiple times during the imaging data acquisition (to reduce effects from possible drifts of the experimental conditions).

Figure 31 shows the results of two SVMI experiments, in which the same velocity distribution was recording using different ion optics modes. The first one involved operation without the additional lens, thus resembling the usual Eppink–Parker arrangement. The accelerator voltages were chosen to provide sufficient kinetic energy range, but the resulting TOF stretching of only 19 ns was too small for satisfactory slicing with the ~5 ns pulse. As can be seen from the recorded image and the extracted kinetic energy distribution, the resulting peaks have rather long wings on the lower-KE side, although the extent of the wings is still limited compared to the full-projection case.[2] The second mode involved operation with the additional lens, and the parameters were chosen to attain the TOF stretching of 50 ns for approximately the same KE range. The resulting image and the distribution extracted from

[1] In contrast, the broadening due to electron recoil is an important issue in another widely used H ionization scheme by $2+1$ REMPI at $\nu = 41\,130$ cm^{-1}, where the excess energy of $13\,710$ cm^{-1} (1.7 eV) must go into translational energy. Although the electron carries most of this energy, the H^+ velocity is changed by ~420 m/s, which is well above the resolution of VMI systems and thus either becomes a limiting factor or requires deconvolution of the measured distributions.

It should be noted that $3+1$ REMPI using the same $\nu = 27\,420$ cm^{-1} radiation without tripling is also possible (see, for example, [42]) but is a much less efficient process. For instance, without tripling no H^+ signal could be observed in the present setup at the usual UV laser pulse energies (~2…3 mJ). Production of pulses with significantly higher energy is associated with more experimental difficulties on the one hand and might have undesired consequences, since many studied organic radicals have 1- or 2-photon absorption in this UV region, on the other.

[2] The "kinetic energy distribution" plotted for the full projection is not a physically meaningful property. Instead, it is simply the recorded full-projection intensity distribution converted to the KE scale using the procedure that is valid only for distributions recorded by sufficiently thin slicing. The purpose of showing it with the sliced data is to illustrate the extreme case in the dependence of peak shapes on the slice thickness.

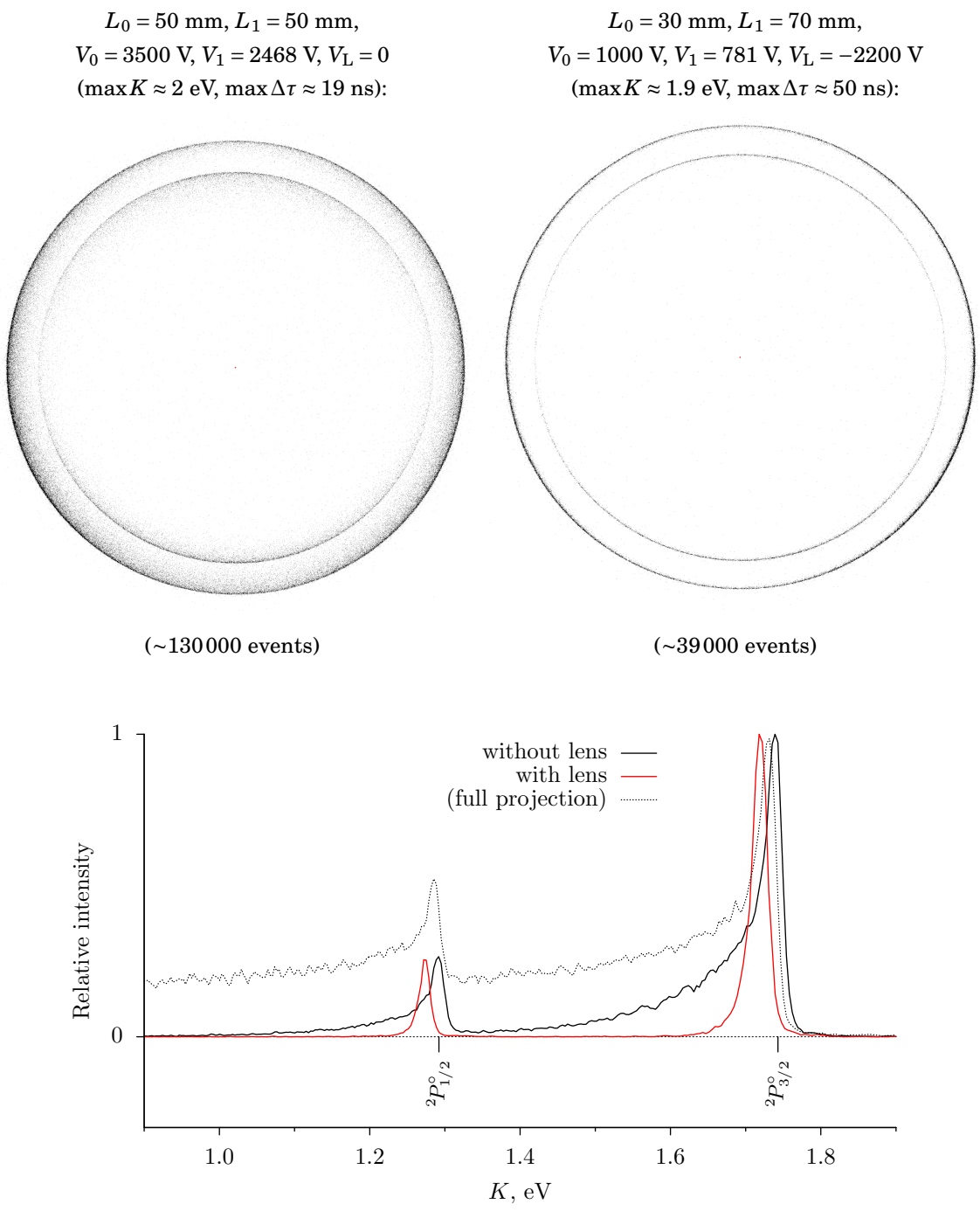

Figure 31 Sliced velocity map images of H^+ from HBr photodissociation at $\nu = 44444$ cm^{-1} taken at two different ion optics regimes. The plot shows kinetic energy distributions extracted from the images (peaks are marked according to the atomic states of the Br cofragment).

it evidently have much more localized peaks, with very small lower-KE wings. The halfwidths of the peaks are ~20 meV, that is ~1.2 % of the KE range, in good agreement with the worst-case $\Delta K = 1.45\,\%$ predicted by simulations. Unlike the O_2 images, rectification using the *vertical* reference direction (as plotted in figure 31) gave a better match of the absolute energies, although the discrepancies did not exceed ~1.5 % in KE with either direction for all H^+ images. Moreover, even the images (namely, the slice "without lens" and the "full projection") taken at supposedly the same experimental conditions show a small difference in the peak positions. This observation suggests that the discrepancies between the simulations and the experimental results come from small unaccounted variations of the experimental parameters, such as the voltages applied to the ion optics and the exact position of the ionization region.

Another SVMI test was carried out with H fragments from H_2S photodissociation at $\nu \approx 42\,560$ cm^{-1} ($\lambda \approx 235$ mn)[1] and using the same ion optics parameters as in the the HBr experiment with the additional lens. As mentioned above (p. 93), the velocity distribution produced in this process has close-lying peaks with extended rotational envelopes, resembling the distributions in the anticipated actual experiments. The experimental results are presented in figure 32 and show that the two peaks with ~47 meV (~2.5 % of max$K$) separation are indeed well resolved by the system. At the same time, the noticeable wings are caused by the rotational excitation of the SH cofragment. They are much longer than the wings due to the finite slice thickness (compare to the distribution obtained for monochromatic particles in the HBr experiment) and completely mask the effect of the latter.

Finally, figure 33 shows an example of operation in an extreme regime with max$K$ = 6.55 eV and $\Delta\tau_{\max K}$ = 58 ns (L_0 = 85 mm, L_1 = 30 mm, V_0 = 1900 V, V_1 = 886 V, V_L = −5000 V)[2]. In this image the H fragments with $K \sim 6$ eV produced

[1] This experiment was performed in process of preparations for the experiments on CH_2OH [43]. The laser wavelength was changed from the 225 nm used in the O_2 and HBr experiments, but not yet calibrated. Hence the "approximately equal" notation is used as a reminder. The lack of calibration prevents the quantitative comparison with the simulations, but the assessment based on the estimated uncertainty agrees well with results for all other cases.

[2] These characteristics correspond to $M = 58\ \mathrm{ns} \cdot \sqrt{6.55\ \mathrm{eV}} \sim 150\ \mathrm{ns}\sqrt{\mathrm{eV/Da}}$, which lies beyond the range plotted in figures 20, 22 and B.1–B.6. The parameters were selected to satisfy both radial and TOF focusing conditions (that is, the solution with minimal Δt was chosen from the Pareto set) and should lead to $\Delta K = 3.3\,\%$, $\Delta t = 0.65$ ns (~1.1 %) and $\Delta t_0 = 4$ ns (~7 %) according to the simulations. While this combination is not optimal from the SVMI perspective, it is in line with the conditions used for figure 31, which were also chosen to satisfy the TOF focusing, and provides an example

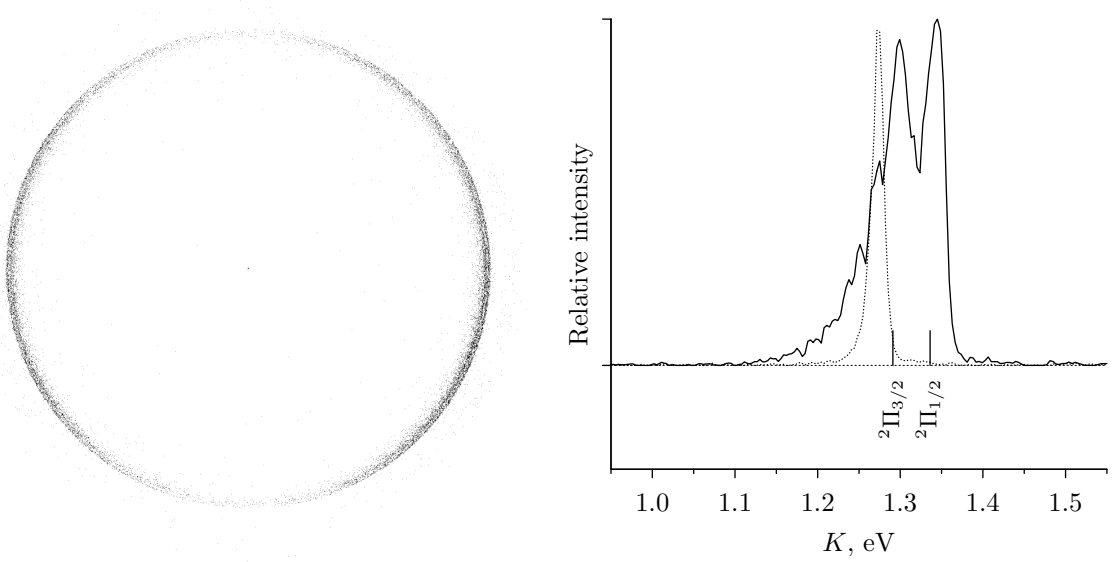

Figure 32 Sliced velocity map image and extracted kinetic energy distribution of H^+ from H_2S photodissociation at $\nu \approx 42560$ cm^{-1}. HS cofragment electronic states are indicated in the plot. (Dotted line shows distribution from the HBr experiment for comparison.)

by HBr photodissociation by Ly-α radiation from the H-detection laser can be seen in addition to the $K < 2$ eV fragments. In contrast to the full inner rings corresponding to dissociation by the $\nu = 44444$ cm^{-1} laser, only a small part of the outer ring is visible. The cause of this deficiency is that the efficient production of the VUV radiation requires phase-matching conditions in the tripling cell, which are satisfied only in a limited frequency range. While the H REMPI needs only one VUV photon, the production and detection of the ~6 eV H fragments requires two VUV photons and is therefore much more sensitive to the VUV intensity. Hence, even though the tripling efficiency is sufficient for H detection over the Doppler profile,[1] the intensity outside the phase-matching resonance cannot produce a detectable photodissociation signal. At the same time, the fragments produced at the peak efficiency can be ionized only if their v_x velocity component does not lead to Doppler detuning. As a consequence, only a small fraction of the high-KE fragments was observed in the experiment. The high-KE fragments correlated with Br in the ground state were not detected at all, either due to the Br*/Br branching ratio significantly shifted towards Br* or strong

of another kind of L_0/L_1 combination (namely, "long/short" in addition to "medium/medium" and "short/long").

[1]The resonant $2p \leftarrow 1s$ transition of H atom is very strong and was probably almost saturated in this experiment.

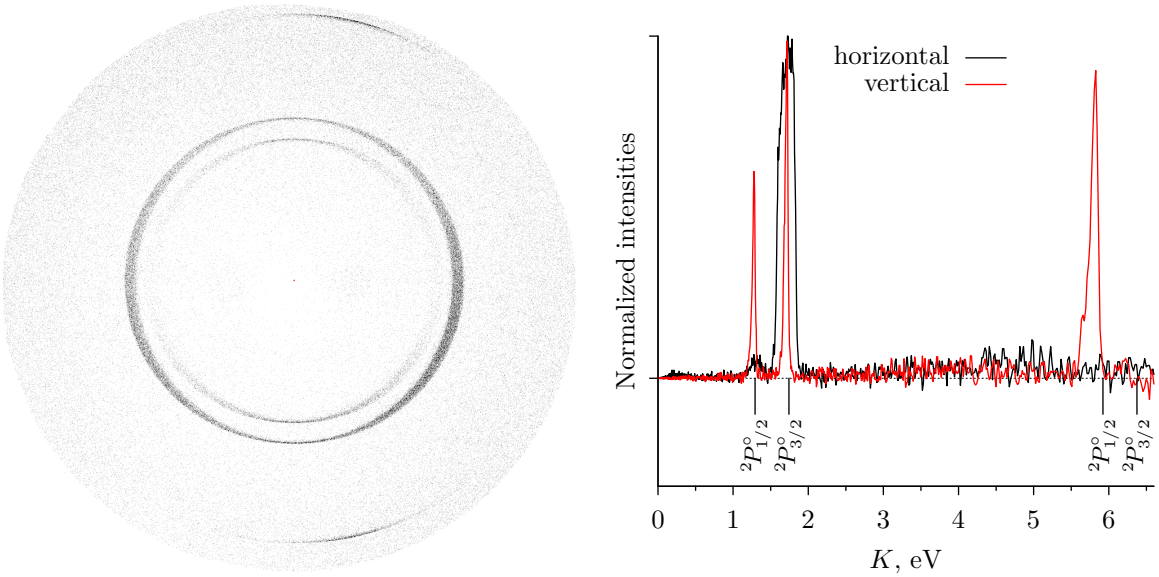

Figure 33 Sliced velocity map image of H^+ from HBr photodissociation at $\nu = 44444$ cm^{-1} and $\nu = 82260$ cm^{-1} (near Ly-α). Plotted kinetic energy distributions were extracted separately from the horizontal and vertical parts of the image (within 45° sectors), and background was subtracted.

perpendicular anisotropy of the Br($^2P_{3/2}$) channel at this high photon energy.[1]

Nevertheless, the kinetic energy distribution extracted from the available part of the image shows that the simulations are again in good agreement with the experiment, reproducing KEs with ~1.8 % accuracy. The inner rings also vividly illustrate the anisotropic (horizontal) broadening due to imperfect radial focusing and the vertically thin but horizontally elongated ionization region. For a more qualitative examination of this effect the kinetic energy distribution was calculated based only on the vertical (using the $(0 \pm 22.5)°$ and $(180 \pm 22.5)°$ sectors) and only on the horizontal (using the $(90 \pm 22.5)°$ and $(270 \pm 22.5)°$ sectors)[2] parts of the image, and the results are shown for compared in figure 33. The "horizontal" distribution has peaks broadened by ~0.24 eV, which is in good agreement with the predicted worst-case resolution (0.22 eV), whereas the "vertical" distribution has much narrower peaks.

[1] Unfortunately, no experimental data on HBr dissociation at these high photon energies was found in the literature. The published theoretical investigations are also not conclusive and usually do not go beyond ~75000 cm^{-1}, since the absorption cross-section drops quickly at high energies. Nevertheless, the available information allows to expect that the Br($^2P_{3/2}$) channel indeed has a strong perpendicular anisotropy over the whole energy range, and the Br*/Br branching ratio, according to [44], might be quite large.

[2] Polar angles are measured from the positive direction of the y axis, see figure 1.

Although the horizontal part of the outer rings is not present in the recorded image, their horizontal broadening is expected to be comparable to the vertical one, since the ion optics parameters were optimized mostly for focusing of the high-KE part of the distribution, as explained in subsection 5.3.

A striking difference of the image shown in figure 33 from all other images presented in this section is the presence of a nearly uniform background over the whole detector area. This background was observed even when no ions were generated by the lasers, and its source was traced to the high negative voltage applied to the additional lens. The study of this effect revealed that the background starts appearing at $V_{\mathrm{L}} \sim -2500$ V, and its intensity quickly increases with the lens voltage,[1] however, no background is observed at any positive voltages. The strong dependence of the intensity on the voltage and independence on other experimental conditions suggest that the background is due to electrons created at the central element of the additional lens by field emission and/or field ionization of the residual gas in the vacuum chamber and accelerated by the large potential difference between the electrode and the detector. This unfortunate circumstance means that in actual experiments, unless the signal is strong and structured enough to be confidently separable from the background, the working lens voltage is limited by $-2500 \ldots -3000$ V, and thus the achievable maximum imaged KE range also has an upper limit unrelated to the ion optics aberrations.

7.3 Position mapping mode

The dependence of the arrival positions of the particles on their initial positions is very undesirable in VMI operation, since it decreases the achievable velocity resolution for spatially extended ionization regions. However, this dependence can be put to good use, namely, for *imaging* (now in the optical sense) of the ionization region shape and position. The experimental diagnostics of these characteristics might be useful for optimization of the overlap between the laser and the molecular beam, and among different lasers in multi-laser experiments, as well as for alignment of the molecular beam relative to the ion optics.

This kind of imaging is similar to electron microscopy and requires operation in

[1] The intensity at $V_{\mathrm{L}} = -5000$ V was so high that it overwhelmed all useful signals in the "regular" VMI mode with ~100 ns mass-gate detection pulse and saturated the MCP detector in the TOF mass-spectrometer mode.

"position mapping mode" with initial positions mapped to arrival positions, desirably, regardless of the initial velocities. These requirements are in some sense opposite to the VMI requirements and therefore lead to significantly different ion optics designs and operating conditions. Electron microscopes, for example, use much more compact optics (at a few-millimeter scale) near the object and much higher voltages (a few tens of kilovolts). Nevertheless, the first electrostatic electron microscope (see figure 6 in [19]) had a simple lens system consisting of two apertures, very similar to the accelerator of the present VMI setup, and used moderate voltages, but still offered resolution at the micrometer scale. Therefore, there is a hope that even the existing VMI accelerator, designed without the microscopy applications in mind, might be configured for a reasonable performance in position mapping.

SIMION simulations and experimental tests showed that although for particles with $K \sim 1$ eV satisfactory velocity-independent focusing cannot be achieved at practically allowable accelerator voltages, the spread due to initial velocities can be reduced significantly and made a few times smaller than the size of the ionization region image. That is, the spatial parameters can be measured at least qualitatively. At the same time, the blurring for ions formed without appreciable kinetic energy[1] is negligible, which allows qualitative measurements even with the achievable performance. Among the studied configurations suitable for position mapping, one is particularly convenient from a practical point of view: $L_0 = 30$ mm, $L_1 = 60$ mm, $V_0 = V_1$, $V_\mathrm{L} = 0$. The $V_0 = V_1$ condition can be easily achieved by disconnecting the V_0 voltage supply from the voltage divider. The position mapping does not depend on the absolute value of the single applied voltage, but the blurring decreases and the detection efficiency increases at higher acceleration voltages, so it is advisable to apply the highest allowable voltage to the V_1 input.

Figure 34 shows an example of operation in the position mapping mode with $V_0 = V_1 = 2000$ V for O_2^+ ions produced by photoionization of O_2 (see subsection 7.1). The images were taken with the laser beam displaced vertically by ~1.7 mm from the central position (using the arrangement shown in figure 28) and its focal point moved by ~2 mm along the beam direction (by moving the focusing lens). Figure 35 shows results obtained in the same way, but for O^+ ions. It is evident that the O_2^+ images provide very sharp pictures of the ionization region,[2] although even for the

[1] Such as O_2^+ in the O_2 experiment, or ionization of H atoms present in the molecular beam or as a background in the vacuum chamber.

[2] The blurring seen near the focus of the laser beam is probably caused by space charge effects. Since

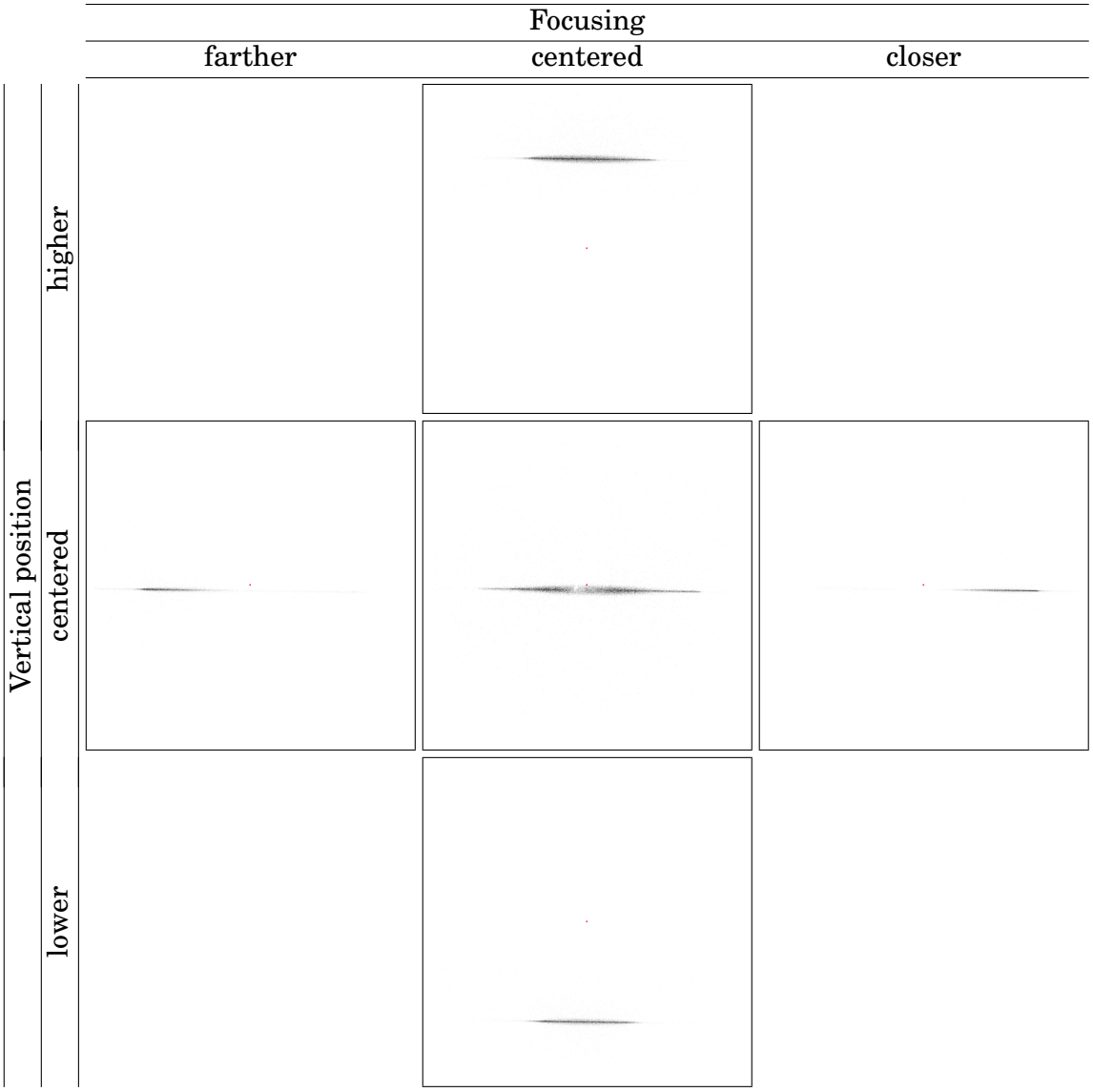

Figure 34 Images of the ionization region at various positions of the laser beam focus relative to the molecular beam recorded using O_2^+ ions.

the electrons formed in the ionization process have enough kinetic energy to leave the ionization volume and do so quickly due to their small mass, the remaining system of N ions acquires electrostatic energy $\sum_{\substack{i=1,\\ j>i}}^{N} \frac{q^2}{r_{ij}}$, where q is the electric charge, and r_{ij} are the initial distances between the ions. This energy is eventually converted to additional kinetic energies of the ions, resulting in $\sim Nq^2/\langle r\rangle$ KE change per ion, where $\langle r\rangle$ is the average inter-ion distance (comparable to the laser beam diameter). The effect must be stronger near the laser beam focus, where the ionization region radius is smaller, and the produced ion density is larger (due to higher energy density and multiphoton nature of the ionization), which agrees with the observed behavior.

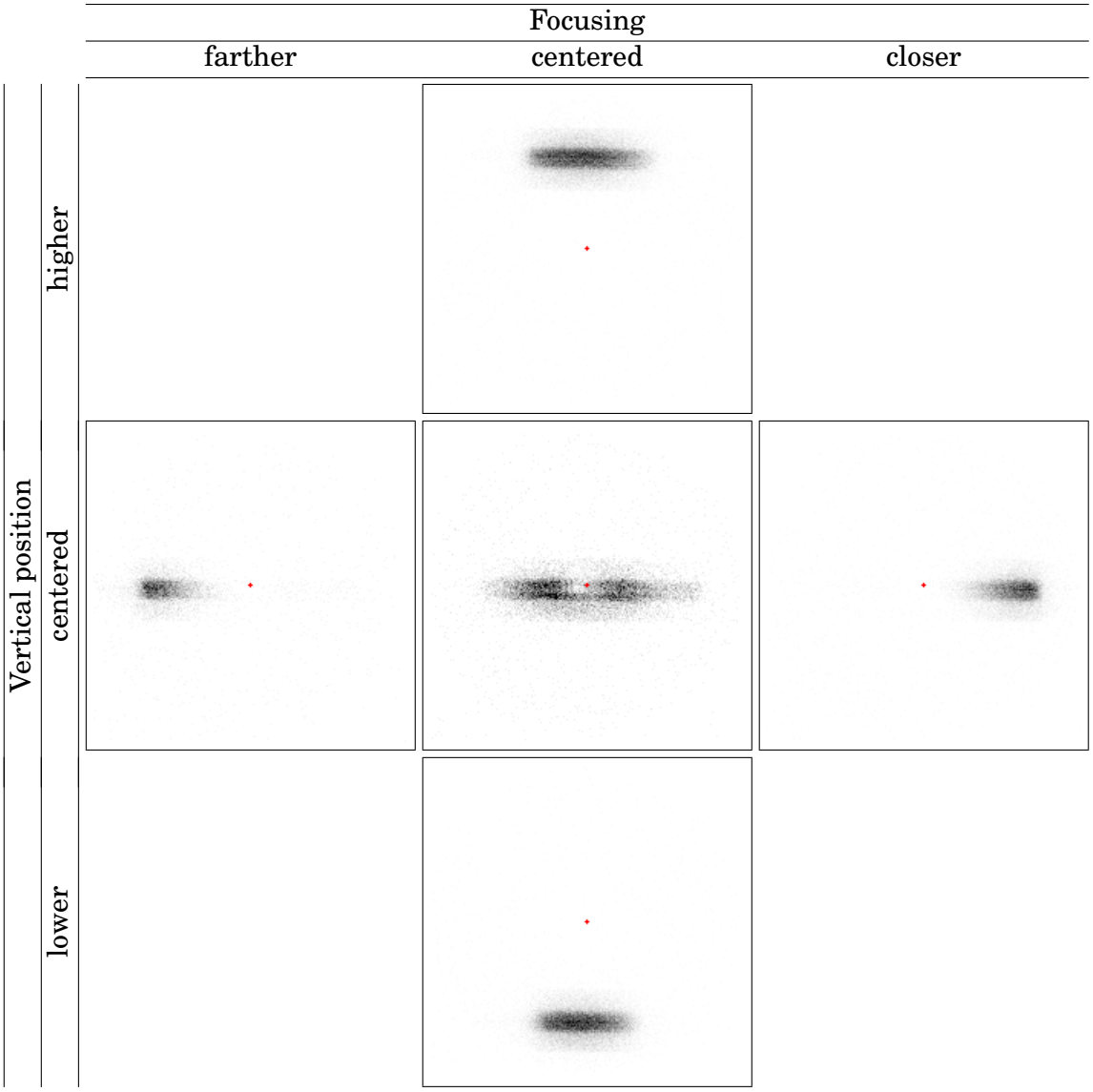

Figure 35 Images of the ionization region at various positions of the laser beam focus relative to the molecular beam recorded using O^+ ions.

O^+ ions with $K \sim 0.2 \ldots 0.4$ eV (the most intense part) the KE blurring does not mask the initial position information.

The molecular beam shape at $z \approx 0$ can be measured by vertical scanning of the ionizing laser beam (or using a sufficiently wide beam in case of 1-photon ionization), as demonstrated in figure 36. This image was obtained by monitoring O_2^+ ions and shifting the laser beam vertically by rotating the plano-parallel plate (see figure 28) in ~5° steps. The nonlinearity in (88) led to nonuniform sampling in terms of verti-

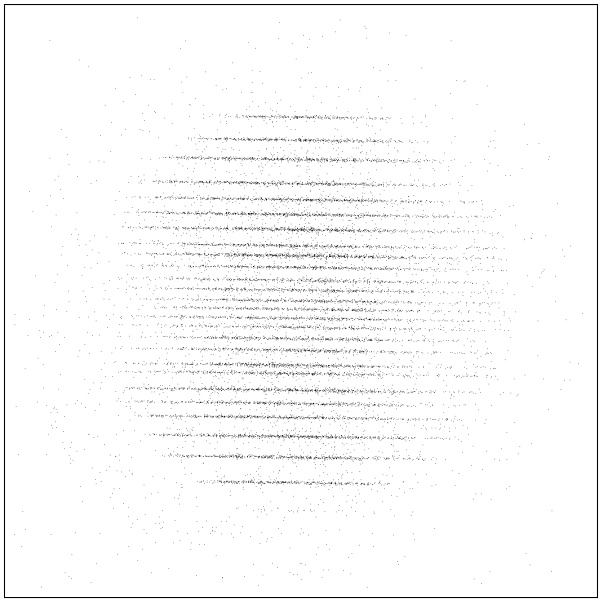

Figure 36 "Raster" image of the molecular beam (using O_2^+ ions) obtained by vertical scanning of the laser beam. (Compare to figure 4a in [7].)

cal positions, but the displacements can be easily calculated, and the fitting of the measured positions to the calculated beam displacements yields 182 px/mm (that is, 5.5 µm/px) scaling factor for the native 1024×1024 px imaging resolution. Therefore, the maximum molecular beam diameter determined from this image is ~3.8 mm, which indicates that the ⌀3 mm orifice in the terminating plate of the accelerator (see figure 14 and p. 80) was acting as the limiting factor in this experiment.[1]

The 5.5 µm/px imaging sensitivity and the ability to determine the positions with ~1 px resolution (even in presence of blurring, by finding the center of the produced symmetric intensity distribution) mean that the laser beams can be aligned with precision comparable to their focused diameters. The limitation of the method is that the laser beam being aligned must produce at least some ions. It is desirable that ions of the same mass, or similar masses,[2] are used for alignment of all beams, since in presence of stray magnetic fields trajectories of ions of different masses are deflected differently. Nevertheless, this deflection is relatively small,[3] and the obtained accu-

[1] This result could be expected from simple geometrical considerations: the ⌀1 mm skimmer located at ~1 cm from the nozzle outlet provides only very rough collimation. A later visual inspection of the system also showed a spot a few millimeters in diameter left by the molecular beam on the plate around the orifice.

[2] They are not required to be the ions on which the VMI measurements will be done.

[3] Trajectories of H^+ ions accelerated by 2 kV have curvature radius $r_g = mv/qB \sim 130$ m due to the

racy is usually better than the accuracy achievable by regular measurements outside the vacuum system (especially with the attached tripling cell).

Although the 2-dimensional images provide information only about the distribution along the x and y axes, the information related to the z axis displacements can be obtained from the TOF measurements, since the TOF focusing is also absent in this mode of operation, and thus the overall TOF depends on the initial positions of the ions. These measurements, however, are much less precise due to the inherently limited time resolution of the system.[1]

It should be noted that the possible applications of the "position mapping" discussed in this subsection were already mentioned in the first article [7] about the VMI method by Eppink and Parker. However, they described it merely as an "out of focus" operation of the VMI setup and gave only examples for O_2^+ ions without initial kinetic energies, making no attempt to optimize the operating conditions to better suit the position mapping requirements. As far as I know, since then the influence of initial positions of the particles on their arrival positions in VMI experiments was considered rather as a curious effect of imperfect focusing and a resolution-decreasing annoyance, than as an opportunity for diagnostics and optimization of experimental conditions.

7.4 TOF-MS operation

Testing of the mass-spectrometer mode was not performed during the experimental characterization described in this section. However, for the sake of completeness, an example of a relatively rich mass spectrum from a later experiment with organic radicals is provided here. Figure 37 shows the TOF signal recorded using ion optics parameters $L_0 = 50$ mm, $L_1 = 50$ mm, $V_0 = 3000$ V, $V_0 = 2115$ V, $V_\mathrm{L} = 0$ and converted to the ion mass scale according to (16). The experiment was devoted to studies of the CH_2OH radical, hence the molecular beam contained these radicals as well as unre-

Earth's magnetic field in the worst case. The deflection at the detector after 0.6 m flight path therefore should not exceed ~1.5 mm, or ~35 px. Heavier particles are affected even less.

[1] Moreover, the $V_0 = V_1$ regime leads to a relatively low electric field strength at the ionization region, and hence, according to (35), a significant TOF spread for particles with nonzero initial kinetic energies. For example, in the O^+ experiment (figure 35) the spread for $K_0 \sim 0.4$ eV ions was $\Delta\tau_{K_0} \approx 150$ ns, whereas the TOF sensitivity was only about 55 ns/mm. It means that if accurate position determinations from TOF measurements are required, then more favorable ion optics parameters must be considered. As the usability of these measurements with the given time resolution (see p. 12) was questionable, no optimizations for this task were performed in the present work.

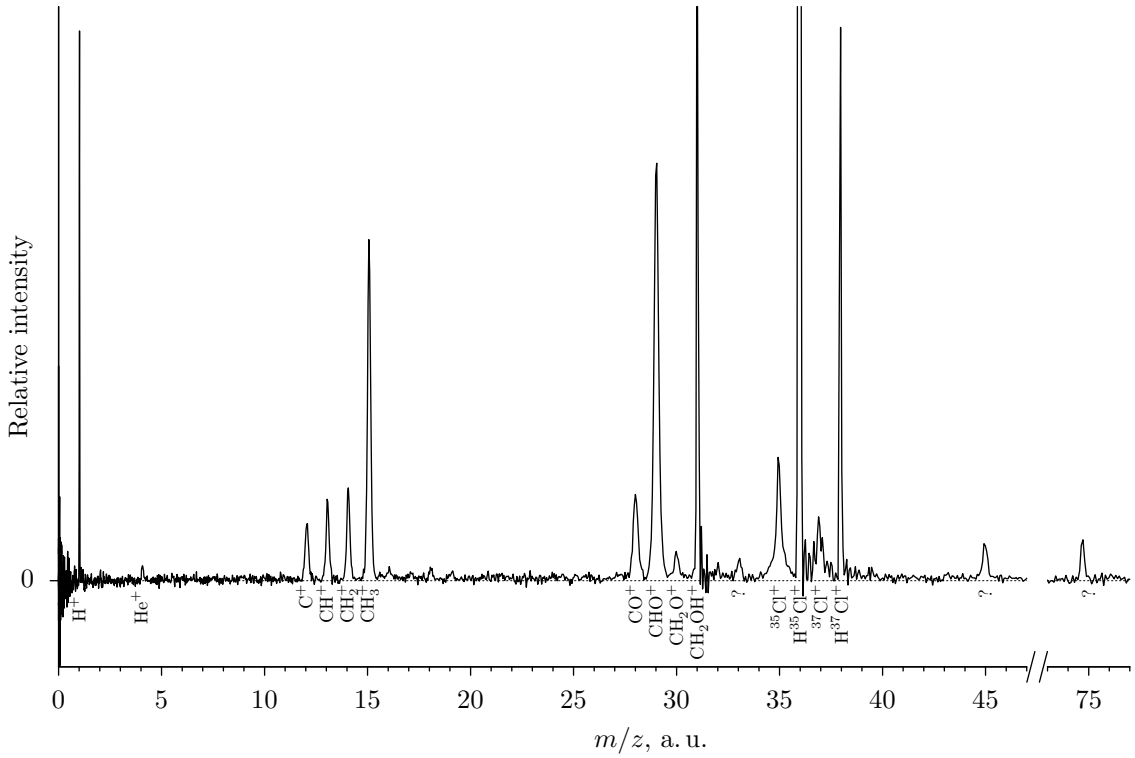

Figure 37 Example of mass spectrum (from CH_2OH studies). Some identified ions are marked under the peaks.

acted precursor molecules CH_3OH and Cl_2, and intermediate Cl atoms together with HCl and H byproducts, all without appreciable kinetic energy. The $\nu \sim 42\,700$ cm^{-1} radiation used for REMPI of CH_2OH was also resonant for HCl and near-resonant for Cl. In addition to "direct" ionization, it also dissociated all present polyatomic species and ionized the fragments, resulting in the observed $COH^+_{n=0\ldots2}$ and $CH^+_{n=0\ldots3}$ progressions of ions with various kinetic energies.

As can be seen from the plot, all observed masses were completely resolved. The ions without kinetic energy produced narrow peaks, whereas for other ions the peaks were broadened to various degrees. The case of Cl^+ is particularly interesting, since its peak[1] had a complex shape and the greatest width. The shape is determined by contributions from different types of Cl atoms prior to ionization. First, some Cl atoms with practically no kinetic energy are present in the molecular beam initially.

[1]Both $^{35}Cl^+$ and $^{37}Cl^+$ isotopes behave similarly, but the $^{37}Cl^+$ signal has ~3 times lower intensity (due to the lower natural abundance of ^{37}Cl) and is contaminated with the electrical ringing produced by the preceding strong and sharp $H^{35}Cl^+$ signal. Therefore, only the $^{35}Cl^+$ signal will be discussed.

They give the central sharp part of the peak. Second, Cl atoms might be produced by Cl_2 or HCl photodissociation. While the 1-photon energy is in principle sufficient to dissociate both Cl_2 and HCl,[1] the additional broader part of the peak was produced by resonant photodissociation of HCl, as revealed by scanning the laser frequency. The maximum observed width of the peak is consistent with 2-photon dissociation, which leads to Cl atoms with $K \approx 3.1$ eV: according to the SIMION simulations, the TOF spread for such fragments should be about ±80 ns, slightly less than the ~100 ns difference between the central arrival times of $H^{35}Cl^+$ and $^{35}Cl^+$. This example allows to make a conclusion that the mass resolution of 1 Da even for particles with relatively high kinetic energies is possible up to at least $m \sim 40$ Da.

Figure 38 shows another example of a mass-spectrum from the same experiment,

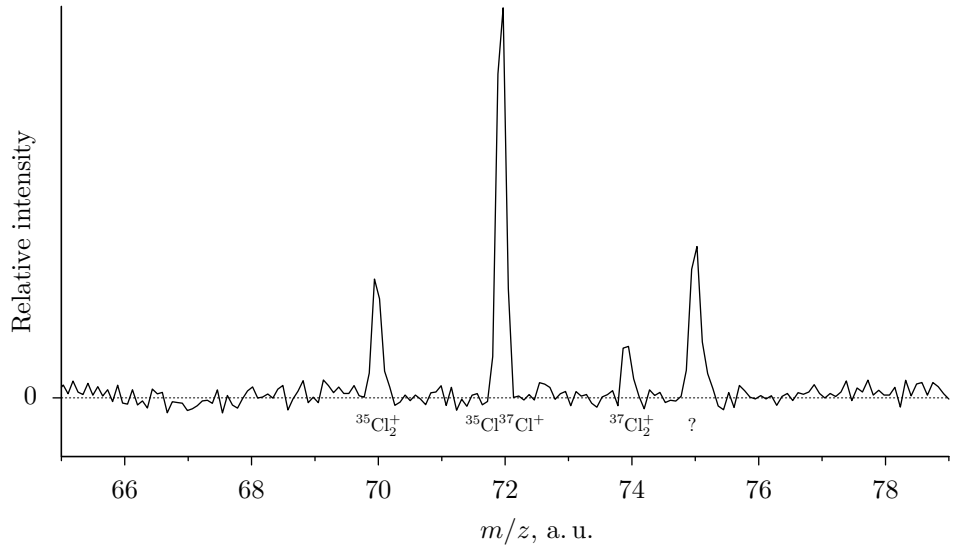

Figure 38 Example of mass spectrum in the region of higher masses.

but taken at $\nu \approx 42\,720$ cm^{-1} (one of the Cl atom REMPI frequencies),[2] clearly illustrating that for "cold" particles the mass resolution is significantly better even at

[1] $D_0(Cl_2) \approx 19\,990$ cm^{-1} [45], $D_0(HCl) \approx 35\,750$ cm^{-1} [46]. Both molecules have repulsive states correlating with ground state fragments, but the absorption cross-sections are actually very low near 42 700 cm^{-1}.

[2] The mass-spectrum part between 70 and 75 Da was very sensitive to the laser frequency and showed different combinations of 70, 72 and 74 Da peaks with various intensities. Although these peaks certainly correspond to the isotopomers of Cl_2, their relative intensities did not correlate with the expected abundances. The mechanism leading to this high ionization selectivity was unclear. Moreover, the 75 Da peak was always present in the spectra, sometimes alone, and could not be identified entirely.

higher masses. Although no particles heavier than 75 Da were observed in the conducted experiments, it is reasonable to expect that the resolving power of the system should be sufficient for all conceivable experiments on the existing apparatus.

8 Conclusion

The simulations and experimental tests described in the previous sections demonstrated that the designed and built SVMI system completely satisfies the demanded requirements (see section 2). Specifically, it is suitable for sliced velocity map imaging of H fragments with kinetic energies from a fraction of an electronvolt to a few electronvolts, providing kinetic energy resolution $\lesssim$2 % (and ~1 % for the range below ~2 eV).

The comparison of the experimental results with the results of numerical simulations indicated that the employed simulation framework provides a reliable description of the actual system performance. In particular, all parameters of the optimal operating conditions can be set based solely on the results obtained by optimization of the simulated performance. The predicted velocity mapping in that case does not differ from the actual one by more than 1 %, and therefore the kinetic energy calibration can be obtained with 1–2 % accuracy from the simulations alone. This fact greatly facilitates experimental studies in which such accuracy is sufficient, since it allows to choose the best conditions for each particular measurement without worrying about the issues with additional experimental calibration. On the other hand, if necessary, experimental recalibration can be also performed, although care must be taken to use as similar experimental conditions as possible if absolute KE accuracy $\lesssim$1 % is desired.

While the main intention of the developed ion-optical system was the application for VMI with sliced detection, its advanced temporal characteristics are potentially useful for 3-dimensional detection with time resolution as well. According to the simulations, a temporal resolution of the velocity mapping $\lesssim$1 % — in good concordance with the radial resolution — can be achieved for a very broad range of operating conditions. That is, the present ion-optical system provides extensive possibilities for independent adjustments of the radial and temporal extents of the particles cloud at the detector, which can be utilized for better matching of these characteristic with

the resolving capabilities of the detection system and therefore can help[1] to improve the resolution or enhance the range of 3-dimensional VMI setups.

9 Future work

Even though the present SVMI system showed good performance and usability during the tests and in subsequent experiments, some of which are described in [43], there is always a room for improvement. In addition, it would be desirable to correct the design and implementation flaws that led to the problems mentioned above. Several possible modifications of the system are summarized in this sections. The changes of the existing hardware required to implement them would range from none to a complete redesign.

The most obvious, and probably most important, revision is related to the parasite electron signal generated by the additional lens at high voltages (see p. 105). Since there are good indications that the electrons are generated near the surface of the central electrode due to a high local electric field strength, and such processes are known to be more efficient near surface roughnesses, careful polishing of the relevant surfaces might eliminate or at least considerably reduce the electron emission intensity. The most important surface is that of the lens ring (closest to the detector[2]) of the central element, but polishing of all other high-voltage parts and their immediate neighbors might be also necessary.[3]

The next set of possible modifications is related to the accelerator assembly. A close examination of the Pareto-optimal plots for the performance characteristics of the system (see figure 20) reveals that at high magnification indices $M \gtrsim 80\ \mathrm{ns}\sqrt{\mathrm{eV/Da}}$ (that is, for high imaged KE ranges or large TOF stretchings) all optimal parameters require the use of the whole available length of the accelerator. (For better visualization the data from figure 20 are replotted in figure 39 in terms of the total length $L_\mathrm{a} \equiv L_0 + L_1$.) This situations contrasts with the diversity seen at lower M values and suggests that a longer accelerator could lead to somewhat

[1] Although the present system was designed with relatively specific goals in mind and might be not optimal for other uses, I hope that the ideas described in this work will help in optimal design of similar systems for other specific cases.

[2] Electrons emitted from the farthest ring are accelerated in the opposite direction and thus should not reach the detector.

[3] At least, it will enhance the high-vacuum performance.

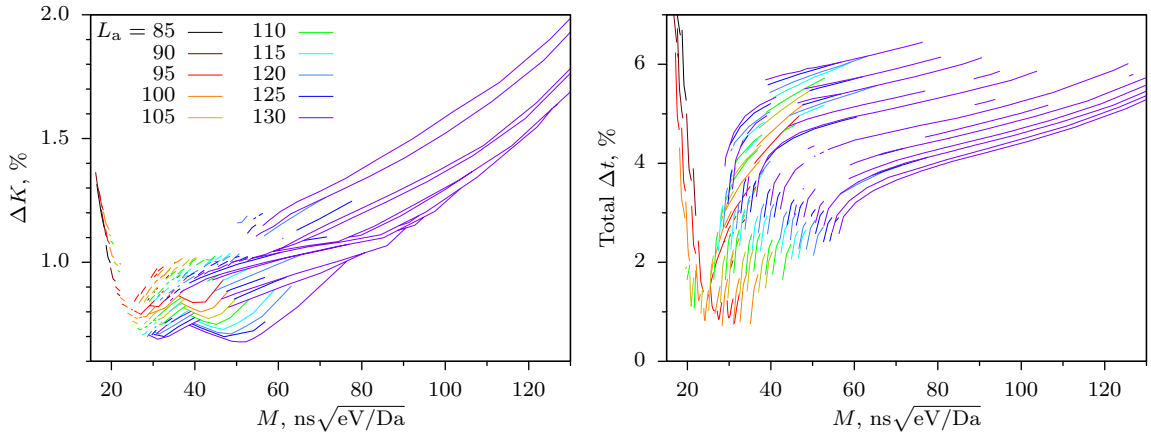

Figure 39 Dependence of Pareto-optimal performance characteristics on the total used length (in mm) of the accelerator.

better performance at high KE ranges by allowing a greater variety of conditions for the optimization. While only a minor improvement is expected (based of the overall behavior of the envelopes of the presented data), the possibility is worth checking by performing additional numerical simulations with more electrodes in the accelerator subsystem.

More complicated electric field configurations in the accelerator also deserve an extended study. The simplest extension of the two-region concept used throughout this work is to use three regions with different electric field strengths.[1] This will add two parameters (length L_2 and electric field strength E_2) to the optimization space, but since the available two-region results can be used as starting points, the complete optimization[2] seems doable. If it leads to a noticeable improvements in at least some of the performance characteristics, then the general configuration with independent voltages applied to all apertures should be studied as well. The large number of parameters would require a very different optimization approach. Perhaps, formulating a single optimization criterion in each particular case and starting one of the usual local minimization methods from the most suitable 2- or 3-region conditions would be the most practical approach. An appealing feature of these studies in regard to the

[1] Although many VMI setups used at present go beyond the basic Eppink–Parker arrangement and incorporate more than two apertures, the benefits of such designs were not quantified in the literature known to me.

[2] "Complete" in terms of the parameter space. Simultaneous optimization of many characteristics is impossible with any number of parameters (see p. 73), however, *all* characteristics optimized with more parameters can be *simultaneously better* than those optimized with less.

existing apparatus is that no modifications of the parts inside the vacuum chamber are required. The 3-region mode will need only one more voltage supply connected to the existing voltage divider. A practically usable implementation of the "general" case, however, must involve a computer-controlled version of a variable voltage divider (which is still a relatively simple electronic device).

The studies of more complicated fields could be combined with a more detailed study of the aperture radii. As described on p. 38, in the present work the radius was chosen mostly based on the performance without the additional lens. All apertures had the same radius, first, to limit the number of parameters in the geometry optimization, second, to facilitate manufacturing of the parts and assembly of the apparatus. Nevertheless, the "upper KE limit" example in figure 23 illustrates that the filling factor of the last apertures under operation in high-M regimes is very large, which might be the main source of the increased aberrations. Therefore, utilization of apertures of different radii, at least larger towards the exit end of the accelerator (especially if the accelerator is to be extended, as mentioned before), might improve the performance characteristics for operation with high KE ranges and high TOF stretchings.[1]

Another set of modifications concerns the additional lenses in the drift region or closer to the detector. As explained at the beginning of section 5, the present system was intentionally kept as simple as possible, and therefore only one additional unipotential lens was installed after the accelerator (see subsection 4.4). The simulations, however, showed that a very short unipotential lens performs worse than an extended one (see p. 78). Since the thick lens in principle has two different "refractive surfaces", a stack of shorter but weaker lenses (that is, the use of multiple refractive surfaces) might show a better performance than the single utilized lens. For example, the optimization of a double unipotential lens described in [30] did not converge to a single lens, which suggests that multielectrode compound lenses indeed have some advantages. The optimization applied to the present system may be organized as geometry optimization of a few electrodes, similar to the approach used in [30],[2] or employ the method that was used for the accelerator design and optimizations in the present work, with multiple fixed electrodes and variable voltages.

[1] Since regimes with moderate M values generally use shorter accelerator lengths (see figure 39), they should not be affected by increased radii of the "inactive" apertures.

[2] However, using independent voltages for all electrodes should be preferred over the configuration with multiple unipotential lenses with grounded intermediate electrodes.

In conjunction with a more complicated configuration of the additional lens, the requirement that the electrostatic potential at the exit of the accelerator is equal to the detector potential can be lifted. This can be done either by keeping the detector grounded and extending the first electrode of the additional lens to the accelerator exit (to prevent the grounded vacuum chamber walls from distorting the electric field) or by using an electrically biased detector. Besides providing more freedom for ion optics optimizations, the larger possible potential difference between the ionization region and the detector should lead to higher kinetic energies of the particles at the detector and hence to higher detection efficiency, which is especially important for operation near the lower KE limit, where the acceleration voltage is relatively small due to the requirement of low electric field strength in the accelerator region. Preliminary simulations showed that using a negative (for positive ions) bias of the detector in the present system is also very effective in reducing the image size, in accordance with the analysis given on p. 43, and requires lower voltages applied to the additional lens for similar resulting characteristics.[1] The main practical problem with the bias is that the employed detector encloses the MCP stack in a holder that has a complicated shape and exposes all electric potentials[2] near the detector input surface. In the present design a grounded electric shield covering these holder parts was sufficient to maintain a nearly field-free region around the detector, but creation of a well-behaved electric field configuration would require more careful design considerations and thus was not included in studies of the minimalistic system. Nevertheless, biased detectors are often used in TOF measurements,[3] for which the field distortions are less crucial, and there are no compelling reasons against improving the field geometry for VMI use.

The last part of this section is devoted to more fundamental considerations. Already in the early days of charged particle optics Scherzer has published his famous article [47] with the proofs that chromatic and spherical aberrations are unavoidable in systems with cylindrically symmetric time-independent electrostatic fields. While these theorems did not pose any particular limit on the aberrations, electron

[1] This fact is notable in connection with the problem of parasite electron emission (see p. 105 and 114). On the one hand, lower lens voltages should reduce the emission intensity, on the other — a significant negative potential of the detector should repel at least some of the produced electrons.

[2] Potentials applied to the front, middle and back of the MCP stack, as well as potentials of the phosphor screen and the (grounded) mounting vacuum flange.

[3] Mainly due to the convenience of operating the detector with grounded *output*.

microscopy — the main field of applications — has eventually reached a resolving power limit dictated by the aberrations in practically reasonable arrangements, and the study of methods to circumvent the troublesome theorems started to develop. The ideas included addition of optical elements without cylindrical symmetry ("multipoles"), alternating electric fields and combinations with magnetic lenses. A relatively recent theory for some of these methods for aberrations corrections can be found in [48]. Although not all of the achievements in electron microscopy are applicable to the VMI case, the possibility of using such ideas for improvement of VMI performance characteristics is definitely interesting.[1]

[1]Some attempts to use magnetic fields for VMI applications were already made. For example, in [49] the measured kinetic energy range was significantly increased by application of an axial magnetic field. (The electrostatic part in that case used Wiley–McLaren arrangement and actually did not provide radial focusing, however, this fact is not related to the magnetic field and does not diminish its utility. In principle, the use of magnetic field for beam collimation was already mentioned in the original article [3] by Wiley and McLaren, but due to the lack of position sensitivity in TOF detection, they were not concerned about the details of the radial velocity mapping, which were important in [49].)

Appendices

A Listings of input files for SIMION simulations

The following listings provide short descriptions and source codes of input files required for numerical simulations of the ion optics performance in SIMION 8. Important points specific to the problem are commented in the code, but the SIMION documentation should be consulted regarding the general information about the formats, semantics and how to use these files.

A.1 Geometry definition

Geometry of the electrodes (including grounded walls and holders) is defined as close as possible (within cylindrical symmetry) to the actual dimensions of the real setup. The resulting potential array must be refined in the "fast adjust" mode and inserted into the workbench using 0.5 mm/gu scale and -51 mm X-shift.

real.gem

```
1  ; This geometry file uses 0.5 mm grid.
2  ; All coordinates and sizes below are specified in millimeters,
3  ; and "locate(0,0,0,2)" sets the appropriate scaling.
4  ; The potential array size is defined accordingly.
5
6  pa_define(1370,152,1,cylindrical,y_mirror)
7  locate(0,0,0,2) {
8   ; vacuum chamber walls
9   electrode(0) {
10   fill {within{box(0,0,1,76)}      ; skimmer side wall
11         within{box(0,75,676,76)}   ; tube
12         within{box(684,0,685,76)}} ; MCP side wall
13  }
```

```
; accelerator
locate(25.5) {
 ; 1st ring
 locate(  0) {electrode( 0) {fill{within{box(-5,36.5,0,55.5)}
                                 within{box(0,51,14,55.5)}}}}
 ; 1st plate
 locate( 10) {electrode( 1) {fill{within{box(0,1.5,1,40)}}}}
 ; other plates
 locate( 20) {electrode( 2) {fill{within{box(0,20,1,40)}}}}
 locate( 30) {electrode( 3) {fill{within{box(0,20,1,40)}}}}
 locate( 40) {electrode( 4) {fill{within{box(0,20,1,40)}}}}
 locate( 50) {electrode( 5) {fill{within{box(0,20,1,40)}}}}
 locate( 60) {electrode( 6) {fill{within{box(0,20,1,40)}}}}
 locate( 70) {electrode( 7) {fill{within{box(0,20,1,40)}}}}
 locate( 80) {electrode( 8) {fill{within{box(0,20,1,40)}}}}
 locate( 90) {electrode( 9) {fill{within{box(0,20,1,40)}}}}
 locate(100) {electrode(10) {fill{within{box(0,20,1,40)}}}}
 locate(110) {electrode(11) {fill{within{box(0,20,1,40)}}}}
 locate(120) {electrode(12) {fill{within{box(0,20,1,40)}}}}
 locate(130) {electrode(13) {fill{within{box(0,20,1,40)}}}}
 locate(140) {electrode(14) {fill{within{box(0,20,1,40)}}}}
 ; 2nd ring
 locate(145) {electrode( 0) {fill{within{box(5,36.5,0,55.5)}
                                 within{box(0,51,-14,55.5)}}}}
}
; lens
locate(251.5) {
 ; 1st element
 locate(0)     {electrode(0)  {fill{within{box(0,60,19,69)}
                                   within{box(0,61,120.5,62)}
                                   within{box(101.5,60,120.5,69)}}}}
 ; middle element
 locate(131.5) {electrode(15) {fill{within{box(0,60,19,69)}
                                   within{box(0,61,120.5,62)}
                                   within{box(101.5,60,120.5,69)}}}}
 ; last element
 locate(263)   {electrode(0)  {fill{within{box(0,60,19,69)}
                                   within{box(0,61,120.5,62)}
                                   within{box(101.5,60,120.5,69)}}}}
}
; MCP end
locate(677.5) {
 electrode(0)  {fill{within{box(-22.5,51,22.5,76)}} ; reducer flange
                fill{within{box(-6,22,-7,51)}}}     ; MCP shield
 ; MCP (front only)
```

```
  electrode(16) {fill{within{box(0,0,1,32)}
                      within{box(0,24,-1,32)}}}
 }
}
```

A.2 Particles definition

Initial positions and velocities of the particles are defined for relatively uniform representation of the distribution. The mass and maximum kinetic energy are set to "unit" values (1 Da and 1 eV respectively) and are scaled according to the actual user settings by the program (see listing A.3)

real.fly2

```
--[[

Particle definitions for "real.lua" program.
3 * 4 * 5 = 60 protons are defined for all combinations of:
   3 kinetic energies: 1, 0.4, 0.1 eV,
   4 positions: (+-0.5 mm, +-1 mm),
   5 angles: 10, 50, 90, 130, 170 degrees.

Colors:    KE      x = -0.5      x = +0.5
          ----- --------------- ----------
           1.0   5 light red     1 red
           0.4   6 light green   2 green
           0.1   7 light blue    3 blue

--]]

particles {
  coordinates = 0,
  -- KE = 1
    standard_beam {
      ke = 1, color = 5,
      position = vector(-0.5, -1, 0), tob = 0,
      n = 5, az = 0, el = arithmetic_sequence {first = 10, step = 40},
      mass = 1.00727647, charge = 1,
    },
    standard_beam {
      ke = 1, color = 5,
      position = vector(-0.5, 1, 0), tob = 0,
```

```
29      n = 5, az = 0, el = arithmetic_sequence {first = 10, step = 40},
30      mass = 1.00727647, charge = 1,
31    },
32    standard_beam {
33      ke = 1, color = 1,
34      position = vector(0.5, -1, 0), tob = 0,
35      n = 5, az = 0, el = arithmetic_sequence {first = 10, step = 40},
36      mass = 1.00727647, charge = 1,
37    },
38    standard_beam {
39      ke = 1, color = 1,
40      position = vector(0.5, 1, 0), tob = 0,
41      n = 5, az = 0, el = arithmetic_sequence {first = 10, step = 40},
42      mass = 1.00727647, charge = 1,
43    },
44  -- KE = 0.4
45    standard_beam {
46      ke = 0.4, color = 6,
47      position = vector(-0.5, -1, 0), tob = 0,
48      n = 5, az = 0, el = arithmetic_sequence {first = 10, step = 40},
49      mass = 1.00727647, charge = 1,
50    },
51    standard_beam {
52      ke = 0.4, color = 6,
53      position = vector(-0.5, 1, 0), tob = 0,
54      n = 5, az = 0, el = arithmetic_sequence {first = 10, step = 40},
55      mass = 1.00727647, charge = 1,
56    },
57    standard_beam {
58      ke = 0.4, color = 2,
59      position = vector(0.5, -1, 0), tob = 0,
60      n = 5, az = 0, el = arithmetic_sequence {first = 10, step = 40},
61      mass = 1.00727647, charge = 1,
62    },
63    standard_beam {
64      ke = 0.4, color = 2,
65      position = vector(0.5, 1, 0), tob = 0,
66      n = 5, az = 0, el = arithmetic_sequence {first = 10, step = 40},
67      mass = 1.00727647, charge = 1,
68    },
69  -- KE = 0.1
70    standard_beam {
71      ke = 0.1, color = 7,
72      position = vector(-0.5, -1, 0), tob = 0,
73      n = 5, az = 0, el = arithmetic_sequence {first = 10, step = 40},
```

```
74        mass = 1.00727647, charge = 1,
75      },
76      standard_beam {
77        ke = 0.1, color = 7,
78        position = vector(-0.5, 1, 0), tob = 0,
79        n = 5, az = 0, el = arithmetic_sequence {first = 10, step = 40},
80        mass = 1.00727647, charge = 1,
81      },
82      standard_beam {
83        ke = 0.1, color = 3,
84        position = vector(0.5, -1, 0), tob = 0,
85        n = 5, az = 0, el = arithmetic_sequence {first = 10, step = 40},
86        mass = 1.00727647, charge = 1,
87      },
88      standard_beam {
89        ke = 0.1, color = 3,
90        position = vector(0.5, 1, 0), tob = 0,
91        n = 5, az = 0, el = arithmetic_sequence {first = 10, step = 40},
92        mass = 1.00727647, charge = 1,
93      },
94  }
```

A.3 Analysis and optimization program

This user-programming script performs low-level initialization of simulation parameters from user-defined high-level parameters, analysis of the simulation results and, possibly, optimization of some user parameters. It can be run in either interactive or batch mode.

The user-controlled parameters are defined as SIMION "adjustable variables" and can be set through the corresponding interface ("Variables" window). These parameters are:

- effective accelerator lengths L_0 and L_1 (in cm),
- effective accelerator voltages V_0 and V_1 (in V),
- lens voltage V_L (in V),
- maximum kinetic energy K_max in the sample (in eV),
- particle mass m (in Da),
- molecular beam velocity v_beam (in m/s).

A few other variables control the automatic optimization parameters:

- V_1 *step* — initial step size (in V) of V_1 variation for resolution optimization (zero

value disables the optimization);

- *K step* — initial step size (in eV) for maximum measurable $K_{\max}$ determination (zero value disables the determination);
- *batch* — nonzero value of this variable activates the batch mode, in which sets of the simulation parameters (L_0, L_1, V_0, V_1, V_L and $K_{\max}$) are read from the external file (`in.dat` placed in the working directory), and the optimization results for each set are recorded to another external file (`out.dat` in the same directory).

Other parameters that do not need to be changed during the ordinary use of the program (the detector radius, the number of plates in the accelerator and the structure of the particle distribution sample) are defined simply as local variables and are hidden from the interface but can be changed in the source code if adjustments to these properties are required.

There are 3 subroutines, which are called by SIMION at various moments during the simulation process and perform the actions necessary for the control and analysis:

1. `segment.initialize()` is called upon the "initialization" of each particle and scales its mass and initial velocity from the generic values according to the specified m and $K_{\max}$ (namely, the default mass 1 Da is multiplied by m, and the initial velocity vector (corresponding to the sample with $K_{\max} = 1$ eV at $m = 1$ Da) is multiplied by $\sqrt{K_{\max}/m}$). Additionally, if requested, it prepares the optimization process or recalls the values of the varied parameters from the previous optimization step.

2. `segment.init_p_values()` is called once after all particles were initialized and sets the potentials of all accelerator electrodes based on L_0, L_1, V_0 and V_1 according to the procedure described in subsection 5.1. The potential of the central element of the lens is also set to V_L.

3. `segment.terminate()` is called for each particle upon hitting an electrode (in normal operation — the detector) and collects the arrival times and radial positions. Upon "termination" of the last particle, when the data gathering is completed, these "raw" data are analyzed according to equations (74)–(80). A summary of the simulation parameters and the obtained results is printed to the "Log" window. If any optimization was enabled, the optimization state is updated, and, depending on whether the convergence is reached or not, either the optimization results are written to the output file, or a new simulation cycle is started. Also, when convergence is reached

in the batch mode, a new set of the simulation parameters is read from the input file, and a new optimization run is requested (see item 1).

In addition to these necessary actions the user program disables the display of particle trajectories during the optimization and enables it after the optimization is finished. The reason behind these operations is that while the trajectories are very helpful for visualization of the system operation, their display takes a considerable amount of time. Therefore, the display is disabled in order to speed up the optimization process and enabled only to show the final result.[1]

Warning! The program does not validate the settings and user's input. The user is responsible for providing sensible values for constants and adjustable variables.

real.lua

```
--[[

Analysis and parameter-optimization program.

(Requires electode definitions from "real.gem", patricle definitions from
"real.fly2" and the ionization region being located at the origin.)

Parameters are described below (see program code). Optimized parameters are:

   V1    if V1step > 0,
   Kmax  if Kstep > 0.

If "batch" is not 0, then file "in.dat" is opened, from each line there
parameters

   L0  L1  V0  V1  VL  Kmax

are read (must be separated by spaces or tabs), and the optimization results
are appended to file "out.dat" in format (separated by tabs)

L0    L1    V0    V1    VL    Kmax    DK    tave    Dt    tau    Dt0    Rmax

where DK [%]     is kinetic energy resultution,
```

[1] If drawing of equipotential contours is enabled in the interface, they are updated for each simulation cycle, which also takes noticeable time during optimizations. This behavior is not controlled by the program, however, the drawing can be easily disabled and enabled from the interface, even when the optimization process is active. Moreover, the optimized potentials are retained when the optimization finishes, so the corresponding contours can be plotted even afterwards (which is impossible for the trajectories).

```
24        tave [us]      average TOF,
25        Dt [ns]        TOF resolution,
26        tau [ns]       full TOF spread,
27        Dt0 [ns]       v_z = 0 slice distortion,
28        Rmax [mm]      radius for KE = Kmax
29                       (for convergency checks and calibration).
30
31  --]]
32
33  simion.workbench_program()
34
35  adjustable L0 = 5     -- initial length [cm]
36  adjustable L1 = 5     -- secondary length [cm]
37  adjustable V0 = 3000  -- initial potential [V]
38  adjustable V1 = 2000  -- secondary potential [V]
39  adjustable VL = 0     -- lens potential [V]
40  adjustable V1step = 0 -- step size for V1 optimization [V]
41  adjustable Kmax = 1   -- maximum kinetic energy (detector edge) [eV]
42  adjustable Kstep = 0  -- step size for Kmax optimization [eV]
43  adjustable m = 1      -- ion mass [Da]
44  adjustable batch = 0  -- batch mode switch (0 = off, any other = on)
45  adjustable vbeam = 0  -- molecular beam velocity [m/s]
46
47  local Rdet = 20       -- detector radius [mm]
48
49  -- This constant must agree with electode definitions in "real.gem":
50  local Nacc = 14 -- number of accelerator electodes; lens must be Nacc + 1
51
52  -- These constants must agree with patricle definitions in "real.fly2":
53  local N = 5   -- number of particles per group (# of angles, must be odd)
54  local a0 = 10 -- minimum angle (for "tau"; max. must be = 180 - min.)
55  local Np = 4  -- number of positions
56  local NK = 3  -- number of energies (highest must be 1st)
57
58  local SimplexOptimizer = require "simionx.SimplexOptimizer"
59  local opt -- optimizer object
60
61  local indat -- input file descriptor
62
63  -- Read parameters from the input file (batch mode)
64  function read_input()
65    L0, L1, V0, V1, VL, Kmax = indat:read("*n", "*n", "*n", "*n", "*n", "*n")
66  end
67
68  -- Initialization of particles (called for each particle)
```

```
69 function segment.initialize()
70   if (V1step ~= 0) or (Kstep ~= 0) then -- optimization enabled
71     if (batch ~= 0) and not indat then  -- first run in batch mode
72       indat = io.open("in.dat", "r")
73       read_input()
74     end
75     if not opt then                     -- first run (any mode)
76       opt = SimplexOptimizer {start = {V1, Kmax}, step = {V1step, Kstep},
77                               minradius = 1e-4}
78       sim_trajectory_image_control = 3 -- don't show or record
79     end
80     V1, Kmax = opt:values()
81   end
82   -- scale initial conditions:
83   ion_mass = m * ion_mass
84   local vscale = sqrt(Kmax / m)
85   ion_vx_mm = vscale * ion_vx_mm + 1e-3 * vbeam
86   ion_vy_mm = vscale * ion_vy_mm
87 end
88
89 -- Initialization of accelerator voltages
90 function segment.init_p_values()
91   for n = 1, Nacc do
92     adj_elect[n] = 0
93   end
94   local dV0 = (V0 - V1) / L0      -- field in the initial region
95   local dV1 = V1 / L1             -- field in the secondary region
96   local fL = 1 - (L0 - floor(L0)) -- fraction for the intermediate region
97   -- initial region:
98   local V = V0
99   for n = 0, floor(L0) do
100    adj_elect[n + 1] = V
101    V = V - dV0
102  end
103  -- treatment of intermediate region:
104  V = V + (dV0 - dV1) * fL
105  -- secondary region:
106  for n = floor(L0) + 1, floor(L0 + L1) do
107    adj_elect[n + 1] = V
108    V = V - dV1
109  end
110  -- lens:
111  adj_elect[Nacc + 1] = VL
112 end
113
```

```
114 local y = {} -- hit radii (positions at the detector)
115 local t = {} -- hit times
116 local lastN = N * Np * NK -- last ion number
117
118 local iter = 0
119 -- Positions at the detector and arrival times are recorded for each ion.
120 -- All analysis is performed after the last ion hit.
121 function segment.terminate()
122   local n = ion_number
123   y[n] = ion_py_mm
124   t[n] = ion_time_of_flight
125   if n < lastN then return end
126
127   -- These 2D arrays accumulate statistics for each group of equivalent ions
128   local Ey = {} -- average radius
129   local Dy = {} -- radius spread
130   local Et = {} -- average time
131   local Dt = {} -- time spread
132   -- statistics for groups:
133   for K = 0, NK - 1 do -- KEs
134     Ey[K] = {}
135     Dy[K] = {}
136     Et[K] = {}
137     Dt[K] = {}
138     for a = 0, N - 1 do -- angles
139       local nKa = K * (N * Np) + a + 1
140       local yKa, miny, maxy = 0, math.huge, -math.huge
141       local tKa, mint, maxt = 0, math.huge, -math.huge
142       for p = 0, Np - 1 do -- initial positions
143         local yKap = y[nKa + p * N]
144         yKa = yKa + yKap
145         miny, maxy = min(miny, yKap), max(maxy, yKap)
146         local tKap = t[nKa + p * N]
147         tKa = tKa + tKap
148         mint, maxt = min(mint, tKap), max(maxt, tKap)
149       end
150       Ey[K][a] = yKa / Np
151       Dy[K][a] = maxy - miny
152       Et[K][a] = tKa / Np
153       Dt[K][a] = maxt - mint
154     end
155   end
156
157   -- Calculations of overall characteristics
158   local Rmax = 0  -- maximum radius
```

```
159   local maxDK = 0 -- KE resolution
160   local tave = 0  -- average TOF
161   local maxDt = 0 -- TOF resolution
162   local tau       -- full TOF spread (estimated)
163   local Dt0       -- distortion of v_z = 0 slice (estimated)
164   for K = 0, NK - 1 do -- KEs
165     for a = 0, N - 1 do -- angles
166       Rmax = max(Rmax, Ey[K][a])
167       maxDK = max(maxDK, Ey[K][a] * Dy[K][a])
168       tave = tave + Et[K][a]
169       maxDt = max(maxDt, Dt[K][a])
170     end
171   end
172   -- final calculations and scaling:
173   tave = tave / (NK * N)
174   maxDK = 200 * maxDK / Rdet ^ 2
175   maxDt = maxDt * 1e3
176   tau = (Et[0][N-1] - Et[0][0]) / math.cos(a0 / 180 * math.pi) * 1e3
177   Dt0 = (Et[0][(N-1)/2] - (Et[NK-1][N-1] + Et[NK-1][0]) / 2) * 1e3
178   -- report to log window:
179   print()
180   iter = iter + 1
181   print(iter)
182   print("L0 =", L0, " L1 =", L1)
183   print("V0 =", V0, " VL =", VL)
184   print("V1 =", V1, " Kmax =", Kmax)
185   print(string.format("Rmax = %.4g mm",  Rmax))
186   print(string.format("maxDK = %.3g %%", maxDK))
187   print(string.format("tave = %.5g us",  tave))
188   print(string.format("maxDt = %.3g ns", maxDt))
189   print(string.format("tau = %.3g ns",   tau))
190   print(string.format("Dt0 = %.3g ns",   Dt0))
191
192   -- Optimization...
193   if (V1step ~= 0) or (Kstep ~= 0) then
194     local res = 0
195     if V1step ~= 0 then
196       res = maxDK
197     end
198     if Kstep ~= 0 then
199       res = res + 10 * abs(Rmax - Rdet) -- (factor "10" for sharper cusp)
200     end
201     opt:result(res)
202     if not opt:running() then -- end of optimization
203       -- write result to the file:
```

```
204       local fout = io.open("out.dat", "a")
205       fout:write(string.format(
206         "%g\t%g\t%g\t%.5g\t%g\t%.5g\t%.4g\t%.5g\t%.3g\t%.4g\t%.4g\t%.5g\n",
207         L0, L1, V0, V1, VL, Kmax, maxDK, tave, maxDt, tau, Dt0, Rmax))
208       fout:close()
209       -- next task or stop:
210       if batch ~= 0 then
211         opt = nil
212         if indat:read(0) ~= nil then
213           read_input()
214         else
215           indat:close()
216           V1step, Kstep = 0, 0 -- stop optimization
217           sim_trajectory_image_control = 0 -- show and retain
218         end
219       else
220         V1step, Kstep = 0, 0 -- stop optimization
221         sim_trajectory_image_control = 0 -- show and retain
222       end
223     end
224     sim_rerun_flym = 1
225   else
226     sim_rerun_flym = 0
227   end
228
229   sim_retain_changed_potentials = 1
230
231 end -- program
```

B Additional Pareto-optimal ion optics parameters and performance characteristics

B.1 With respect to ΔK and Δt

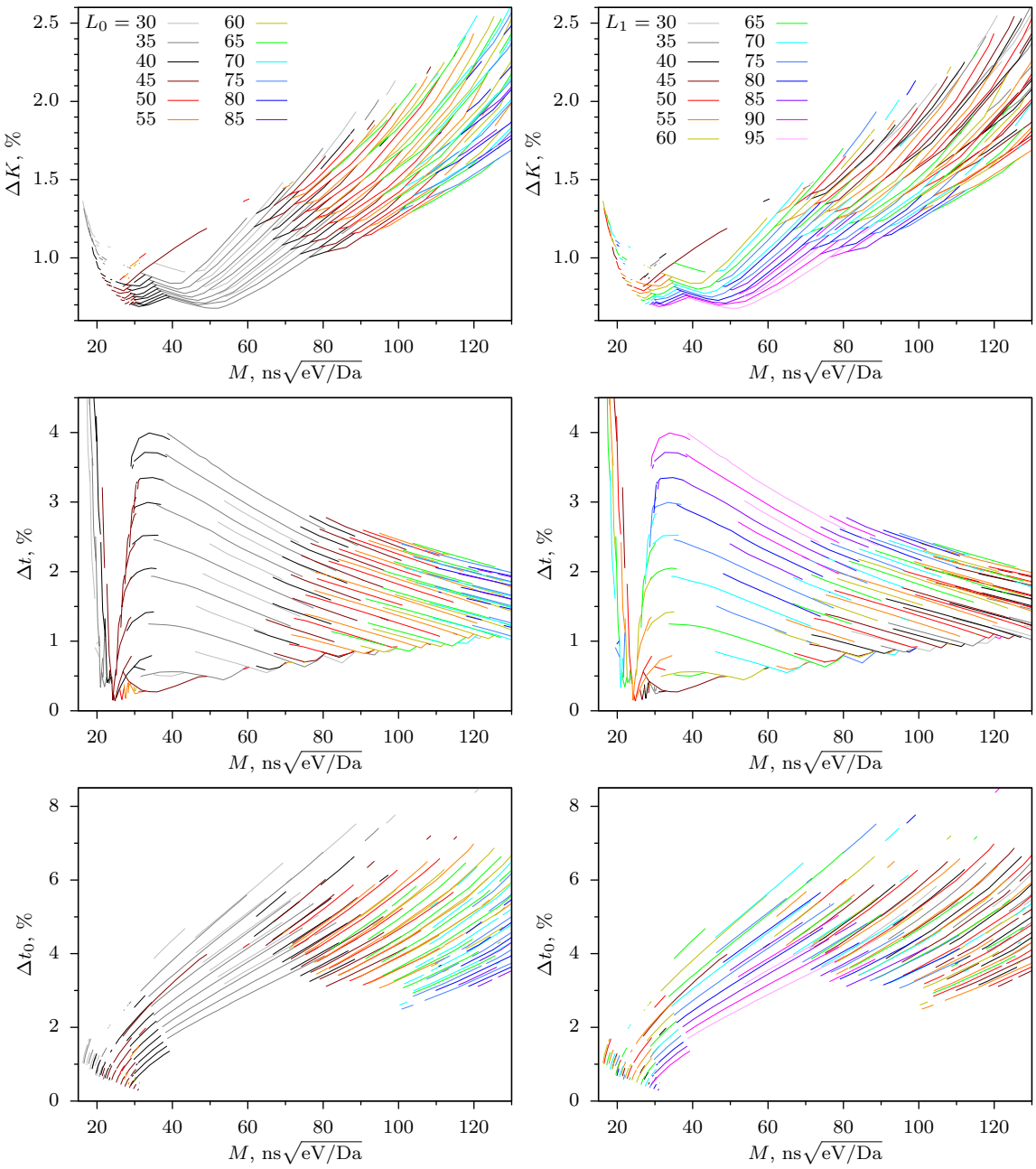

Figure B.1 Relative overall kinetic energy and TOF resolutions as functions of magnification index. (Lengths L_0 and L_1 are in mm.)

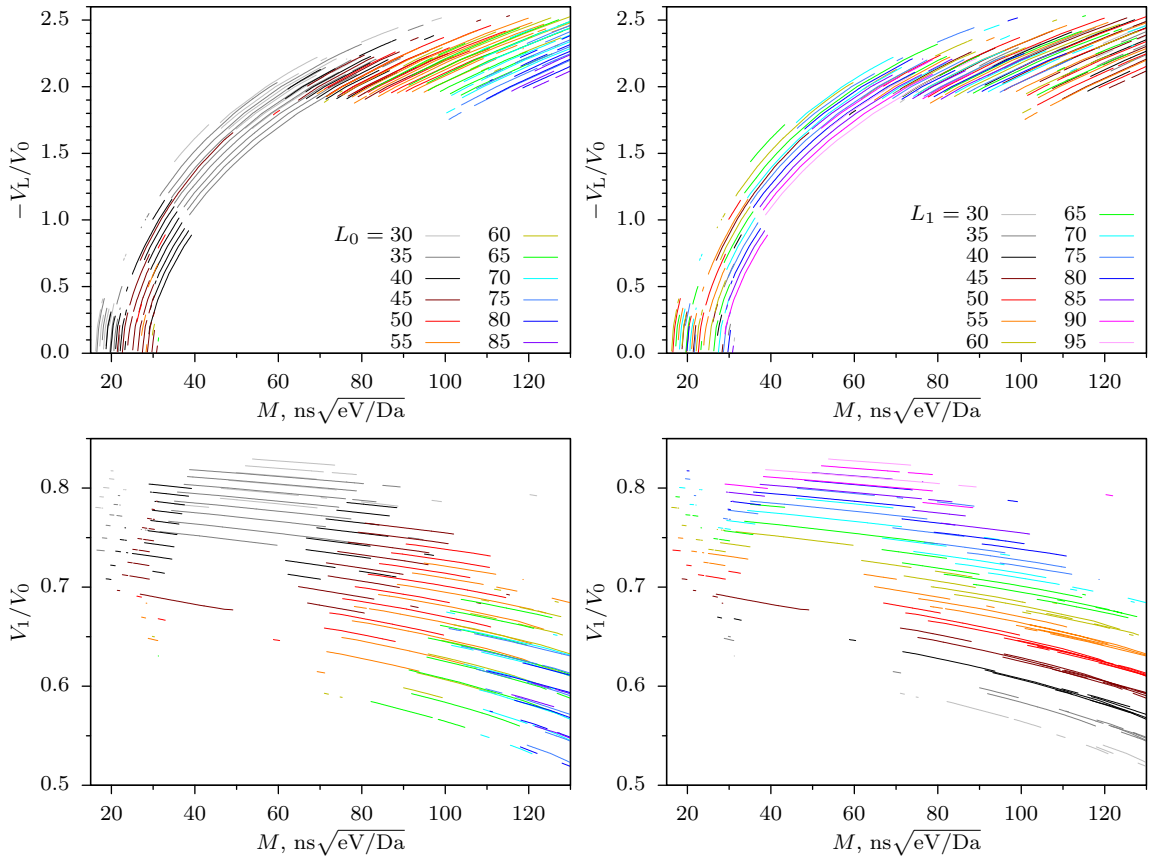

Figure B.2 Interdependence of ion optics parameters and magnification index. (Lengths L_0 and L_1 are in mm.)

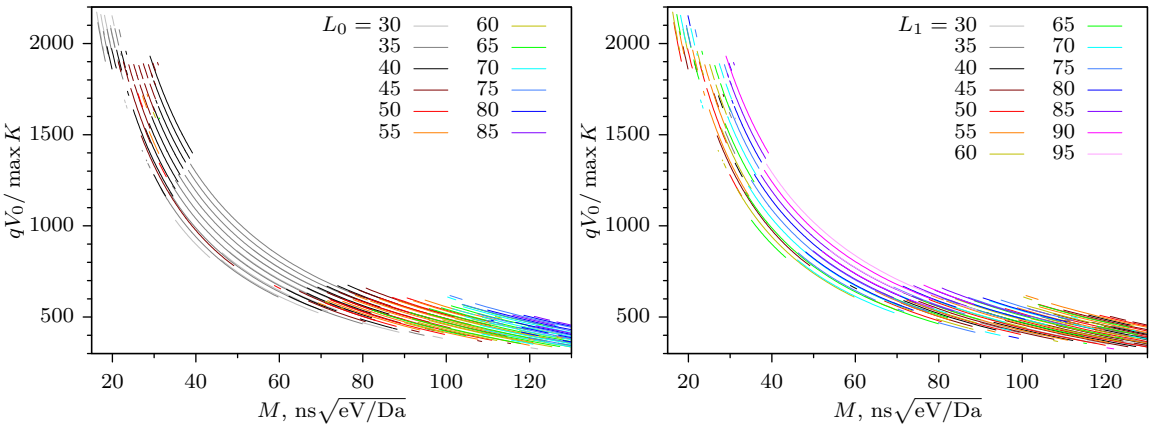

Figure B.3 Dependence of voltage scale on imaged kinetic energy range and magnification index. (Lengths L_0 and L_1 are in mm.)

B.2 With respect to ΔK and Δt_0

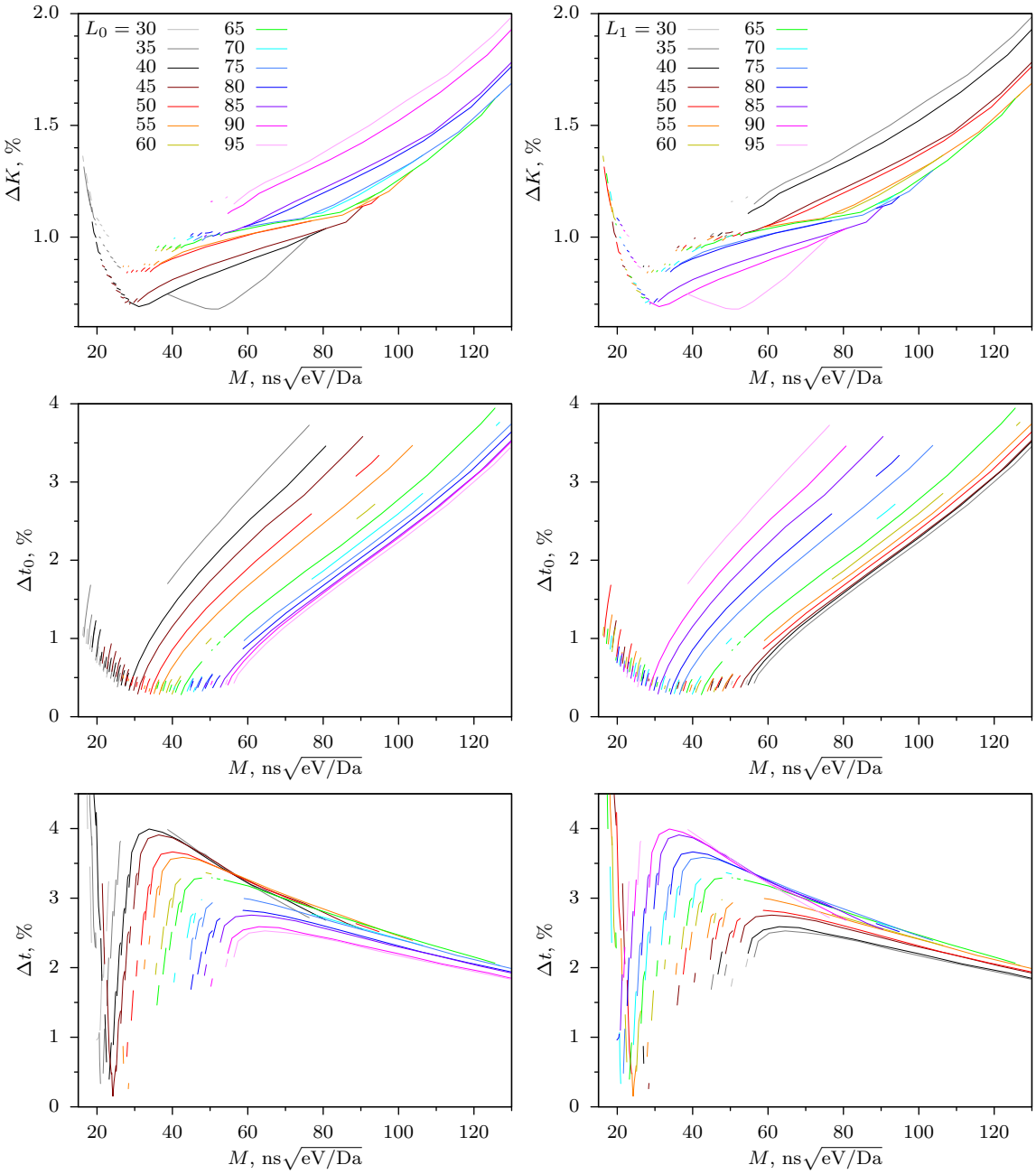

Figure B.4 Relative overall kinetic energy and TOF resolutions as functions of magnification index. (Lengths L_0 and L_1 are in mm.)

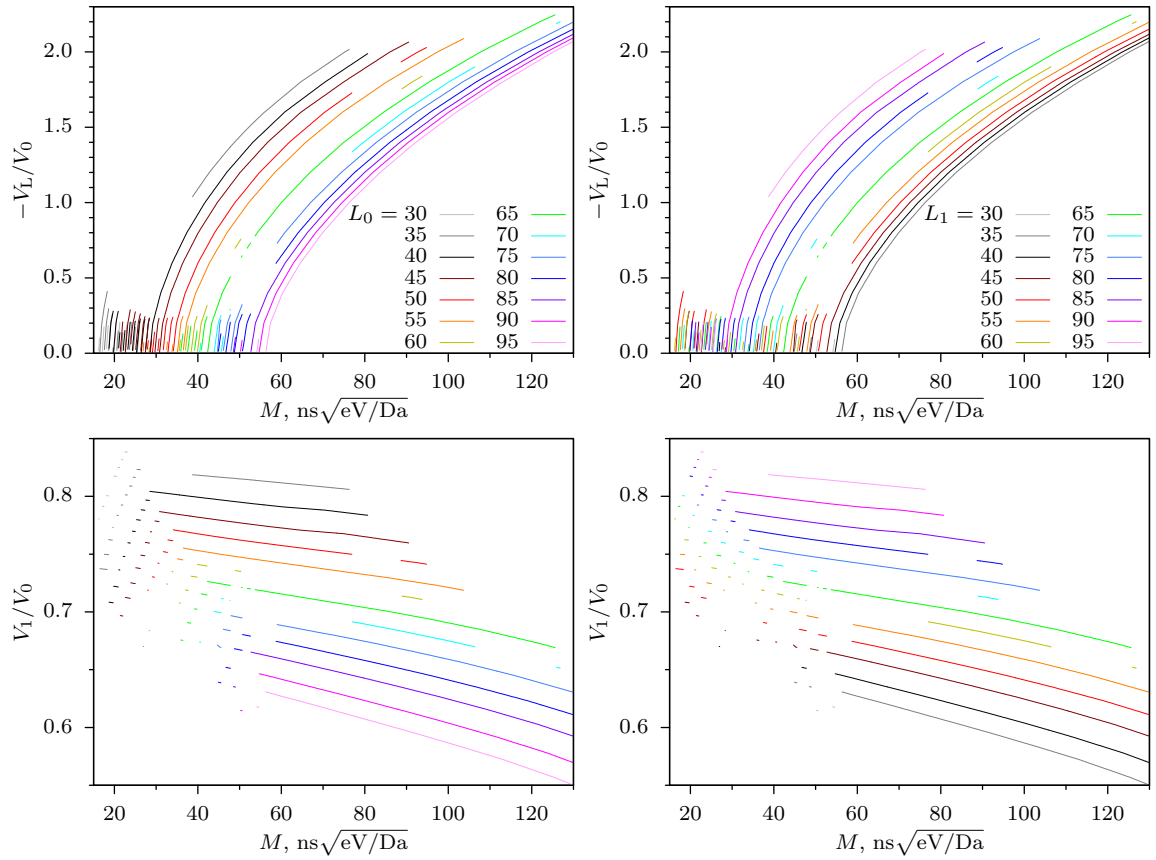

Figure B.5 Interdependence of ion optics parameters and magnification index. (Lengths L_0 and L_1 are in mm.)

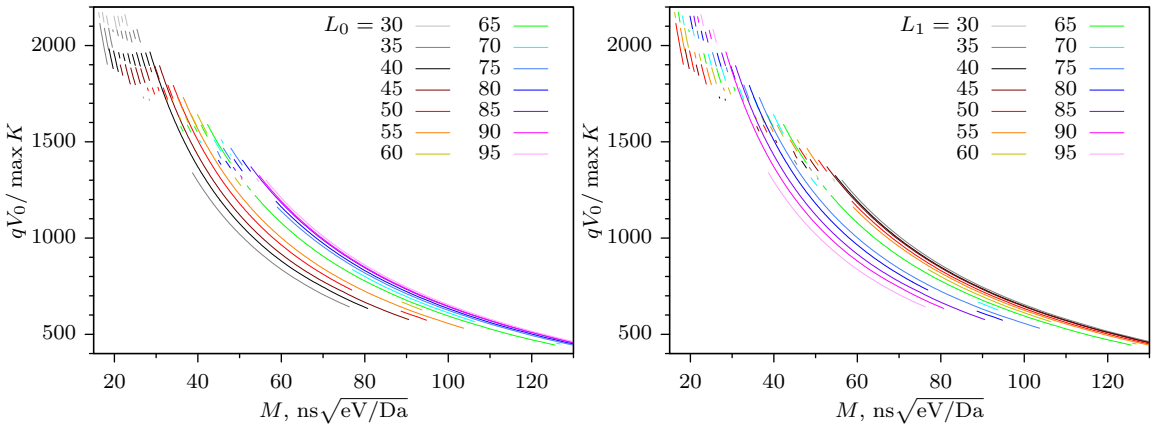

Figure B.6 Dependence of voltage scale on imaged kinetic energy range and magnification index. (Lengths L_0 and L_1 are in mm.)

C Mechanical drawings and photographs

This appendix includes scaled down drawings submitted to the USC machine shops for manufacturing of the custom-made parts. No descriptions for standard parts (such as nuts, set screws, washers and so on) that were purchased from McMaster-Carr are included. If necessary, their parameters can be derived from the parameters of the matching parts.

The drawings have captions and comments included within and therefore are given below "as is" without figure numbers and captions.

Photographs of the most important subassemblies are provided in figures C.1–C.4 after the drawings. They were taken in laboratory directly during the assembly process, without any special preparations, and therefore have relatively poor quality but should be sufficient for illustration purposes.

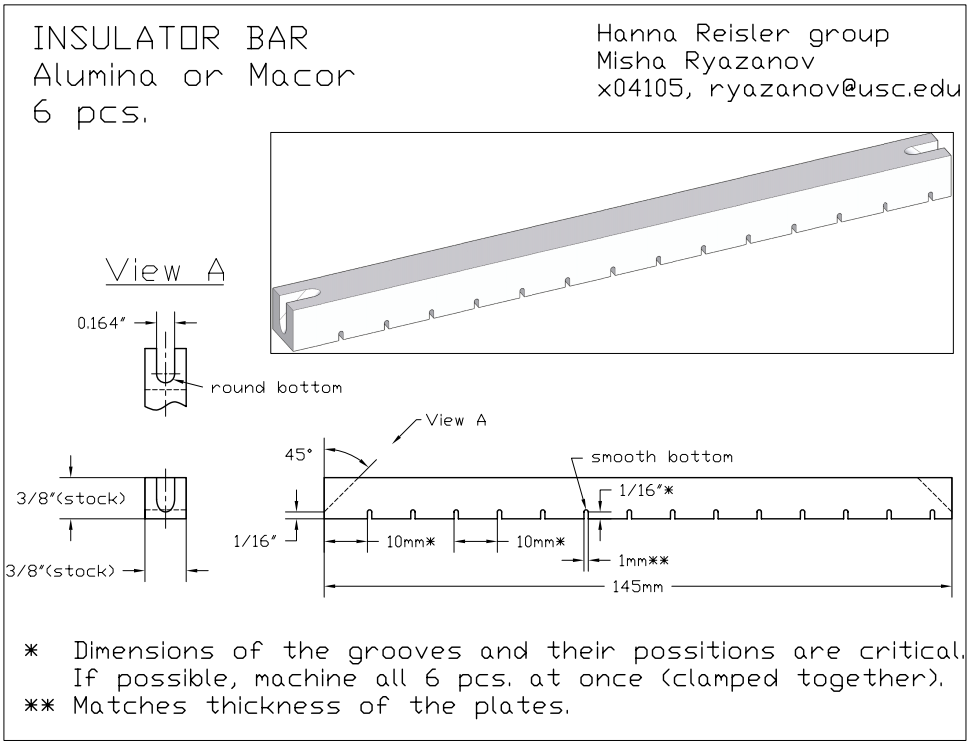

FRAME RING 1
Stainless steel
(non-magnetic)
1 pc.

Hanna Reisler group
Misha Ryazanov
x04105, ryazanov@usc.edu

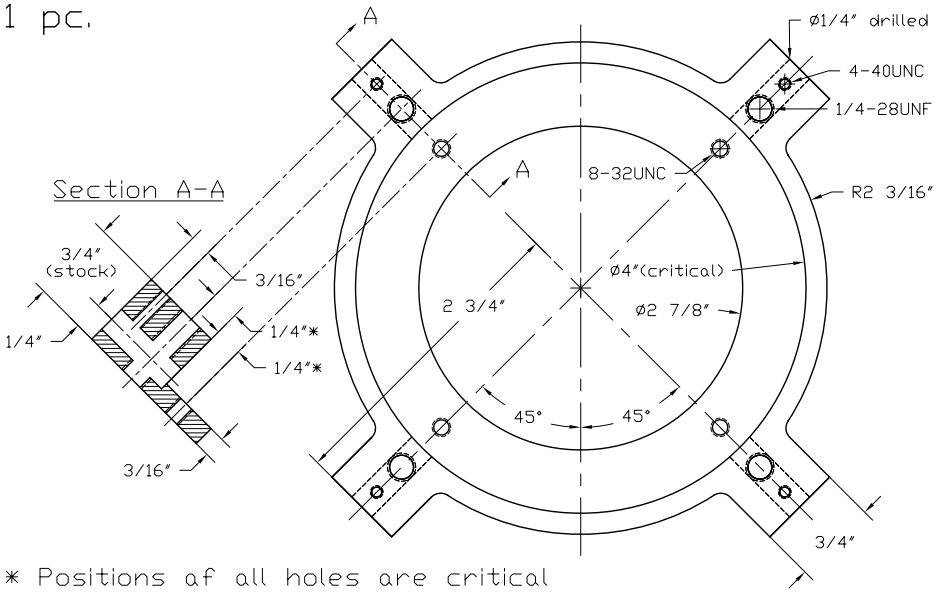

* Positions af all holes are critical

FRAME RING 2
Stainless steel
(non-magnetic)
1 pc.

Hanna Reisler group
Misha Ryazanov
x04105, ryazanov@usc.edu

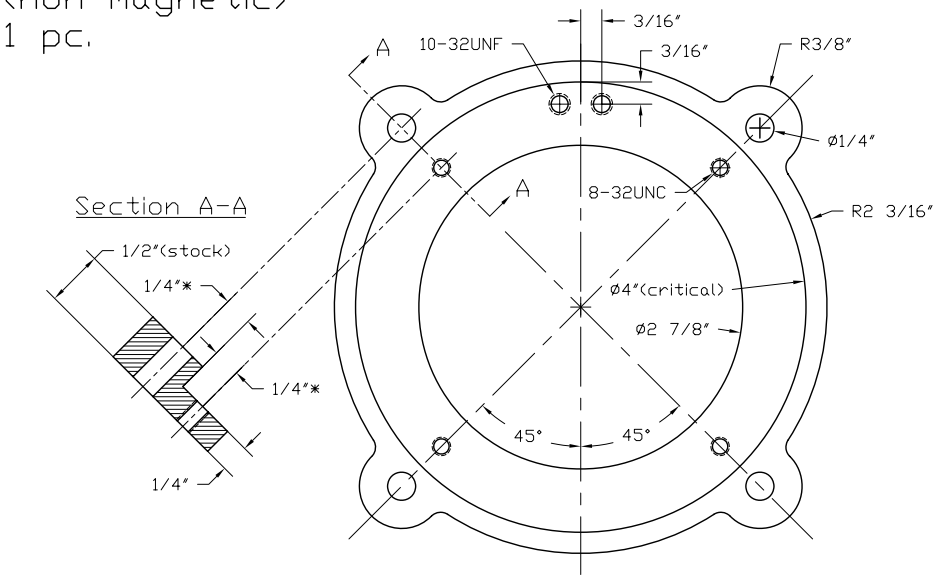

* Positions af all holes are critical

SCREW
Bronze
(non-magnetic, no zinc)
4 pcs.

Hanna Reisler group
Misha Ryazanov
x04105, ryazanov@usc.edu

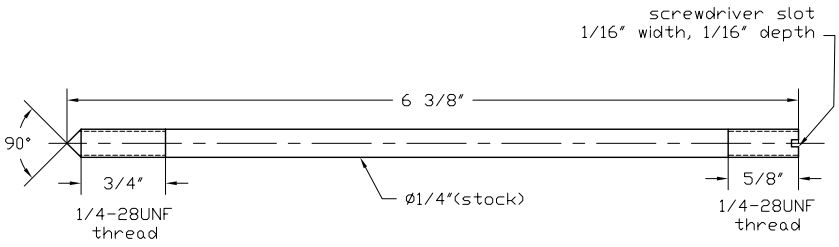

PIN
Bronze
(non-magnetic, no zinc)
4 pcs.

Hanna Reisler group
Misha Ryazanov
x04105, ryazanov@usc.edu

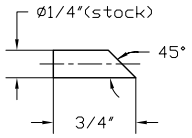

1ST PLATE
□FE Copper
1 pc.

Hanna Reisler group
Misha Ryazanov
x04105, ryazanov@usc.edu

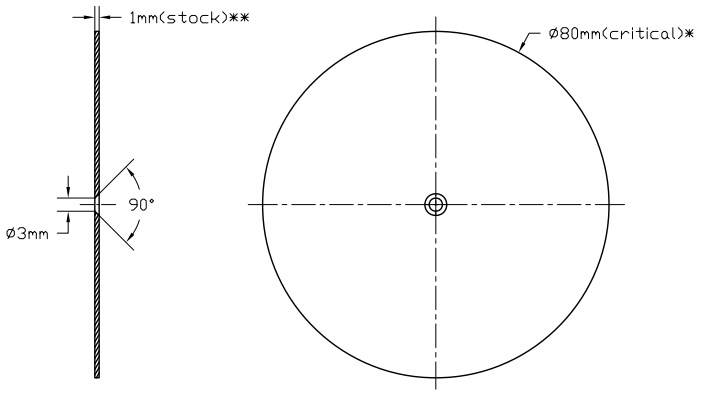

* External diameters of all plates are critical.
If possible, machine all plates at once (clamped together).
** Use sheet stock with closest thickness
(+ see notes for "INSULAT□R BAR").

PLATE
□FE Copper
15 pc.

Hanna Reisler group
Misha Ryazanov
x04105, ryazanov@usc.edu

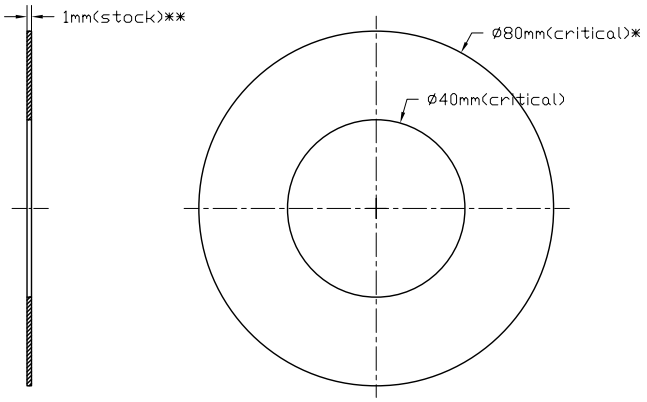

* External & internal diameters of all plates are critical.
If possible, machine all plates at once (clamped together).
** Use sheet stock with closest thickness
(+ see notes for "INSULAT□R BAR").

ALIGNMENT HOOK
Stainless steel
1 pc.

Hanna Reisler group
Misha Ryazanov
x04105, ryazanov@usc.edu

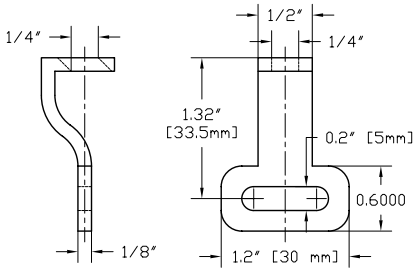

Was made in the lab to fit the chamber dimensions.

ALIGNMENT SCREW
Stainless steel
1 pc.

Hanna Reisler group
Misha Ryazanov
x04105, ryazanov@usc.edu

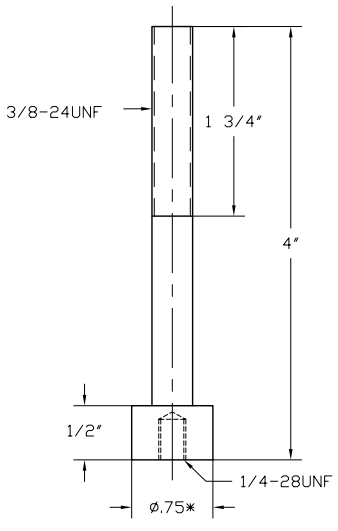

Assembly:

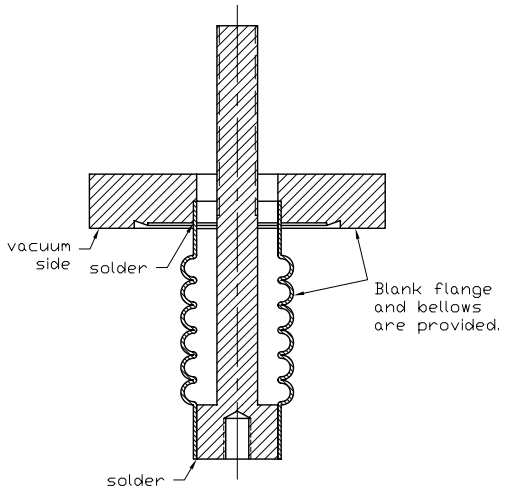

* The screw should fit into the bellows.

ALIGNMENT SLIDER
Stainless steel
1 pc. each

Hanna Reisler group
Misha Ryazanov
x04105, ryazanov@usc.edu

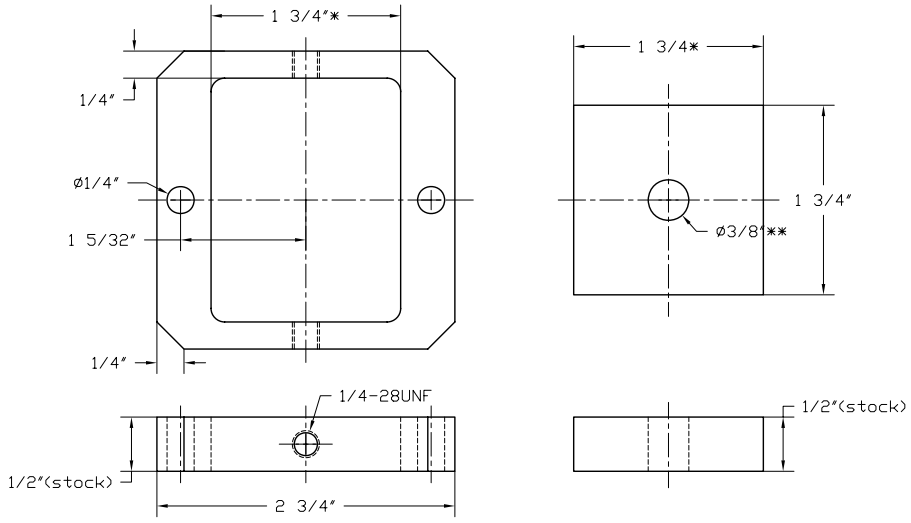

* The smaller part should slide in the bigger one with no significant play.
** "ALIGNMENT SCREW" should fit into this hole with no significant play.

ALIGNMENT NUT
Brass
1 pc.

Hanna Reisler group
Misha Ryazanov
x04105, ryazanov@usc.edu

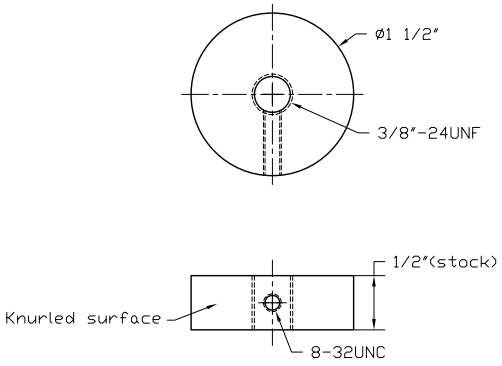

LENS RING 1
Stainless steel (non-magnetic)
2 pcs.

Hanna Reisler group
Misha Ryazanov
x04105, ryazanov@usc.edu

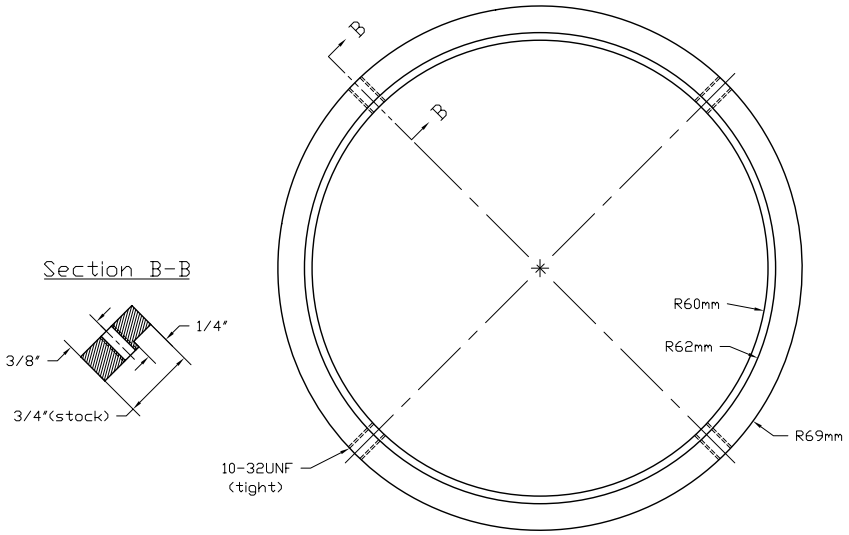

Section B-B

Note: "RING 1", "RING 2" and "RING 3" all have similar shapes.

LENS RING 2
Stainless steel (non-magnetic)
2 pcs.

Hanna Reisler group
Misha Ryazanov
x04105, ryazanov@usc.edu

Section A-A

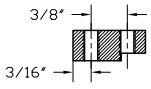

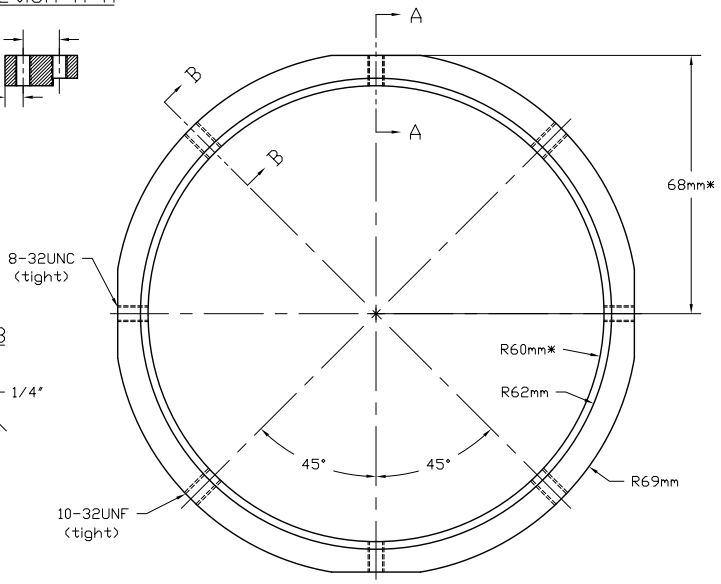

Section B-B

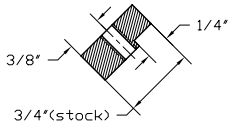

* These dimensions and positions af all holes are critical

LENS RING 3
Stainless steel (non-magnetic)
2 pcs.

Hanna Reisler group
Misha Ryazanov
x04105, ryazanov@usc.edu

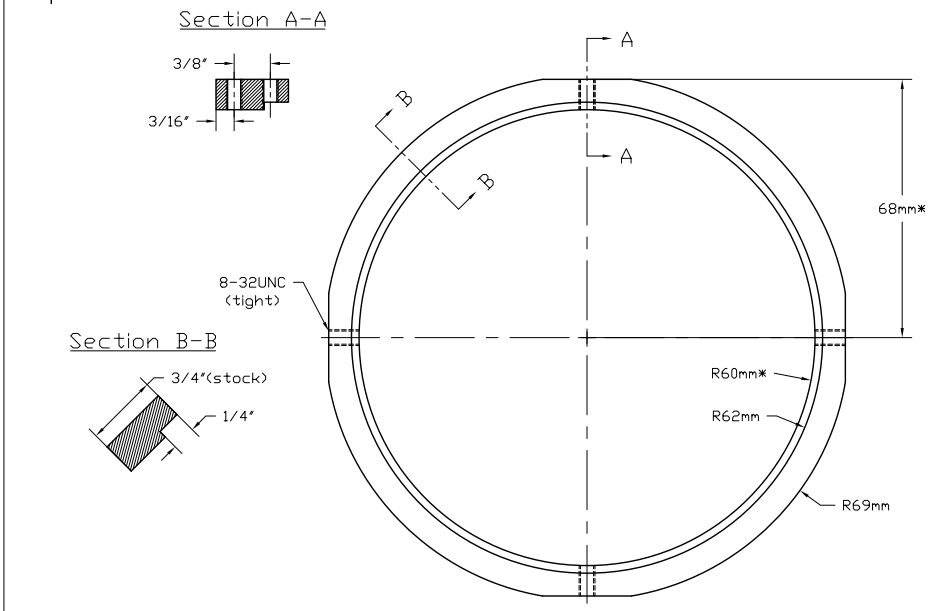

* These dimensions and positions af all holes are critical

LENS INSULATOR
Macor
10 pc.

Hanna Reisler group
Misha Ryazanov
x04105, ryazanov@usc.edu

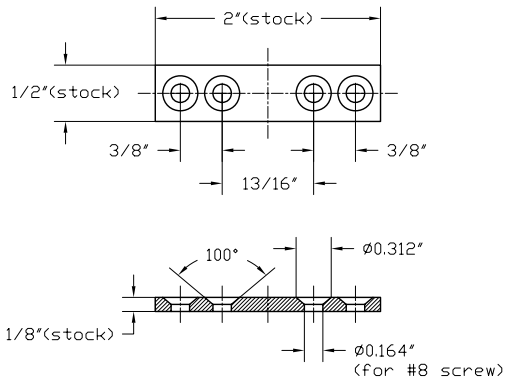

Positions af all holes are critical

LENS SHIELD
Stainless steel (non-magnetic) perforated sheet.
Thickness: about 1mm; Hole diameter: < 4mm.
3 pcs.

Hanna Reisler group
Misha Ryazanov
x04105, ryazanov@usc.edu

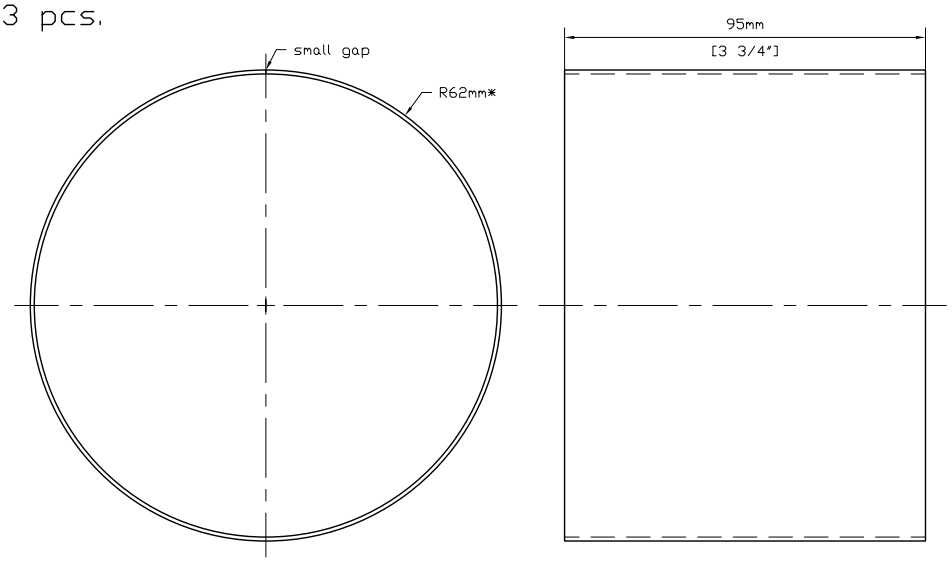

* The "SHIELD"s are intented to be inserted into the "LENS RING"s.

MCP SHIELD
□FE Copper
1 pc.

Hanna Reisler group
Misha Ryazanov
x04105, ryazanov@usc.edu

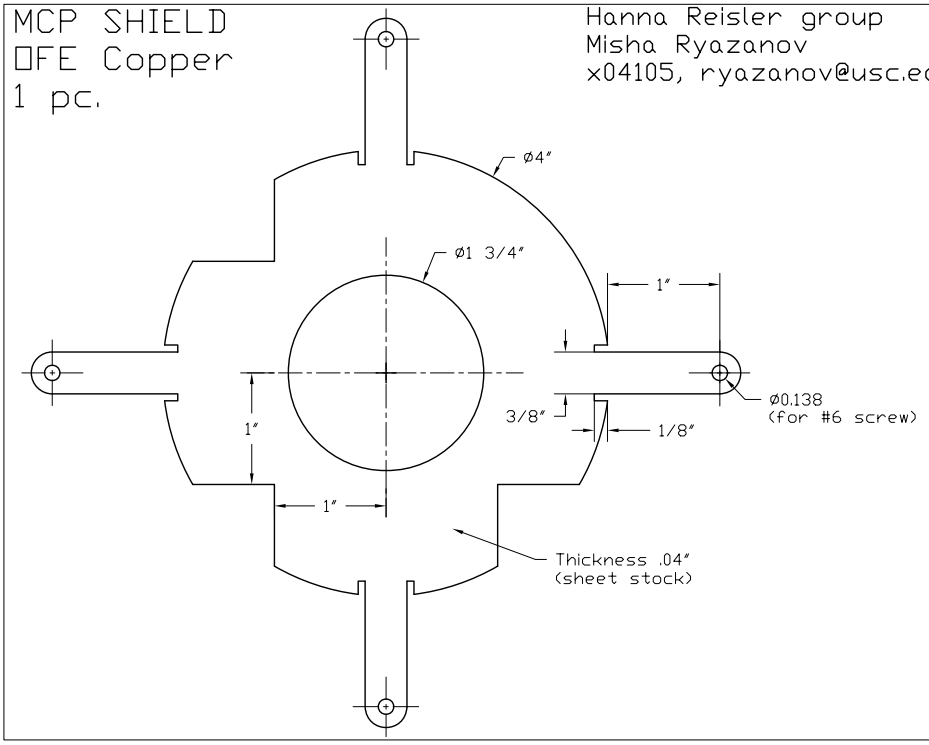

REDUCER FLANGE
(Flange is provided)

Hanna Reisler group
Misha Ryazanov
x04105, ryazanov@usc.edu

Front view:

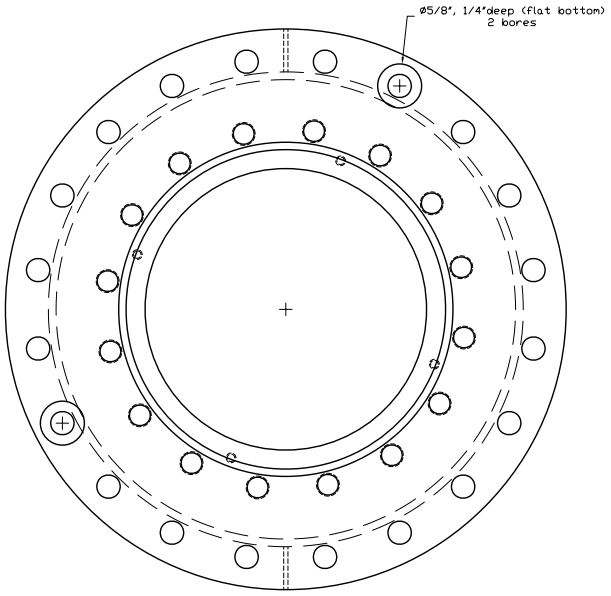

REDUCER FLANGE
(Flange is provided)

Hanna Reisler group
Misha Ryazanov
x04105, ryazanov@usc.edu

Rear view:

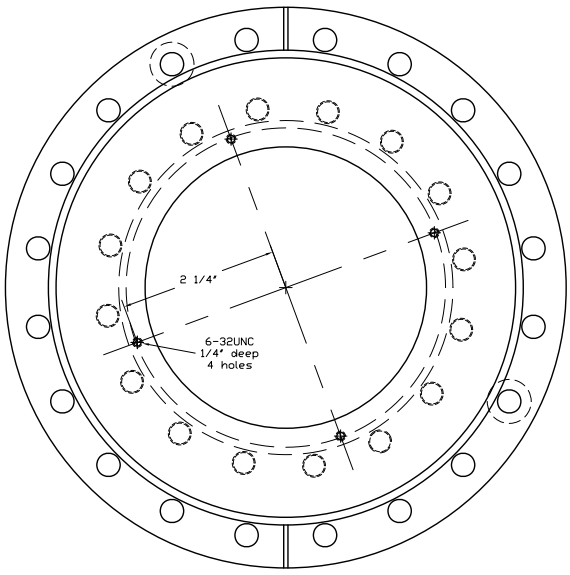

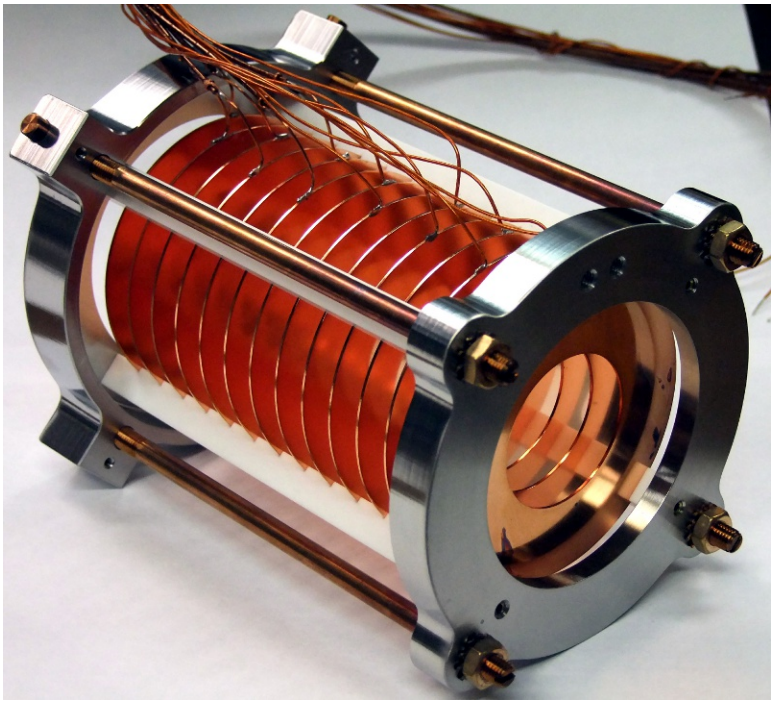

Figure C.1 Accelerator assembly.

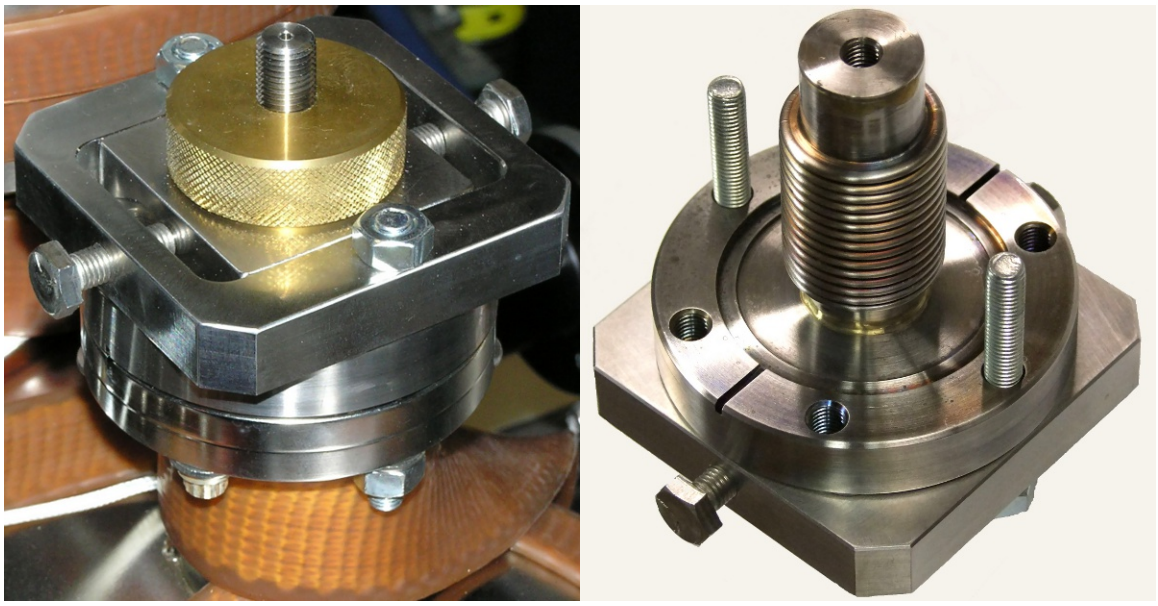

Figure C.2 Top (installed) and bottom views of accelerator suspension and alignment assembly.

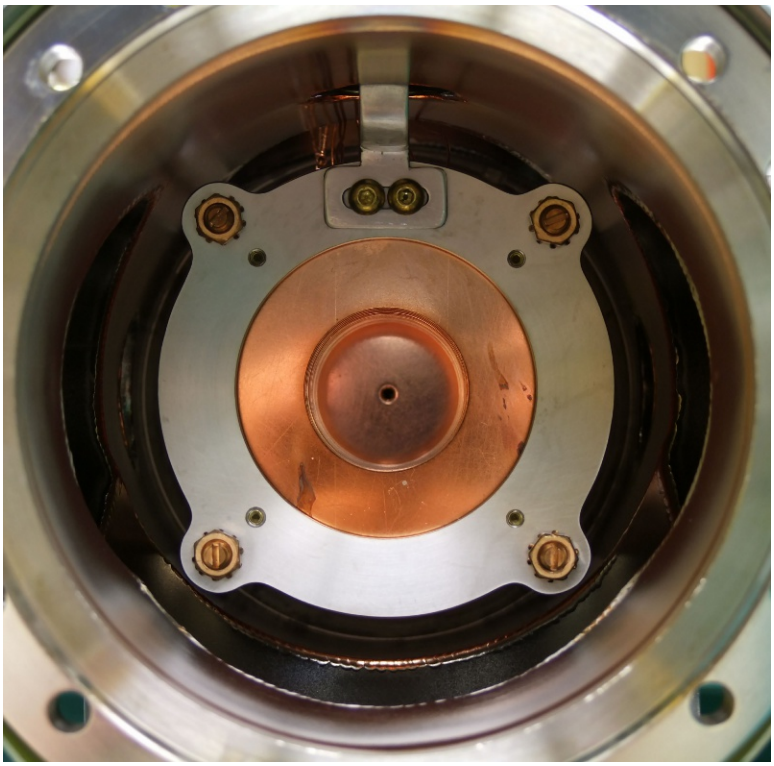

Figure C.3 Accelerator installed in the vacuum chamber (without extension).

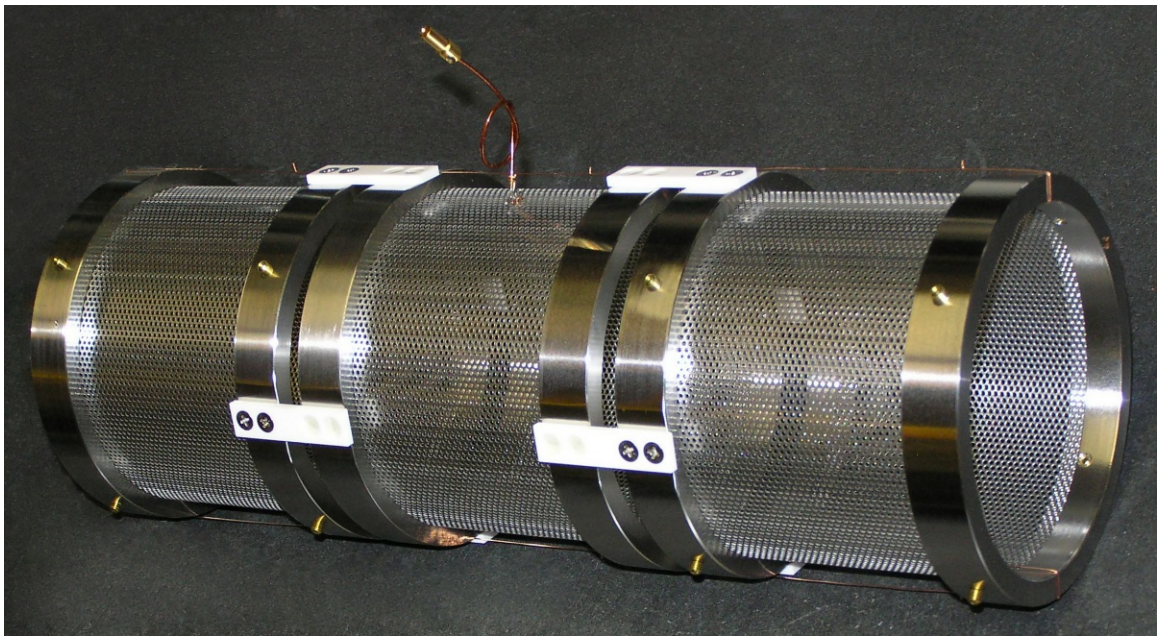

Figure C.4 Additional lens. (Thin copper wires holding the parts together before installation are cut and removed after anchoring inside the vacuum chamber.)

D Electronic circuit diagrams

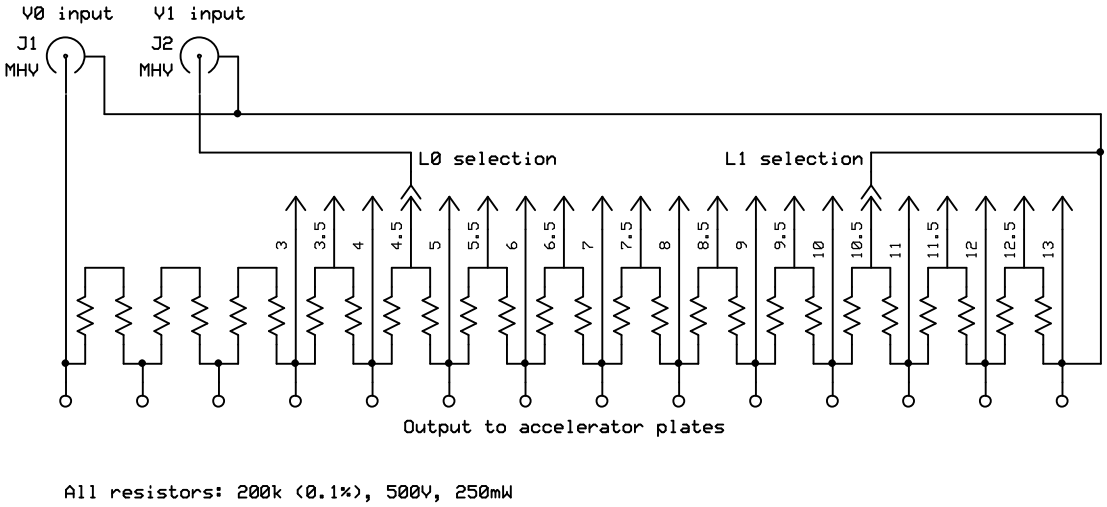

Figure D.1 Voltage divider for accelerator. Connections for effective lengths $L_0 = 45$ mm (4.5 cm), $L_1 = 60$ mm (6 cm = 10.5 cm – 4.5 cm) are illustrated.

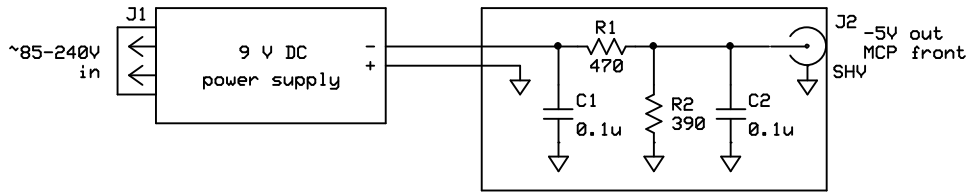

Figure D.2 Bias voltage supply for detector front plate.

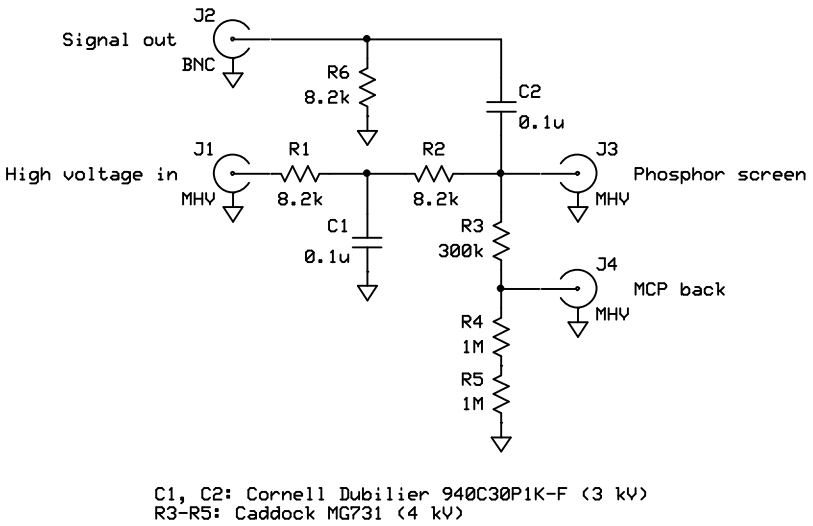

Figure D.3 Voltage divider and signal decoupler for detector operation in electrical signal pickup mode.

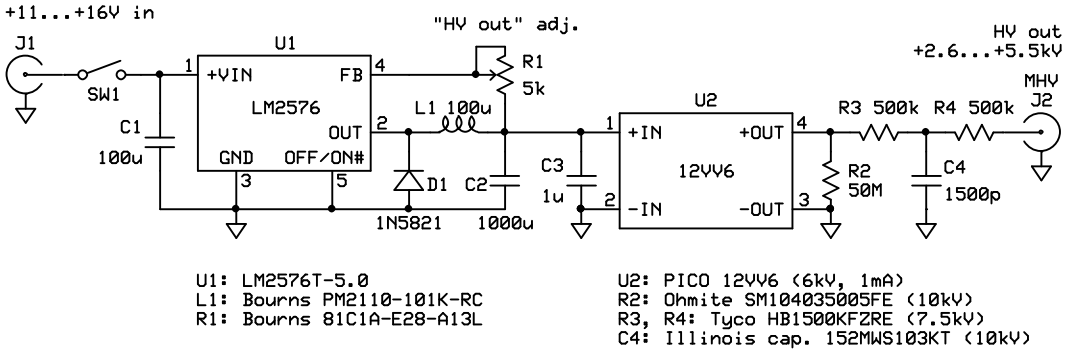

Figure D.4 Phosphor screen voltage supply for detector operation in imaging mode.

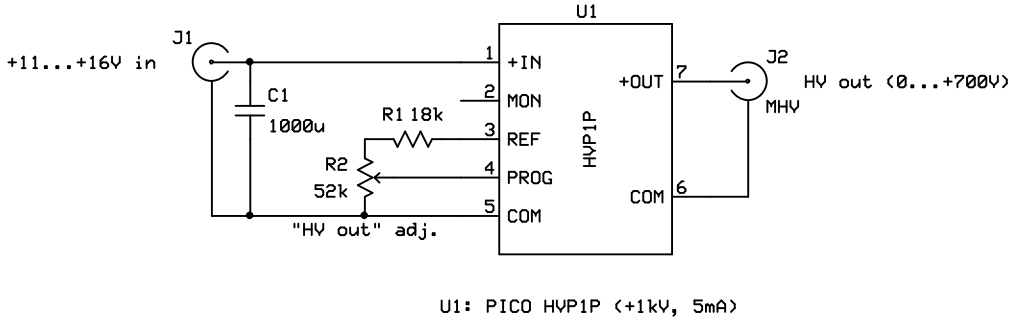

Figure D.5 Voltage supply for AV-HVX-1000A pulser.

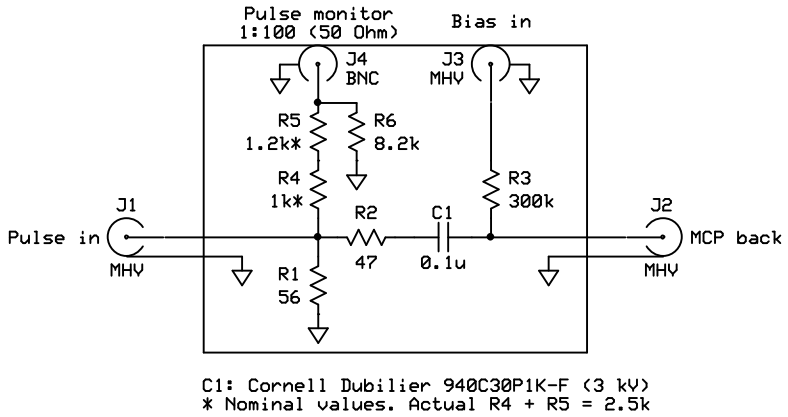

Figure D.6 Pulse and bias voltage combiner for AV-HVX-1000A pulser.

E High-voltage nanosecond pulser

The pulser is used for fast gating of the MCP-based particle detector in SVMI experiments. It produces electrical pulses of fixed duration (halfwidth ~5 ns) with amplitude adjustable in the whole operating range of the detector (up to ~2 kV) and is self-contained, requiring only a low-voltage (11−14 V, 3 A) power supply and an input TTL triggering signal ($\gtrsim$100 ns duration). The generated pulse is delivered to the detector through a short (~20 cm) cable with an SHV connector that must be connected directly to the detector electrical feedthrough. A 100-fold attenuated ($\lesssim$20 V amplitude) pulse is also provided through a BNC connector for monitoring purposes. It can be fed to any device with 50 Ohm input impedance using an appropriate cable of arbitrary length.

The design was suggested by Dr. András Kuthi from the Pulsed Power Laboratory at USC and essentially represents a downscaled version of a megavolt-range pulser described in [50] (see also [51]). The pulser consists of an initial energy storage capacitor, a relatively slow semiconductor switch followed by a 3-stage magnetic pulse compressor and ends with a step-recovery diode opening switch. The basic circuit diagram is shown in figure E.1 (compare to figures 5 and 6 in [50]).

The main principles of the pulse forming sequence can be described as follows. A slow charging (phase A in figure E.1) of the energy storage capacitor $C1$ through the current-limiting resistor $R1$ and the primary winding of the transformer T prepares the system before the pulse generation can be initiated by an incoming trigger

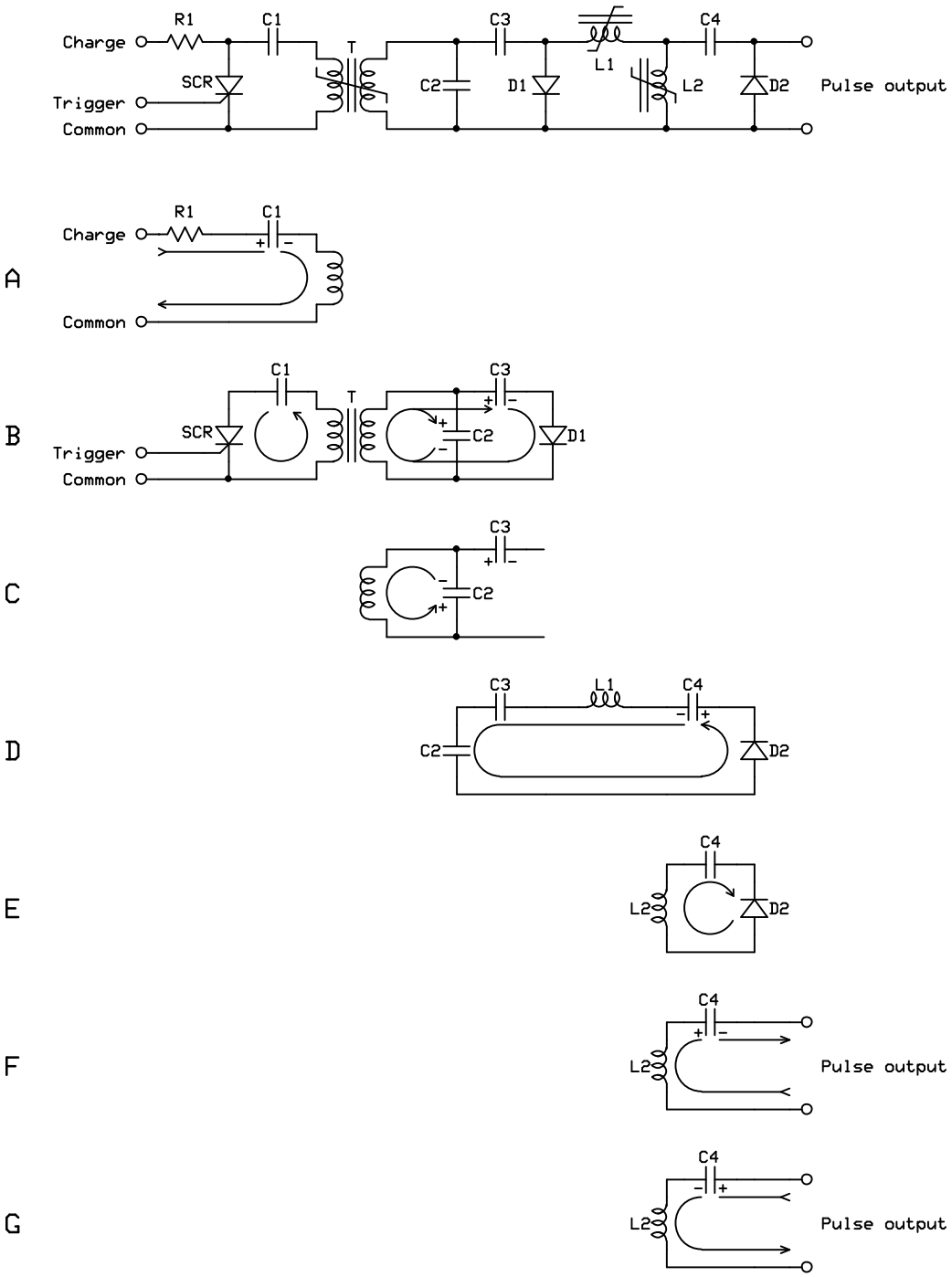

Figure E.1 Schematic circuit diagram and operation sequence.

signal. Upon triggering (phase B), $C1$ starts discharging through the opened SCR switch and the saturable transformer T, charging capacitors $C2$ and $C3$ connected in parallel through the diode $D1$. When the maximum current through T is reached, the transformer core becomes saturated. At that point the coupling between the primary and secondary windings is lost, and the inductance of the secondary winding drops to a low value, leading to a quick recharging of $C2$ in the reverse polarity (phase C). Then the transformer core gets out of saturation, significantly increasing the secondary winding impedance. At the same time, the current produced by $C2$ and $C3$ (now connected in series) discharging through the diode $D2$ and the inductor $L1$ saturates the core of $L1$,[1] which leads to a quick charging of the capacitor $C4$ (phase D). During this process the p–n junction of $D2$ is saturated with charge carriers, which makes possible backward discharging of $C4$ through the inductor $L2$ and $D2$ using its reverse recovery effect. The discharge current saturates the $L2$ core (phase E),[2] which in turn increase the $C4$ discharge rate. The charge stored in $D2$ is eventually depleted, and the current abruptly stops flowing through the diode. Since the high current in $L2$ cannot disappear immediately, its path becomes closed through $C4$ and the load connected to the pulser output (phase F), which causes a high voltage spike due to the load resistance. The LC circuit formed by $L2$, $C4$ and the load leads to subsequent recharging of $C4$ in the opposite direction, which causes an equally quick decrease of the load voltage (phase G). In principle, these oscillations could continue for several periods, creating unwanted ringing instead of a single pulse. However, with correctly chosen parameters of the circuit, desaturation of the $L2$ core after the first cycle and damping in the load prevent further spikes.

The actual circuit diagram of the present pulser implementation is shown in figure E.2.[3] The lack of specifications for electrical parameters of the detector, as well as the usage of regular rectifier diodes, which are made not for step recovery operation and hence also have no specifications for parameters relevant to such operation,[4] required matching of some characteristics by trial and error. This especially

[1] A preceding slow discharge of $C3$ through the secondary winding of T, $L2$ in parallel with $D2$–$C4$, and $L1$ helps this saturation.

[2] This is facilitated by the currents already flowing through $L2$ in the same direction during phases C and D.

[3] Main part. The additional circuits are shown in figure E.3.

[4] The choice of diodes was based simply on the fact that the availability and prices of "real" step-recovery diodes rated for such high voltages are beyond reasonable. At the same time, high-voltage rectifier diodes are relatively cheap and were already successfully used for pulser constructions in the

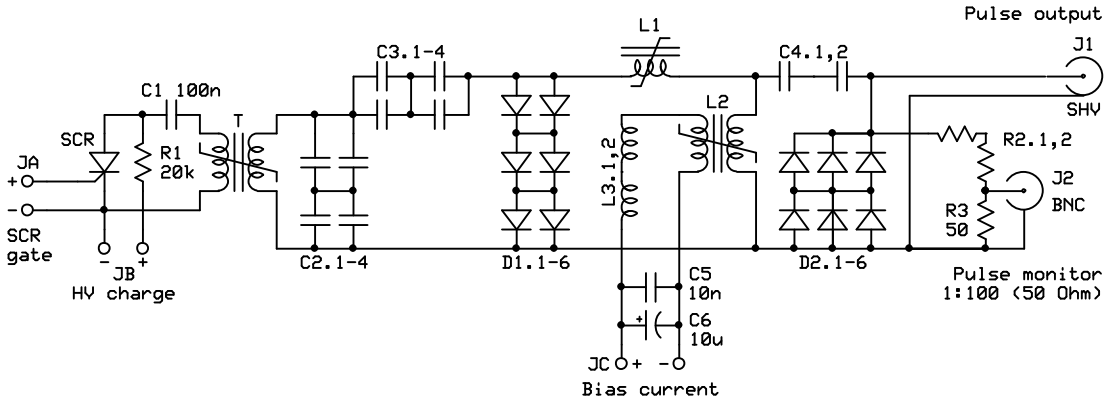

T (x2), L1, L2 cores: Ceramic Magnetics CMD5005 ferrite, 2" OD, 1" ID, 0.5" H
T: 1 turn / 2 turns
L1: 2 turns (x2 in parallel)
L2: 2 turns (x2 in parallel) + 2 turns (bias)

SCR: Teccor SK065K, 1kV, 65A
R1: >1 kV
C1: Epcos B32652, 1 kV
C2-4.n (each): AVX MLC, 8200pF, C0G, 1kV
D1.n (each): Fairchild RHRP30120, 1.2kV, 30A, hyperfast
D2.n (each): IRF (Vishay) 60EPS12, 1.2kV, 60A
L3.n (each): Delavan 4590R, 220u, 2A, >1kV!
R2 (total): 2.5k, >2 kV

Figure E.2 Main board.

pertains to capacitor values, the number and type of $D2$ diodes, and saturable inductor parameters. The bias current circuit that was added to the last core (of $L2$) allows to create some premagnetization and therefore to adjust the saturation moment in time. This helps in achieving the maximum energy efficiency, which not only maximizes the output pulse amplitude, but also prevents afterpulses due to the unused energy circulating in the magnetic compressor stages. The pulse amplitude is adjusted mostly by changing the primary charge voltage, but at each voltage the bias current must be also adjusted for best performance. Typical values in the present setup are 560 V charge and 750 mA bias. The produced pulses have ~1800 V amplitude[1] and ~5 ns halfwidth of the main peak. The electrical pulse has some lower-frequency oscillations before and some high-frequency oscillations after the main peak (see figure E.4), but their total amplitude does not exceed ~500 V and has no effect on the detector operation.

Pulsed Power Laboratory at USC. Among them the models with sufficient forward current ratings (for phase D in figure E.1) must be chosen. An addition selection criterion is that devices with larger physical size of the p–n junction generally have larger stored charge.

[1]Due to the lack of correct impedance matching in the system (the main reason for which is that the detector itself was not properly designed for fast switching) the actual pulse amplitude at the detector cannot be measured accurately. The pulse monitor installed at the pulser output (before the cable) apparently can give up to ~20 % error depending on the propagation characteristics. The quoted amplitude was estimated by comparison of the produced signal intensities with a slower pulser, for which the voltage can be measured without complications.

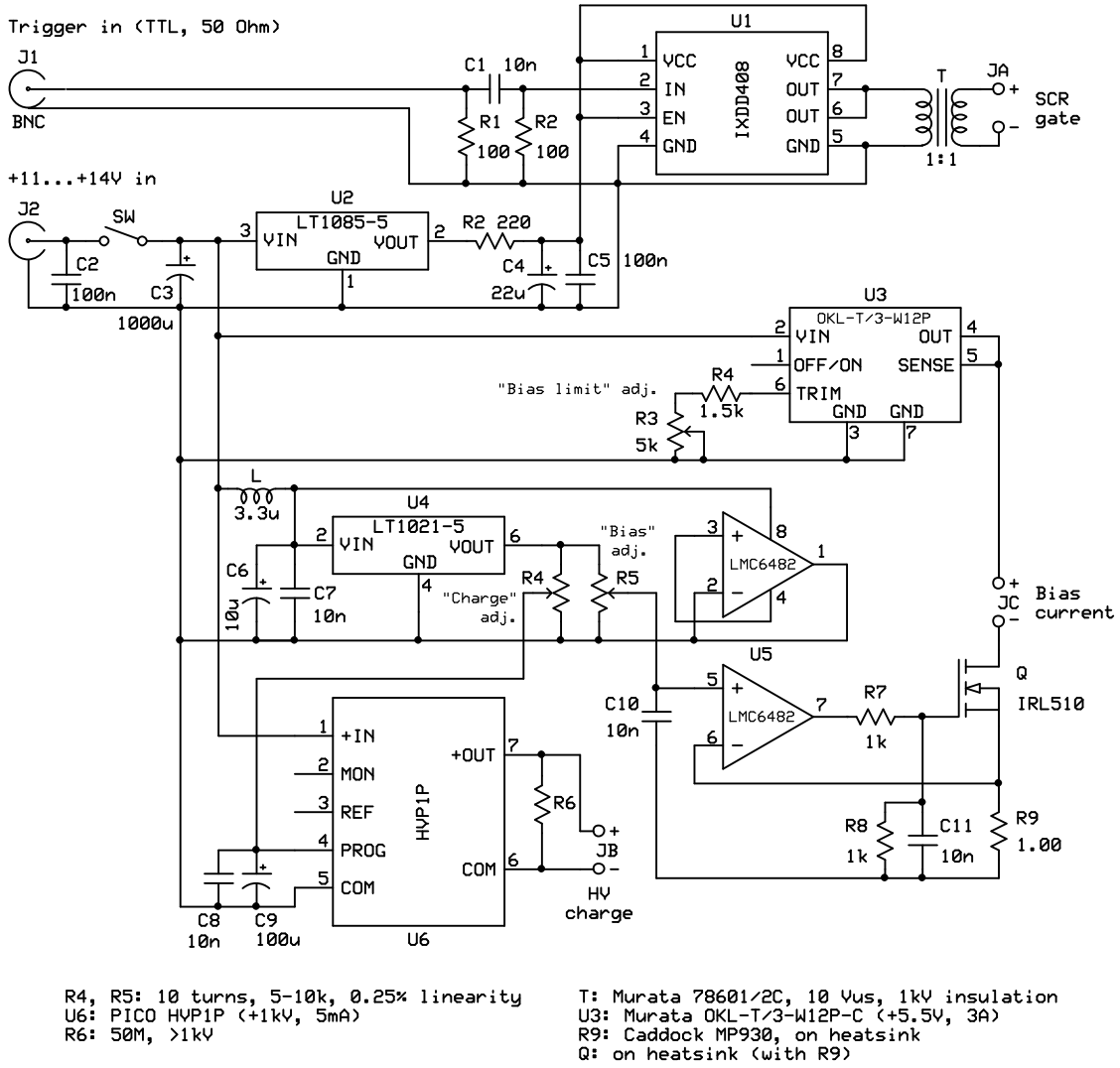

R4, R5: 10 turns, 5-10k, 0.25% linearity
U6: PICO HVP1P (+1kV, 5mA)
R6: 50M, >1kV

T: Murata 78601/2C, 10 Vus, 1kV insulation
U3: Murata OKL-T/3-W12P-C (+5.5V, 3A)
R9: Caddock MP930, on heatsink
Q: on heatsink (with R9)

Figure E.3 Auxiliary board.

Figure E.3 shows the auxiliary circuits required for pulser operation. They include the adjustable high voltage supply for the pulser charging ($U6$ and $R4$), the SCR gate driver ($U1$ and T) and the adjustable current source for the bias current ($U3$, Q, $U5$ and $R5$). The latter uses a voltage source $U3$ and linear current regulation by the transistor Q, which dissipates the excess voltage. Since the dissipated power is equal to the output bias current multiplied by the dissipated voltage, it might become substantial if the $U3$ output voltage is too high. At the same time, low voltage will limit the maximal possible output current. Therefore, a coarse voltage adjustment by the resistor $R3$ is provided. To minimize heat dissipation at any given

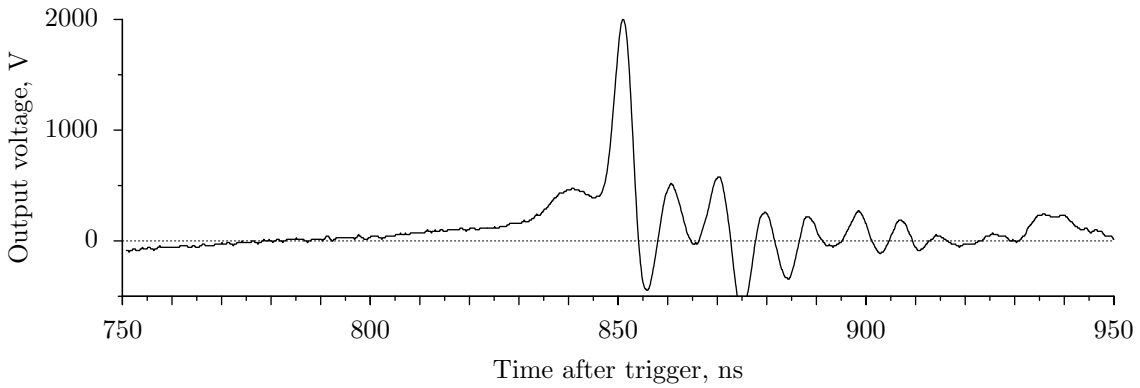

Figure E.4 Example of output electrical pulse (measured at the pulse monitor output). Note that fast oscillations after the main peak are mostly due to electrical interference in low-voltage signal lines induced by powerful electromagnetic radiation.

bias current setting the voltage should be set to the minimal value ensuring reliable current stabilization (which can be easily checked by output pulse stability).

References

[1] I. M. Ismail, M. Barat, J.-C. Brenot, J. A. Fayeton, V. Lepere, Y. J. Picard, *A zero dead-time, multihit, time and position sensitive detector based on micro-channel plates*, Rev. Sci. Instrum. **76**(4), 043304 (2005).

[2] A. I. Chichinin, K.-H. Gericke, S. Kauczok, C. Maul, *Imaging chemical reactions — 3D velocity mapping*, Int. Rev. Phys. Chem. **28**(4), 607 (2009).

[3] W. C. Wiley, I. H. McLaren, *Time-of-flight mass spectrometer with improved resolution*, Rev. Sci. Instrum. **26**(12), 1150 (1955).

[4] J. A. Syage, *Photofragment imaging by sections for measuring state-resolved angle–velocity differential cross sections*, J. Chem. Phys. **105**(3), 1007 (1996).

[5] J. L. Wiza, *Microchannel plate detectors*, Nucl. Instr. and Meth. **162**(1–3), 587 (1979).

[6] D. W. Chandler, P. L. Houston, *Two-dimensional imaging of state-selected photodissociation products detected by multiphoton ionization*, J. Chem. Phys. **87**(2), 1445 (1987).

[7] A. T. J. B. Eppink, D. H. Parker, *Velocity map imaging of ions and electrons using electrostatic lenses: application in photoelectron and photofragment ion imaging of molecular oxygen*, Rev. Sci. Instrum. **68**(9), 3477 (1997).

[8] M. L. Lipciuc, J. B. Buijs, M. H. M. Janssen, *High resolution slice imaging of a molecular speed distribution*, Phys. Chem. Chem. Phys. **8**(2), 219 (2006).

[9] Ch. R. Gebhardt, T. P. Rakitzis, P. C. Samartzis, V. Ladopoulos, Th. N. Kitsopoulos, *Slice imaging: a new approach to ion imaging and velocity mapping*, Rev. Sci. Instrum. **72**(10), 3848 (2001).

[10] J. J. Lin, J. Zhou, W. Shiu, K. Liu, *Application of time-sliced ion velocity imaging to crossed molecular beam experiments*, Rev. Sci. Instrum. **74**(4), 2495 (2003).

[11] D. Townsend, M. P. Minitti, A. G. Suits, *Direct current slice imaging*, Rev. Sci. Instrum. **74**(4), 2530 (2003).

[12] M. N. R. Ashfold, N. H. Nahler, A. J. Orr-Ewing, O. P. J. Vieuxmaire, R. L. Toomes, Th. N. Kitsopoulos, I. A. Garcia, D. A. Chestakov, S.-M. Wu, D. H. Parker, *Imaging the dynamics of gas phase reactions*, Phys. Chem. Chem. Phys.

8(1), 26 (2006).

[13] D. G. Conroy, *Rydberg state of an open shell species: characterization and photophysics of the* $3p_z$ *state of* CH_2OH, Ph. D. dissertation, University of Southern California, 2000.

[14] V. Dribinski, *Photoelectron and ion imaging studies of the mixed valence/Rydberg excited states of the chloromethyl radical,* CH_2Cl*, and the nitric oxide dimer,* $(NO)_2$, Ph. D. dissertation, University of Southern California, 2004.

[15] L. D. Landau, E. M. Lifshitz, *Mechanics*, Course of theoretical physics, Butterworth-Heinemann, 1976.

[16] C. Bordas, F. Paulig, H. Helm, D. L. Huestis, *Photoelectron imaging spectrometry: principle and inversion method*, Rev. Sci. Instrum. **67**(6), 2257 (1996).

[17] C. J. Davisson, C. J. Calbick, *Electron lenses*, Phys. Rev. **42**(4), 580 (1932).

[18] *Minutes of the Pasadena meeting, June 15 to 20, 1931*, Phys. Rev. **38**(3), 579 (1931).

[19] E. Brüche, H. Johannson, *Elektronenoptik und Elektronenmikroskop*, Naturwissenschaften **20**(21), 353 (1932).

[20] P. J. Todd, T. G. Schaaff, P. Chaurand, R. M. Caprioli, *Organic ion imaging of biological tissue with secondary ion mass spectrometry and matrix-assisted laser desorption/ionization*, J. Mass Spectrom. **36**(4), 355 (2001).

[21] M. Markl, Ph. Kilner, T. Ebbers, *Comprehensive 4D velocity mapping of the heart and great vessels by cardiovascular magnetic resonance*, J. Cardiovasc. Magn. Reson. **13**(1), 7 (2011).

[22] M. M. Harb, S. Cohen, E. Papalazarou, F. Lépine, C. Bordas, *Transfer-matrix-based method for an analytical description of velocity-map-imaging spectrometers*, Rev. Sci. Instrum. **81**(12), 125111 (2010).

[23] D. A. Dahl, *SIMION for the personal computer in reflection*, Int. J. Mass Spectrom. **200**(1–3), 3 (2000).

[24] *SIMION 8.0*, `http://www.simion.com`, Scientific Instrument Services, Inc., Ringoes, NJ.

[25] V. Papadakis, Th. N. Kitsopoulos, *Slice imaging and velocity mapping using a single field*, Rev. Sci. Instrum. **77**(8), 083101 (2006).

[26] E. Wrede, S. Laubach, S. Schulenburg, A. Brown, E. R. Wouters, A. J. Orr-Ewing, M. N. R. Ashfold, *Continuum state spectroscopy: a high resolution ion imaging study of IBr photolysis in the wavelength range 440–685 nm*, J. Chem. Phys. **114**(6), 2629 (2001).

[27] H. L. Offerhaus, C. Nicole, F. Lépine, C. Bordas, F. Rosca-Pruna, M. J. J. Vrakking, *A magnifying lens for velocity map imaging of electrons and ions*,

Rev. Sci. Instrum. **72**(8), 3245 (2001).

[28] Y. Zhang, C.-H. Yang, S.-M. Wu, A. van Roij, W. J. van der Zande, D. H. Parker, X. Yang, *A large aperture magnification lens for velocity map imaging*, Rev. Sci. Instrum. **82**(1), 013301 (2011).

[29] E. Harting, F. H. Read, J. N. H. Brunt, *Electrostatic lenses*, Elsevier Scientific Pub. Co., 1976.

[30] G. A. Garcia, L. Nahon, Ch. J. Harding, E. A. Mikajlo, I. Powis, *A refocusing modified velocity map imaging electron/ion spectrometer adapted to synchrotron radiation studies*, Rev. Sci. Instrum. **76**(5), 053302 (2005).

[31] J. A. Nelder, R. Mead, *A simplex method for function minimization*, Comput. J. **7**(4), 308 (1965).

[32] S. V. Gils, C. L. Pen, A. Hubin, H. Terryn, E. Stijns, *Electropolishing of Copper in H_3PO_4*, J. Electrochem. Soc. **154**(3), C175 (2007).

[33] W. Li, S. D. Chambreau, S. A. Lahankar, A. G. Suits, *Megapixel ion imaging with standard video*, Rev. Sci. Instrum. **76**(6), 063106 (2005).

[34] D. H. Parker, A. T. J. B. Eppink, *Photoelectron and photofragment velocity map imaging of state-selected molecular oxygen dissociation/ionization dynamics*, J. Chem. Phys. **107**(7), 2357 (1997).

[35] P. C. Cosby, D. L. Huestis, *On the dissociation energy of O_2 and the energy of the O_2^+ $b\,^4\Sigma_g^-$ state*, J. Chem. Phys. **97**(9), 6108 (1992).

[36] P. M. Regan, S. R. Langford, A. J. Orr-Ewing, M. N. R. Ashfold, *The ultraviolet photodissociation dynamics of hydrogen bromide*, J. Chem. Phys. **110**(1), 281 (1999).

[37] Yu. Ralchenko, A. Kramida, J. Reader, NIST ASD team, *NIST atomic spectra database (version 4.1)*, `http://physics.nist.gov/asd`, National Institute of Standards and Technology, Gaithersburg, MD, 2011.

[38] S. A. Harich, D. W. H. Hwang, X. Yang, J. J. Lin, X. Yang, R. N. Dixon, *Photodissociation of H_2O at 121.6 nm: a state-to-state dynamical picture*, J. Chem. Phys. **113**(22), 10073 (2000).

[39] R. Mahon, Th. J. McIlrath, V. P. Myerscough, D. W. Koopman, *Third-harmonic generation in argon, krypton, and xenon: bandwidth limitations in the vicinity of Lyman-α*, IEEE J. Quantum Electron. **15**(6), 444 (1979).

[40] W. Zhou, Y. Yuan, Sh. Chen, J. Zhang, *Ultraviolet photodissociation dynamics of the SH radical*, J. Chem. Phys. **123**(5), 054330 (2005).

[41] Z. Xu, B. Koplitz, C. Wittig, *Kinetic and internal energy distributions via velocity-aligned Doppler spectroscopy: the 193 nm photodissociation of H_2S and HBr*, J. Chem. Phys. **87**(2), 1062 (1987).

[42] L. R. Brewer, F. Buchinger, M. Ligare, D. E. Kelleher, *Resonance-enhanced multiphoton ionization of atomic hydrogen*, Phys. Rev. A **39**(8), 3912 (1989).

[43] M. Ryazanov, Ch. Rodrigo, H. Reisler, *Overtone-induced dissociation and isomerization dynamics of the hydroxymethyl radical (CH_2OH and CD_2OH). II. Velocity map imaging studies*, J. Chem. Phys. **136**(8), 084305 (2012).

[44] A. G. Smolin, O. S. Vasyutinskii, G. G. Balint-Kurti, A. Brown, *Photodissociation of HBr. 1. Electronic structure, photodissociation dynamics, and vector correlation coefficients*, J. Phys. Chem. A **110**(16), 5371 (2006).

[45] J. Li, Y. Hao, J. Yang, Ch. Zhou, Y. Mo, *Vibrational structure, spin–orbit splitting, and bond dissociation energy of $Cl_2^+(\tilde{X}\,^2\Pi_g)$ studied by zero kinetic energy photoelectron spectroscopy and ion-pair formation imaging method*, J. Chem. Phys. **127**(10), 104307 (2007).

[46] M. Michel, M. V. Korolkov, K.-M. Weitzel, *A new route to the dissociation energy of ionic and neutral HCl via lineshape analysis of single rotational transitions*, Phys. Chem. Chem. Phys. **4**(17), 4083 (2002).

[47] O. Scherzer, *Über einige Fehler von Elektronenlinsen*, Z. Phys. **101**(9), 593 (1936).

[48] H. Rose, *Theory of electron-optical achromats and apochromats*, Ultramicroscopy **93**(3–4), 293 (2002).

[49] M. Gisselbrecht, A. Huetz, M. Lavollée, T. J. Reddish, D. P. Seccombe, *Optimization of momentum imaging systems using electric and magnetic fields*, Rev. Sci. Instrum. **76**(1), 013105 (2005).

[50] Yu. A. Kotov, G. B. Mesyats, S. N. Rukin, A. L. Filatov, S. K. Lyubutin, *A novel nanosecond semiconductor opening switch for megavolt repetitive pulsed power technology: experiment and applications*, Digest of technical papers: Ninth IEEE international pulsed power conference, vol. 1, p. 134–139, Albuquerque, NM, USA, 1993.

[51] A. Kuthi, P. Gabrielsson, M. R. Behrend, P. Th. Vernier, M. A. Gundersen, *Nanosecond pulse generator using fast recovery diodes for cell electromanipulation*, IEEE Trans. Plasma Sci. **33**(4), 1192 (2005).